

A Modular Microfluidic Approach to Nano High-Performance Liquid Chromatography with Electrochemical Detection

Thesis by

Scott Brian Miserendino

In Partial Fulfillment of the Requirements
for the Degree of

Doctor of Philosophy



California Institute of Technology

Pasadena, California

2007

(Defended May 10, 2007)

© 2007

Scott Brian Miserendino

All Rights Reserved

To my parents

Acknowledgements

I am thankful for the good fortune I have had over the course of my life that has enabled me to reach this occasion. The completion of my Ph.D. thesis is a testament to the encouragement and advice I have received from many people. Without the support of family, friends, and colleges, this thesis would not have been completed, nor would the journey have been as enjoyable.

I would like to thank my advisor, Dr. Yu-Chong Tai, for his guidance, wisdom, and experience. Dr. Tai maintained a friendly working environment focused on the advancement of the MEMS field and the betterment of his students. I have benefited immensely from my discussions and interactions with him. He has taught me, above all things, the importance of good management and teamwork. I have and continue to admire his belief that if something can be built, his students can find the way to build it. Dr. Tai also recognizes that the greatest impediment to an individual's success as a researcher is his own self-doubt. I appreciate being pushed beyond what I thought was possible and I look forward to many future interactions with Dr. Tai and his research group.

During my time at Caltech, the members of the Caltech Micromachining Group were indispensable. Trevor Roper, our lab technician, is deserving of special thanks for all his patience and hard work keeping the lab running. Linda Dozsa, Tanya Owens, and Christine Matsuki provided all the administrative support a graduate student could ask for. Dr. Ellis Meng, Dr. Jun Xie, Dr. Qing He, Dr. Justin Boland, Dr. Matthieu Liger, and Dr. Victor Shih provided the world's best hands on mentoring and training in micromachining and microfluidics. Working beside and learning from Siyang Zheng, Angela Tooker, Changlin Pang, Damien Rodger, Jason Shih, Quoc "Brandon" Quach,

Po-Jiu “PJ” Chen, Nick Lo, Wen Li, and Mike Liu has been a real pleasure. To the newer members of the group, Ray Huang, Monty Nandra, Luca Giacchino, Chun-Hui “Jeffrey” Lin, and Young-Hyun “Justin” Kim, it has been great knowing and working with you and I only wish I had more time to get to know you all better. Finally, I hope I was able to pass something of value from my experience along to my former undergraduate researcher, current group member, and friend, Juhwan Yoo. Collectively, these individuals have made coming to the lab for the last five years something to look forward to, and I will definitely miss working with them.

My research was funded by the Center for Cell Mimetic Space Exploration (CMISE), a NASA University Research, Engineering and Technology Institute (URETI). On this note, I would like to thank Dr. Chih-Ming Ho for organizing CMISE and Dr. James Liao for heading the metabolics interdisciplinary research group (IRG) of which I was a part. Additionally, I am appreciative of the other graduate student members of the metabolics IRG for all of their valuable collaborations: Dr. Urvashi Bhardwaj, Li Zhang, Dr. Brian Matthew, and Mark Brynildson. Dr. Tatyana Bendikov, Dr. Alan Cassell, and Dr. Stacey Boland also deserve credit for their work on collaborative projects and publications.

During my first week at Caltech, I met a number of individuals whom I have remained close friends with during my graduate experience. Piyush Prakash, Matthew Mattson, Dr. Demetri Spanos, Max Kresh, Frosso Seitaridou, Mary-Laura Lind, Renaud Richards, and Dr. Hossein Rokhsariazar have made my life particularly enjoyable, and I look forward to continuing our friendships. Additionally, I would like to thank all those that I served with on the Caltech Graduate Student Council and Graduate Review Board. Your dedication to your community is inspiring.

Dr. Arne Fliflet, Dr. Steven Gold, Allen Kinkead, and Dr. Ralph Bruce, my first mentors in science and engineering, also deserve acknowledgement for their friendship, patience, and advice over the years. I met all of them during my first real laboratory experience at the end of the 11th grade when I was a participant in the science and engineering apprenticeship program (SEAP) and spent the summer with the Plasma Physics Division of the Naval Research Laboratory (NRL). I would spend two summers as a SEAP and three years as an undergraduate working summers and breaks at NRL. I can say with certainty that my NRL experience was critical in my decision to pursue a career in electrical engineering.

I would also like to express my thanks to my family for all of their unconditional support and guidance. My brother, TJ, and sister, Allison, have always been there for support and good times when it was needed most. Ashley, you have become part of our family and hope you and my brother have a long, happy life together. Rebecca Adler has been my best friend, confidant, and the greatest source of joy in my life for the past 2.5 years. She has also served as my personal editor, comedian, nurse, and chef. I am forever grateful for all that she has done, for continuously challenging me with alternative views, and for the wonderful person she is. My grandparents, but especially my Nan, were always there for me and helped make me who I am today. I only wish you could all be here. I would also like to thank my parents, to whom this thesis is dedicated. My mom and dad are two of the most wonderful, loving, and supportive parents a son could be blessed with. They continually offer more of themselves than can be expect of parents. I love you all and look forward to sharing many other momentous occasions with you!

Abstract

A Modular Microfluidic Approach to Nano High-Performance Liquid Chromatography with Electrochemical Detection

Thesis by

Scott Brian Miserendino

Doctor of Philosophy in Electrical Engineering

California Institute of Technology

The field of microfluidics faces many challenges that must be overcome before wide-spread use of microfluidic devices can be achieved. Chief among these challenges are the need for reliable, user-friendly packaging and robust, reconfigurable, and reusable microfluidic systems. A modular microfluidic design approach to microfluidic systems is developed and a prototype modular nano high-performance liquid chromatography (nHPLC) system with electrochemical detection is demonstrated. The modular microfluidic system requires high operating pressure, low dead volume interconnects, and assembly into a simple, reliable package. The modular approach differs from the classic monolithic approach to microfluidic systems by offering increased system flexibility, reduced individual device fabrication complexity, and increased independence of component fabrication technologies at the cost of an additional microfluidic interconnect component.

Microgaskets and MEMS O-rings based on a new, commercial, photodefinable silicone are developed and characterized to provide the necessary low dead volume

interconnects. The microgaskets and MEMS O-rings are shown to work well at typical operating pressures and did not leak under operating pressures up to 250 psi. The modular nHPLC system is used to separate a nitrate/nitrite sample with efficiencies favorably comparable to commercial macro HPLC systems and other nano HPLC systems reported in the literature. Finally, new electrochemical working electrode materials are presented for use in electrochemical detectors. One material is a thin-film carbon based on pyrolyzed Parylene-C that can conformally coat high-aspect-ratio structures to achieve better than a ten-fold increase in effective electrode area relative to geometric surface area. The second material is a carbon nanotube (CNT) nanoarray that uses a Parylene-C stabilization and insulation matrix. The CNT nanoarray shows a bifurcated sensitivity profile that indicates possible application to trace analyte detection. The combination of trace analyte detection and high-efficiency analyte separation in modular microfluidic systems places applications, such as near real-time, single cell small molecule secretion monitoring, within reach.

Table of Contents

ACKNOWLEDGEMENTS	iv
ABSTRACT.....	vii
TABLE OF CONTENTS	ix
LIST OF FIGURES.....	xi
LIST OF TABLES.....	xiv
1 MICROELECTROMECHANICAL SYSTEMS.....	1
1.1 HISTORY OF MICROELECTROMECHANICAL SYSTEMS.....	2
1.2 MEMS FABRICATION TECHNOLOGIES FOR MICROFLUIDICS	4
1.2.1 Bulk Micromachining.....	5
1.2.2 Surface Micromachining.....	7
1.2.3 Soft Lithography.....	8
1.3 LAB-ON-A-CHIP (LOC) SYSTEMS	10
1.3.1 Monolithic Systems.....	10
1.3.2 Modular Systems	12
1.4 PARYLENE MICROFLUIDICS.....	13
1.4.1 Introduction to Parylene	13
1.4.2 Parylene Microfluidics.....	15
2 LAMINAR FLOW THEORY	18
2.1 LIQUID FLOW IN PRESSURE-DRIVEN MICROFLUIDIC DEVICES	18
2.2 NAVIER-STOKES EQUATION.....	19
2.3 STOKES FLOW	23
2.4 CAPILLARY ACTION AND LAPLACE PRESSURE	25
2.5 LAMINAR FLOW IN A CYLINDRICAL TUBE	27
2.6 LAMINAR FLOW WITH NON-CIRCULAR CROSS SECTIONS	29
2.7 ENTRANCE LENGTH.....	32
2.8 STREAM FUNCTION AND VELOCITY POTENTIAL	33
3 MICROFLUIDIC PACKAGING: MICROGASKETS AND MEMS O-RINGS.....	37
3.1 INTRODUCTION	37
3.2 RESERVOIRS	39
3.3 GLUES AND EPOXIES	41
3.4 PRESS-FIT INTERCONNECTS	42
3.5 COMPRESSION INTERCONNECTS.....	46
3.6 MICROGASKETS AND MEMS O-RINGS.....	51
3.6.1 Photodefinable Silicone as a MEMS Material.....	51
3.6.2 Silicone Microgasket Fabrication.....	55
3.6.3 Microgaskets and MEMS O-Rings Theory.....	59
3.6.4 Silicone Microgasket Compression Testing	61
3.6.5 Silicone Microgasket Sealability.....	63
3.6.6 Via Dead Volume	67

3.7	CONCLUSIONS.....	68
4	MODULAR MICROFLUIDIC NANO HIGH-PERFORMANCE LIQUID CHROMATOGRAPHY.....	70
4.1	MODULAR MICROFLUIDICS.....	70
4.2	MICROFLUIDIC JIG DESIGN.....	71
4.3	HIGH-PERFORMANCE LIQUID CHROMATOGRAPHY.....	74
4.3.1	<i>Ion-Exchange Chromatography Theory</i>	76
4.3.1.1	Sample Injection.....	78
4.3.1.2	Peak Analysis.....	78
4.3.1.3	Amperometric Detection.....	80
4.3.2	<i>A Modular nHPLC System for Nitrate/Nitrite Detection</i>	83
4.3.2.1	nHPLC Component Microfabrication.....	85
4.3.2.2	HPLC Column Packing.....	88
4.3.2.3	Valve-Less Injection.....	89
4.3.2.4	Nitrate/Nitrite Separation and Detection.....	91
4.3.3	<i>Summary</i>	93
4.4	CONCLUSIONS.....	94
5	WORKING ELECTRODE MATERIALS FOR INTEGRATED ELECTROCHEMICAL DETECTORS.....	96
5.1	INTRODUCTION.....	96
5.2	ELECTROCHEMICAL CHARACTERIZATION TECHNIQUES.....	97
5.2.1	<i>Double Layer Capacitance</i>	101
5.2.2	<i>Cyclic Voltammetry</i>	102
5.3	THIN-FILM CARBON AS A MEMS MATERIAL.....	105
5.3.1	<i>TFC from Pyrolyzed Parylene-C</i>	106
5.3.2	<i>Pyrolyzed Parylene Electrodes</i>	109
5.3.2.1	TFC Electrode Fabrication.....	111
5.3.2.2	TFC Electrode Characterization.....	112
5.4	CARBON NANOTUBES NANOARRAYS.....	113
5.4.1	<i>CNT Nanoarray Electrode Fabrication</i>	115
5.4.2	<i>CNT Electrode Film Patterning</i>	120
5.5	CNT NANOARRAY CHARACTERIZATION.....	121
5.5.1	<i>Electrochemical Characterization</i>	121
5.5.2	<i>Pretreatment</i>	122
5.5.3	<i>Additional Electrochemical Characterizations after Pretreatment</i>	124
5.5.4	<i>Sensitivity and Lower Detection Limit</i>	126
5.6	CONCLUSIONS.....	128
6	CONCLUSIONS.....	130
	APPENDIX A: MECHANICAL DRAWINGS.....	133
	APPENDIX B: CONTROL CHIP FABRICATION RECIPE.....	137
	APPENDIX C: DEVICE CHIP FABRICATION RECIPE.....	139
	REFERENCES.....	142

List of Figures

FIGURE 1-1. ANISOTROPIC ETCHING OF SILICON SUBSTRATE USING A SiO_2 MASK AND KOH ETCHANT	6
FIGURE 1-2. DIFFERENT METHODS OF FORMING SURFACE MICROMACHINED MICROFLUIDIC CHANNELS.....	7
FIGURE 1-3. ONE-LAYER PDMS MICROFLUIDIC DEVICE FABRICATION	9
FIGURE 1-4. NUMBER OF MICROFLUIDIC PATENTS ISSUED PER YEAR IN THE UNITED STATES.....	10
FIGURE 1-5. PARYLENE COMPOSITION AND DEPOSITION	15
FIGURE 1-6. VARIOUS PARYLENE MICROFLUIDIC DEVICES	16
FIGURE 1-7. FULLY INTEGRATED PARYLENE-BASED LAB-ON-A-CHIP	17
FIGURE 2-1: COLOR PLOT OF THE REYNOLDS NUMBER FOR ROOM TEMPERATURE WATER FLOWING IN A CYLINDRICAL TUBE	24
FIGURE 2-2: DIAGRAM OF A MENISCUS IN A CAPILLARY TUBE.....	27
FIGURE 2-3: CROSS-SECTIONAL DIAGRAM OF LAMINAR FLOW IN A CYLINDRICAL TUBE	29
FIGURE 2-4: DIAGRAMS OF SOME CHANNEL GEOMETRIES WITH ANALYTICAL SOLUTIONS	30
FIGURE 2-5: COMMON CHANNEL CROSS SECTIONS IN MICROFLUIDIC DEVICES.....	31
FIGURE 2-6: EXAMPLE OF THE USE OF STREAMLINE ANALYSIS IN MICROFLUIDIC DEVICES.	36
FIGURE 3-1: PHOTOGRAPH OF MICROFLUIDIC DEVICE WITH GLUED TUBE INTERCONNECT	41
FIGURE 3-2: PDMS PRESS FIT INTERCONNECTS.....	44
FIGURE 3-3: DIAGRAMS OF A GASKET AND O-RING CONNECTION.....	47
FIGURE 3-4: EXAMPLE OF HIGH-PRESSURE MICROFLUIDIC SYSTEM USING COMPRESSION INTERCONNECTS	50
FIGURE 3-5. PHOTODEFINABLE SILICONE FROM THE DOW CORNING CORPORATION	53
FIGURE 3-6. SURFACE PROFILE OF NUCLEATED SILICONE DUE TO INSUFFICIENT POST-EXPOSURE BAKING	55
FIGURE 3-7. CROSS-SECTIONAL DIAGRAM OF DEVICE AND CONTROL CHIP FABRICATION	56
FIGURE 3-8. SEM OF SU8 SURFACE AFTER O_2 ETCH. CLOSEUP SHOWS ROUGHENED SURFACE..	57
FIGURE 3-9. CROSS SECTION OF GASKET STRUCTURE	58
FIGURE 3-10. IMAGES OF MEMS O-RINGS	58

FIGURE 3-11: FORCE BALANCE DIAGRAM OF MODULAR MICROFLUIDIC SYSTEM UNDER COMPRESSION	60
FIGURE 3-12: COMPRESSIBILITY OF SU8/SILICONE MICROGASKET	63
FIGURE 3-13: LEAK RATE TEST RESULTS	64
FIGURE 3-14: MEMS O-RINGS AFTER EXCESSIVE COMPRESSIVE STRESS WAS APPLIED TO SEAL THE SYSTEM	66
FIGURE 3-15: NUMERICALLY SIMULATED FLUID FLOW VELOCITY PROFILE THROUGH A VIA	67
FIGURE 3-16: DIFFERENT FABRICATED VIA GEOMETRIES AND CROSS SECTIONAL DIAGRAM.....	68
FIGURE 4-1: FIRST ATTEMPT AT MODULAR MICROFLUIDIC JIG.....	72
FIGURE 4-2: FINAL JIG DESIGN FOR MODULAR MICROFLUIDIC SYSTEM.....	73
FIGURE 4-3: ILLUSTRATION OF ANALYTICAL LIQUID CHROMATOGRAPHY	75
FIGURE 4-4: ILLUSTRATION OF ANION EXCHANGE PRINCIPLE	77
FIGURE 4-5: ILLUSTRATION OF A TYPICAL CHROMATOGRAM SHOWING TWO ANALYTE PEAKS... 79	
FIGURE 4-6: RELATIONSHIP BETWEEN VOLTAMETRIC RESPONSE OF COMPOUNDS <i>A</i> , <i>B</i> , AND <i>C</i> AND THE APPLIED POTENTIAL ON THE SELECTIVITY IN HPLC	82
FIGURE 4-7: SCHEMATIC OF nHPLC SYSTEM	84
FIGURE 4-8: CROSS-SECTIONAL DIAGRAMS OF DEVICE AND CONTROL CHIP FABRICATION FOR nHPLC.....	86
FIGURE 4-9: PHOTOGRAPHS OF THREE FABRICATED DEVICE CHIPS WITH LARGE VIAS	87
FIGURE 4-10: 7 μ M BEAD SLURRY ON CYTOMETER.....	88
FIGURE 4-11: HPLC COLUMN PACKING SETUP	89
FIGURE 4-12: ILLUSTRATIONS OF THE HPLC SEPARATION COLUMN.....	89
FIGURE 4-13: IMAGES OF VALVELESS INJECTION SCHEME.....	90
FIGURE 4-14: NITRATE/NITRITE SEPARATION RESULTS AND ANALYSIS	92
FIGURE 5-1: DIAGRAM OF ELECTRON CHARGE TRANSFER AT AN ELECTRODE AND MASS TRANSPORT TO AND FROM THE ELECTRODE SURFACE.....	99
FIGURE 5-2: (A) ILLUSTRATION OF ELECTRICAL DOUBLE LAYER. (B) EXAMPLE OF A CIRCUIT MODEL OF AN ELECTRODE/SOLUTION INTERFACE	102
FIGURE 5-3: DIAGRAM OF TYPICAL CYCLIC VOLTAMMETRY MEASUREMENT	104
FIGURE 5-4: SIMULTANEOUS THERMAL ANALYSIS DATA FOR A FREE-STANDING, 15.8 MG FILM OF PARYLENE-C.....	107
FIGURE 5-5: MICRORAMAN DATA FOR PARYLENE C.....	108

FIGURE 5-6. RESISTIVITY AS A FUNCTION OF PYROLYSIS TEMPERATURE AND HEATING RATE. .	109
FIGURE 5-7. THREE-DIMENSIONAL ELECTRODES USING PYROLYZED PARYLENE.....	109
FIGURE 5-8. TFC ELECTRODE FABRICATION PROCESS.....	111
FIGURE 5-9. FABRICATED TFC ELECTRODES.....	112
FIGURE 5-10. CYCLIC VOLTAMMOGRAMS OF 5.0 mM HEXACYANOFERRATE IN 0.1 M KCL USING PLATINUM AND PYROLYZED PARYLENE ELECTRODES	113
FIGURE 5-11. ILLUSTRATION OF A MULTI-WALLED CARBON NANOTUBE.	114
FIGURE 5-12. PECVD AND HOT FILAMENT ASSISTED VERTICAL CNT GROWTH CHAMBER.....	116
FIGURE 5-13. PHOTOGRAPH OF PECVD VERTICAL CNT GROWTH IN PROGRESS.....	116
FIGURE 5-14. VERTICAL CNTs COVERED IN 0.34 μ M OF PARYLENE.....	117
FIGURE 5-15. (A) CNTs IMMEDIATELY AFTER GROWTH. (B) CROSS-SECTION OF CNT ELECTRODE ARRAY	118
FIGURE 5-16. (A) SEM OF SINGLE CNT TIP. (B) TEM OF SINGLE CNT TIP.....	118
FIGURE 5-17. FABRICATION PROCESS FLOW FOR CNT NANOARRAY ELECTRODES.....	119
FIGURE 5-18. OVERHEAD VIEW OF CNT ELECTRODE ARRAY.....	119
FIGURE 5-19. CNT GROWTH PATTERNED USING Ti/Ni LIFTOFF AND SELECTIVE GROWTH	120
FIGURE 5-20. EMBEDDED CNT FILM PATTERNED USING O ₂ PLASMA ETCH	121
FIGURE 5-21. CYCLIC VOLTAMMETRY OF 5.0 mM K ₃ Fe(CN) ₆ IN 0.1 M KCL	122
FIGURE 5-22. ELECTROCHEMICAL CHARACTERIZATION OF CNT NANOARRAYS	125
FIGURE 5-23. SENSITIVITY MEASUREMENTS OF CNT NANOARRAYS	127

List of Tables

TABLE 1-1. CHARACTERISTICS OF ANISOTROPIC SILICON ETCHANTS	5
TABLE 1-2. ELECTRICAL, MECHANICAL, AND THERMAL PROPERTIES OF PARYLENE AND PDMS	14
TABLE 3-1: OPERATION RANGES OF VARIOUS INTERCONNECT TECHNOLOGIES	42
TABLE 3-2: TABLE OF PDMS COEFFICIENTS OF FRICTION	45
TABLE 3-3. PROCESSING PARAMETERS FOR DOW CORNING WL-5150	54
TABLE 3-4. PHOTOLITHOGRAPHY PERFORMANCE OF DOW CORNING WL-5150	54
TABLE 3-5. DETAILS OF DIFFERENT FABRICATED VIA GEOMETRIES.....	68
TABLE 4-1: NITRITE/NITRATE SEPARATION ANALYSIS.....	93
TABLE 5-1: DIFFUSION COEFFICIENTS IN WATER.....	100
TABLE 5-2. TABLE OF M FACTORS FOR TYPICAL MICROELECTRODE GEOMETRIES	101
TABLE 5-3. GAIN IN SURFACE AREA DUE TO 3-D ELECTRODE STRUCTURE.....	111
TABLE 5-4. ΔE_p OF $K_3Fe(CN)_6$ AFTER ELECTROCHEMICAL PRETREATMENT OF CNT NANO-ELECTRODES	123

1 MICROELECTROMECHANICAL SYSTEMS

The goal of this work is to address two of the most vexing challenges in modern microfluidics: fluidic packaging, and system-level design and interoperability among microfluidic components. In particular, this work will address these problems specifically for the class of Parylene-based microfluidic devices but these solutions may be extended to several other device classes, including both silicon- and glass-based microfluidics. The thesis begins with an introduction to the field of microelectromechanical systems, followed by discussion of fabrication techniques in microfluidics, lab-on-a-chip systems, and Parylene microfluidics. The second chapter will derive important formulas and theory for liquid flow in microfluidic systems. Chapter Three will discuss the development and testing of novel microgaskets and MEMS O-rings in context with other packaging technologies. Chapter Four describes a prototype modular microfluidic system for nano high-performance chromatography and electrochemical detection. The modular system is used to demonstrate the high-efficiency separation of a sample of nitrate and nitrite and prove the assertion that modular design does not drastically reduce system performance relative to macro and monolithic micro systems. Chapter Five introduces two new materials for use in on-chip electrochemical detectors. One material is a novel thin-film carbon and the other is a nanoarray of carbon nanotubes in a Parylene insulation matrix. The thesis concludes with

some final thoughts and a look forward to potential new and exciting applications of these technologies.

1.1 History of Microelectromechanical Systems

In 1947, Bell Lab scientists John Bardeen, Walter Brattain, and William Shockley invented the transistor, officially beginning the information age [1]. Subsequently in 1958, Jack Kilby built the first integrated circuit and Robert Noyce figured out how to connect the various integrated components. Less than a decade later in 1965, Gordon Moore predicted that chip complexity, measured by the number of total transistors, would double every two years to minimize cost per unit of complexity [2]. Following this prediction, Noyce and Gordon teamed up to start the Intel Corporation in 1968 and with large profits to be made in the new semiconductor industry, billions of research and development dollars were poured into developing the technology needed to fabricate transistors on the smallest possible scale.

Starting in the 1970s, academic researchers began using semiconductor technologies to build electromechanical devices out of silicon [3]. These new devices became classified as microelectromechanical systems, or MEMS. While the origins of MEMS are deeply rooted in the origins of the semiconductor industry, the fields soon diverged. The semiconductor industry remained primarily interested in the fabrication of transistors on silicon and to a lesser extent, a few III-V semiconductors. MEMS branched out into sensors, actuators, fluidics, optics, and biochemical devices [4, 5].

Since the 1980s, microfluidics has gone through several stages of development. From the mid-1980s to the mid-1990s, the field primarily focused on device miniaturization using silicon substrates [6]. In the mid-1990s interest shifted to

understanding and exploring new effects in microflow devices [7]. In 1990, Manz et al. [8] predicted that MEMS technologies could be suitable for biological and chemical applications and that these applications could be fully integrated onto a single substrate or “lab-on-a-chip,” similar to Jack Kilby’s vision of electronics. The mid-1990s also marks an important shift in microfluidic device materials. Prior to the mid-1990s, silicon was the primary material for microfluidic devices with some use of glass and several common silicon derivatives such as silicon dioxide, silicon nitride, and polycrystalline silicon. Starting in the late-1990s and into the new century polymer-based microfluidics began to dominate research investigation [9].

Two polymers, in particular, have been used on a large scale in microfluidic devices: Parylene and poly(dimethylsiloxane) (PDMS). PDMS microfluidic technology is based on the concept of replica molding, also known as soft lithography, making it an ideal candidate for prototype microfluidic systems [10]. PDMS’s popularity increased greatly with the development of simple PDMS-based pneumatic valves and pumps [11] and an easy-to-use interconnect technique in early 2000 [12]. In 2005, a complex modular PDMS-based microfluidic system was introduced by Shaikh et al. [13].

Parylene was first introduced as a microfluidic material in 1997 by Man et al. [14]. While many Parylene-based microfluidic devices have been invented, a reliable interconnect technology has remained elusive. This thesis will address the development of a fully integrated interconnect technology for high-pressure Parylene microfluidics. Also presented is the development of a completely modular microfluidic system based on Parylene technology.

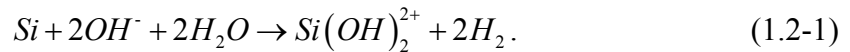
Parylene and PDMS microfluidics each have advantages and disadvantages. PDMS microfluidics typically require less equipment to fabricate, can be made in just a few days, and PDMS's gas permeability can make it a good candidate for bench-top biological applications. PDMS microfluidics, however, exhibit a relatively low maximum operating pressure, can only be integrated with a limited number of other materials (mostly glass), are not chemically inert, and are not suitable for many biomedical applications requiring implantation. Parylene is chemically inert at room temperature, Class VI biocompatible (making it useful for biomedical implants), can survive high operating pressures (one to two orders of magnitude above PDMS), and can be conformally coated. Parylene microfluidics, however, suffer from the lack of good interface technologies and greater fabrication complexity. Both PDMS and Parylene-C, a popular variant of Parylene, are relatively inexpensive materials.

1.2 MEMS Fabrication Technologies for Microfluidics

MEMS fabrication technology is the collection of techniques, materials, and machines used to build devices on the micron scale. This technology was originally borrowed from the semiconductor industry, but significant contributions have been made by MEMS researchers in the area of released (or free-standing) structures and in the micromachining of materials other than silicon or metal. Micromachining techniques most relevant to microfluidics can be broken down into three categories: bulk micromachining, surface micromachining, and soft lithography. Each of these will be discussed below.

1.2.1 Bulk Micromachining

Bulk micromachining is the manipulation of the substrate material (almost always silicon) to form mechanical structures. For microfluidic applications, bulk micromachining can be used to form microfluidic channels. After the channels have been etched into the substrate, a cover, typically glass or silicon, is bonded to the substrate at high temperatures. The substrate can be machined using either dry or wet etching techniques. Wet etching of silicon is typically anisotropic, meaning certain crystal orientations etch faster than others (Figure 1-1). Wet silicon etchants are based on the following chemistry:



The hydroxide groups can be provided by alkali hydroxide etchants (KOH, NaOH, etc.), ammonium hydroxide etchants (NH₄OH, tetramethyl ammonium hydroxide (TMAH)), or ethylenediamine pyrocatechol (EDP) [7]. Of the various etchants, KOH offers the best selectivity between the <100> and <111> plane etching. Table 1-1 displays information from several common anisotropic silicon wet etchants.

Table 1-1. Characteristics of Anisotropic Silicon Etchants [7]

Characteristic	KOH	TMAH	EDP
Concentration (weight %)	40 – 50	10 – 40	See*
Temperature (°C)	80	90	70 – 97
<111> etch rate (nm/min)	2.5 – 5	20 – 60	5.7 – 17
<100> etch rate (µm/min)	1 – 2	0.5 – 1.5	0.2 – 0.6
<110> etch rate (µm/min)	1.5 – 3	0.1	--
Si ₃ N ₄ etch rate (nm/min)	0.23	1 – 10	0.1
SiO ₂ etch rate (nm/min)	1 – 10	0.05 – 0.25	0.2
Al attack	Yes	No	Yes

*1 L ethylene diamine, 160 g pyrocatechol, 6g pyrazine, 133 mL water

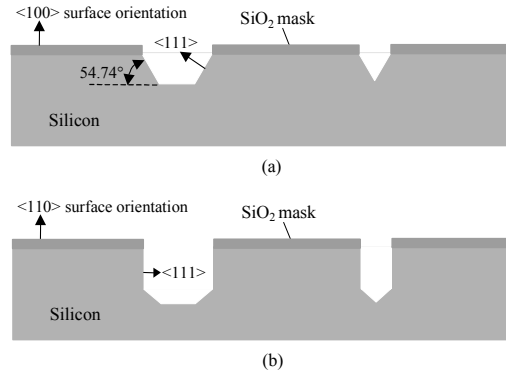


Figure 1-1. Anisotropic etching of silicon substrate using a SiO₂ mask and KOH etchant

The bulk substrate can also be etched isotropically using dry etching techniques. Dry etching involves exposure of the substrate to a plasma containing highly reactive species. The gas selected to form the plasma must selectively etch the substrate relative to the mask. Common silicon plasma etchants include CClF_3 , SF_6 , NF_3 , and CF_4 . Most of the silicon etching is performed by the fluorine free radicals in the plasma [15]. Depending on the design of the plasma etcher, the final etch can be completely isotropic, slightly anisotropic, or very anisotropic. Plasma etchers typically produce the most isotropic etching profile and are designed with the RF power electrode above and separated from the substrate.

Reactive ion etchers (RIEs) can produce slightly anisotropic etch profiles because the smaller power electrode (relative to the ground electrode) is on the bottom and in contact with the substrate, thus causing more vertical impingement of reactive species onto the wafer. The most anisotropic etching is done using a plasma etching process designed by Robert Bosch known as the Bosch process. The Bosch process involves alternating between a silicon etching step using SF_6 and a passivation deposition step using C_4F_8 . The C_4F_8 depositions protect the sidewalls of the trench while the SF_6 etch makes it deeper. Aspect ratios of 30:1 with sidewall angles of $90 \pm 2^\circ$ and etch rates of 2

to 3 $\mu\text{m}/\text{min}$ are achievable using the Bosch process [15]. Any dry etch process designed to make deep, high-aspect-ratio structures is called deep reactive ion etching (DRIE).

1.2.2 Surface Micromachining

Surface micromachining is the technique of selectively adding and removing layers of material from the surface of a substrate. Layers are patterned using photolithography and are either considered structural or sacrificial. Structural layers form the final device. Sacrificial layers are used to aid in the machining of the structural layers and are removed prior to device completion. Surface micromachining is used in many MEMS devices and is a popular fabrication technique in microfluidic devices. Surface micromachining techniques allow for materials other than silicon and glass to be used. Of particular interest is the integration and use of polymers to form microfluidic devices. A variety of microfluidic structures have been devised to form surface micromachined channels (Figure 1-2).

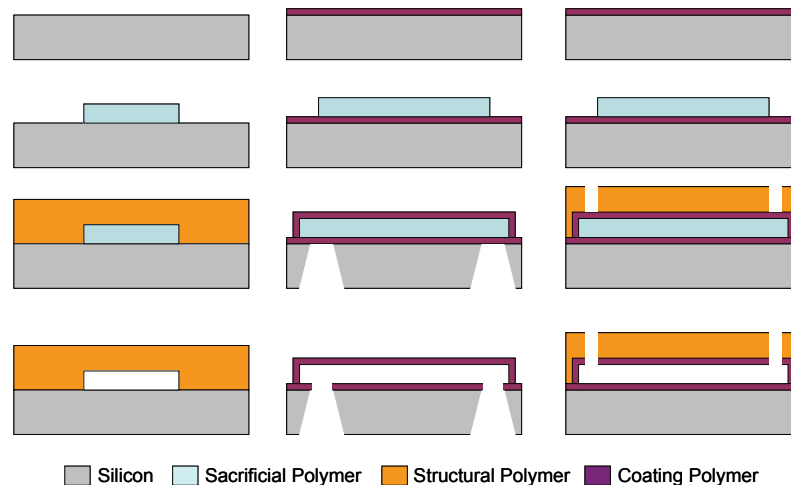


Figure 1-2. Different methods of forming surface micromachined microfluidic channels. Center diagrams show channels with backside vias while the diagrams on the left illustrate topside vias.

A major design choice when dealing with surface machined channels is whether to incorporate backside or topside vias. Backside vias require the substrate to be bulk micromachined, which can place limits on via location and cause increases in fabrication time and cost. Topside vias are typically easier and cheaper to machine but, unlike backside vias, the fluidic interconnects will block the view of a portion of the device.

Removal of the sacrificial polymer, in the case of photoresist, is done through soaking in a strong organic solvent (such as acetone or isopropyl alcohol) that does not attack the structural or coating polymer layers. Removal of other sacrificial polymers such as polynorbornene (PNB) can be done by decomposition at high temperatures (typically between 370°C and 425°C) [16]. Use of decomposition to remove the sacrificial polymer does limit the types of structural polymers that can be used since they must be able to withstand the high decomposition temperatures.

1.2.3 Soft Lithography

Soft lithography is a non optical micromachining technique. Unlike bulk and surface micromachining where either the bulk substrate or added layers of material are patterned using photolithography, in soft lithography the entire microfluidic device is made of a single material. The most commonly used material, PDMS, is a silicone rubber mixed with a curing agent and then poured over a mold, or master. The master is either made of silicon or SU8 (a UV patternable epoxy) on silicon. Silicon masters can be precisely machined using DRIE or other bulk machining processes. SU8 masters are typically lower cost and require less specialized equipment to create.

After the PDMS is poured over the master, it is allowed to cure. Cured PDMS is relatively stable with temperature and humidity, optically transparent, mechanically durable, and can be easily bonded to glass [7]. After curing, the PDMS is peeled off the mold, individual devices are cut out, fluidic vias are punched through the material, and the devices are bonded to a clean, glass substrate. A classic PDMS soft lithography fabrication diagram is shown in Figure 1-3. This procedure can be modified to include multiple layers of PDMS through PDMS/PDMS bonding. Multilayer PDMS structures make the integration of valves and pumps relatively simple [11]. A complete review of soft lithography is available from Xia and Whitesides [17].

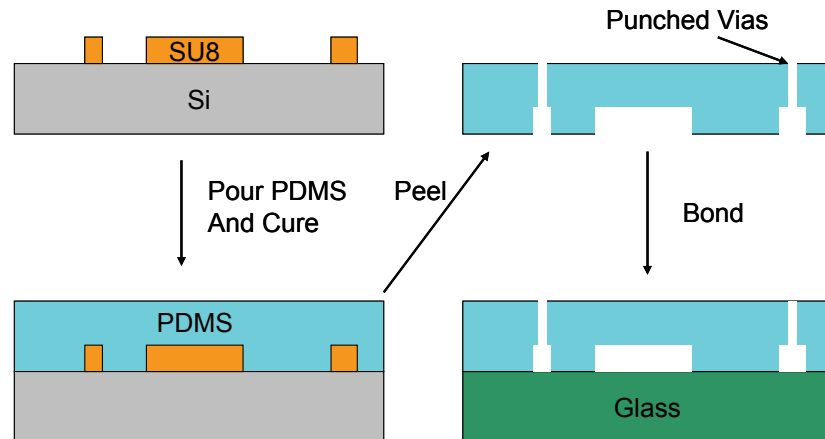


Figure 1-3. One-layer PDMS microfluidic device fabrication

Microfluidic systems based on PDMS and soft lithography suffer several drawbacks. Exposure to organic solvents can cause significant swelling of PDMS [18]. PDMS is limited to structures with aspect ratios between 0.2 and 2 [17]. The PDMS/Glass bond can only sustain pressures up to approximately 100 psi, limiting the operating range of PDMS devices [12]. PDMS is also gas permeable which makes it unsuitable for certain applications.

1.3 Lab-on-a-Chip (LoC) Systems

A complete biological or chemical analysis system fabricated on a single substrate is known as a lab-on-a-chip (LoC) or micro total analysis system (μ TAS). The first such device was a gas chromatography system developed in 1979 [19]. It was not until the early 1990s, however, that research into LoC systems became widespread. Since the early 1990s, the field has developed rapidly, welcoming contributions from many disciplines. The large body of literature focused on LoC systems has been extensively reviewed [20-22]. Some of the application areas targeted by researchers include cell handling and analysis, biomimetic and biopowered systems, clinical diagnosis, immunoassays, DNA assays, proteins assays, environmental studies, and gas analysis [22]. The growth of the LoC industry can be seen in the increase in the number of US patents relating to microfluidic devices in recent years (Figure 1-4).

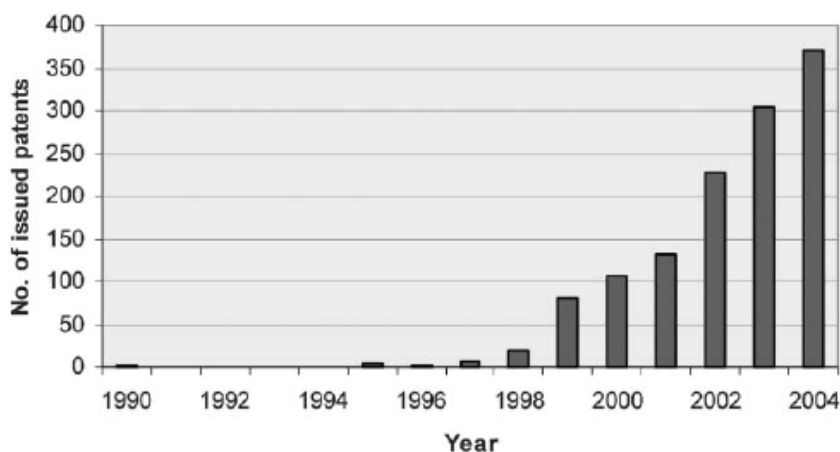


Figure 1-4. Number of microfluidic patents issued per year in the United States [23]

1.3.1 Monolithic Systems

Some of the benefits of LoC systems over their macro counterparts include smaller size; greater portability; lower power, sample, and reagent consumption; and

faster analysis times. In some instances improvements in device efficiency, sensor sensitivity, and lower detection limits are also possible. For many researchers the ultimate goal is to develop a completely integrated system on a single substrate. This monolithic approach has long been regarded as ideal. The main argument for full monolithic integration is that it will achieve minimum device size allowing for drastic reductions in device cost. These cost reductions could be significant enough to allow the devices to become “disposable” after a single use. If this can be achieved, issues of long-term reliability and system care will not be of concern.

Monolithic integration in microfluidics has only rarely been achieved in the laboratory and much less frequently with commercial success. Many laboratory systems still require off-chip pressure sources, electronics, sample preparation, and flow control. While it is almost always argued that given sufficient development time and money any device can be fully integrated, few designs progress to this stage of development. One reason for this is the lack of a so called “killer application” that would justify such an investment.

Monolithic fluidic systems tend to be very specialized. They are often not interoperable with other microfluidic devices and have difficulty adapting to changing performance demands and new technologies. Furthermore, given the relatively small markets for microfluidic devices, the costs for production are still too high to produce large numbers of single-application disposable microfluidic systems.

1.3.2 Modular Systems

An alternative approach to monolithic integration is modular design. In modular design, functional units are designed and fabricated individually and then connected using a fluidic breadboard. Modular systems typically incorporate packaging schemes that standardize fluidic and electrical interconnects and provide a flexible platform on which a variety of microfluidic functions can be performed. Since each module is individually designed and fabricated, it is easier and cheaper to upgrade their performance as new technologies become available. If components fail, the modular design allows for replacement of individual parts rather than the replacement of the entire system. Modular systems also offer greater flexibility in device fabrication since individual device fabrication processes are not required to be mutually compatible. Finally, the modular approach benefits from the reapplication of devices designed for one application to other applications. For example, a micropump module used for a protein assay application might be reused in a cell sorting application. The more applications which use the same component, the cheaper that component will be to fabricate, due to economies of scale.

Although there are many advantages to modular systems, they do have their disadvantages. Firstly, the fluidic breadboard can be complex and costly to fabricate. Secondly, the connections between the breadboard and the various devices typically introduce additional dead or sweep volume into the system that could degrade overall performance relative to a monolithic design. One of the major challenges for modular systems is developing chip-to-chip interconnect technologies that minimize dead and sweep volumes while maintaining ease of assembly, capability of withstanding high

operating pressures, and resistance to caustic reagents. Ultimately, the choice between monolithic and modular design will rest on the need for versatility in the final system. At least one company [24] and several researchers [13, 25, 26] have already recognized the trend toward modular microfluidic systems.

1.4 Parylene Microfluidics

1.4.1 Introduction to Parylene

In 1947, Parylene-N was unintentionally discovered by Michael Mojzesz Szwarc during an investigation of a class of aliphatic carbon-hydrogen bonds in which the carbon was directly attached to a benzene ring [27]. The new vapor-coated plastic piqued the interest of many companies, leading to the development of di-p-xylylene as the feedstock for the Parylene film in the 1950s by William F. Gorham (Figure 1-5) [27]. Parylene was commercialized in 1965 by the Union Carbide Corporation and widely used to protect components and assemblies in medical, electronic and automotive applications, and to preserve cultural materials and delicate antiquities. Parylene was ultimately commercialized in three primary varieties: Parylene-N, Parylene-C, and Parylene-D.

Parylene-N is a primarily a dielectric, exhibiting a very low dissipation factor, high dielectric strength, and a dielectric constant invariant with frequency [28]. Parylene-C has a useful combination of electrical and physical properties plus a very low permeability to moisture and other corrosive gases. Along with its ability to provide a true pinhole-free conformal insulation, Parylene-C is the material of choice for coating critical electronic assemblies. Parylene-C is highly biocompatible and is recognized for having the highest biocompatibility rating (USP Class VI) by the US Food and Drug

Administration, which qualifies it for use in chronic biomedical implants [29, 30]. This high biocompatibility comes from its highly chemically inert structure. Because of its conformal, pinhole free deposition, chemical inertness, and high mechanical strength, Parylene-C has been the primary choice for use in microfluidics. Parylene-D is similar in properties to Parylene-C with the added ability to withstand higher temperatures [28]. Properties of the three major varieties of Parylene and PDMS are given in Table 1-2.

Table 1-2. Electrical, Mechanical, and Thermal Properties of Parylene and PDMS [28]

Property	Parylene-N	Parylene-C	Parylene-D	PDMS [31]
Dielectric Strength (V/mil), 1 mil film	7,000	5,600	5,500	610 [32] (1 mm film)
Dielectric Constant				2.3 – 2.8
60 Hz	2.65	3.15	2.84	
1 kHz	2.65	3.10	2.82	
1 MHz	2.65	2.95	2.80	
Young's Modulus (psi)	350,000	400,000	380,000	52 – 126
Index of Refraction	1.661	1.639	1.669	1.4
Yield Strength (psi)	6,100	8,000	9,000	325
Elongation to Break (%)	20-250	200	10	210 – 310 [32]
Coefficient of Friction				
Static	0.25	0.29	0.33	--
Dynamic	0.25	0.29	0.31	0.43 – 0.51 [33]
Density (g/cm ³)	1.10 – 1.12	1.289	1.418	9.7*10 ⁻⁴
Melting Point (°C)	420	290	380	-49.9 – 40
Thermal Conductivity at 25 °C (10 ⁻⁴ cal/(cm*s*°C))	3.0	2.0	--	3.6
Specific Heat at 20 °C (cal/g*°C)	0.20	0.17	--	0.35

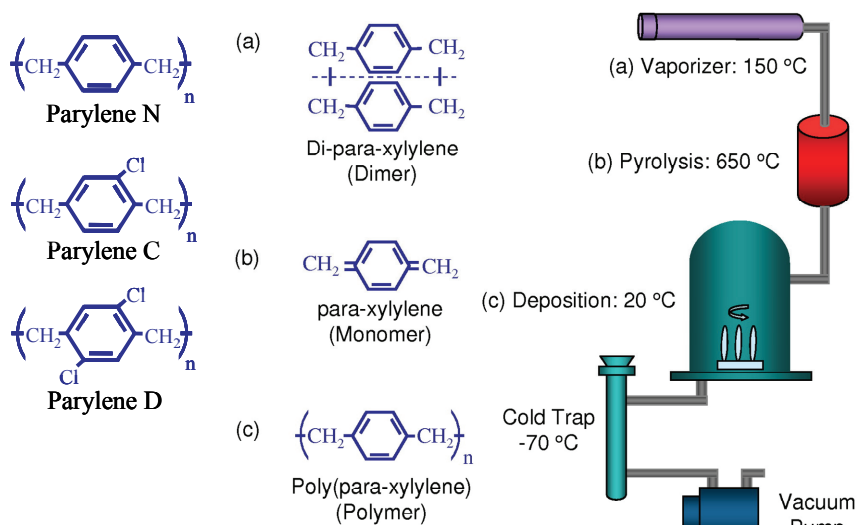


Figure 1-5. Parylene composition and deposition. (left) Different varieties of Parylene. (right) Room temperature, CVD Parylene deposition system diagram

1.4.2 Parylene Microfluidics

Parylene microfluidics provides several advantages over other common microfluidic technologies such as PDMS, glass, and silicon. Parylene microfluidic techniques have been developed that can resist internal fluid pressures above 800 psi, which allows its use in high-pressure applications that are inaccessible to PDMS (with its top working pressure between 75 and 100 psi) [13, 34]. The key to Parylene's success as a microfluidic material has been its room temperature deposition, conformal pin-hole free coating of microstructures, and ease of patterning. Room temperature deposition allows Parylene to coat a layer of sacrificial photoresist to form microchannels. Microchannels can also be formed by coating sacrificial layers of oxide or metal. Furthermore, multiple Parylene and sacrificial layers can be deposited to form three-dimensional microfluidic structures [35]. The pin-hole free deposition of Parylene makes it ideal for microfluidic applications involving gases such as micro gas chromatography, electrochemical micropumps and valves, and pneumatic micropumps and valves. Finally, Parylene can be easily etched and hence patterned using oxygen plasma. The versatility of the

Parylene processing technology allows a wide variety of microfluidic devices to be realized (Figure 1-6).

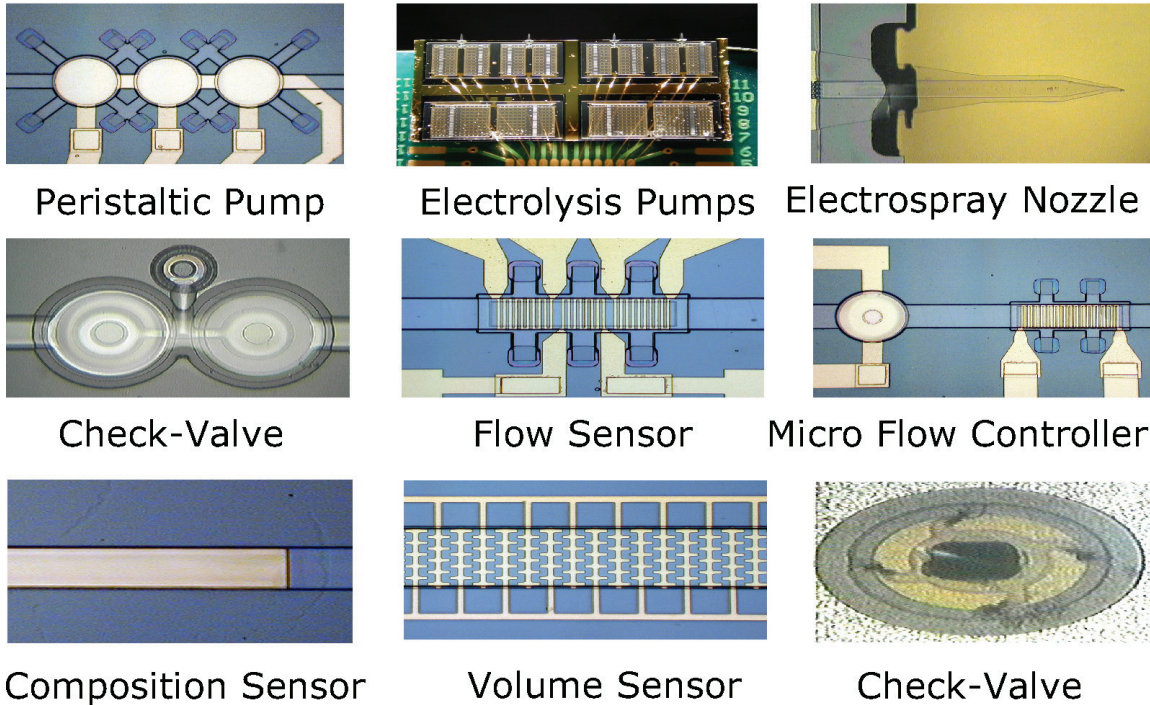
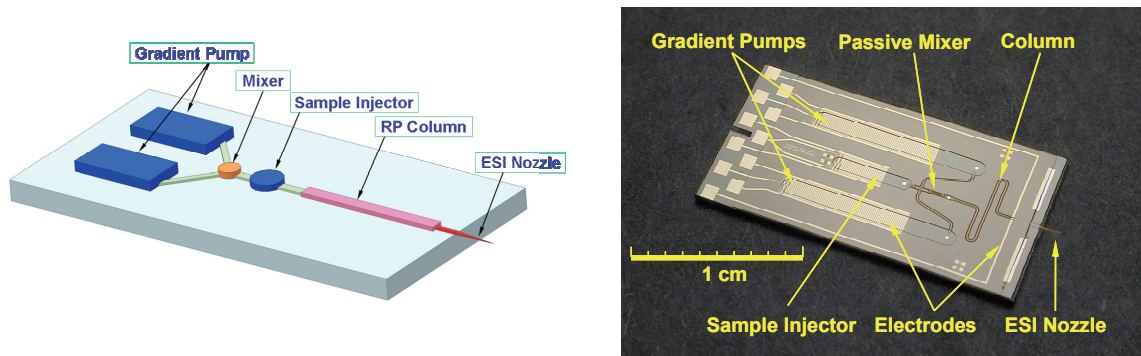


Figure 1-6. Various Parylene microfluidic devices. Pictures courtesy of Dr. Yu-Chong Tai

Entire microfluidic systems have been fully integrated using Parylene technology. One such system by Xie et al. [36] contains three electrochemical micropumps, a micromixer, an on-chip separation column, and an electro spray ionization nozzle (Figure 1-7). Parylene microfluidic systems are also being developed for biomedical applications to take advantage of Parylene's Class VI biocompatibility rating, along with research into other Parylene based MEMS implants [29, 37]. High-pressure Parylene microfluidic applications such as high-performance liquid chromatography are also being explored [36, 38, 39]. This thesis will continue to develop the field of on-chip liquid chromatography and high-pressure, Parylene-based microfluidic systems.



2 LAMINAR FLOW THEORY

The fundamental physics that govern the operation of pressure force driven microfluidics are essentially a subset of the principles that govern macro scale fluidics. Pressure force driven microfluidics, however, can make novel use of force and volumetric scaling into the micro regime, and hence provide functionality unachievable by macro-size devices. Knowledge of fluid mechanics is essential to the understanding of the design and operation of pressure force driven microfluidic devices. While fluidic theory covers a vast range of flow regimes, only a small subset of these regimes are typically encountered in microfluidic devices. This chapter will provide a short introduction to the necessary theoretical background required for understanding pressure force driven microfluidics by focusing primarily on laminar, viscous flow, and the importance of force scaling relative to device size.

2.1 Liquid Flow in Pressure-Driven Microfluidic Devices

The continuum postulate stipulates that the quantum nature of matter, namely that matter is composed of discrete particles, can be approximated by a continuous medium in which properties of a particle such as mass, velocity, pressure, and viscosity exist in and are continuously distributed over the entire space that the quantity of matter occupies. Fluid mechanics in the regime where most pressure driven microfluidic devices are operated satisfies the continuum postulate [7]. Hence, we speak of space and time

varying density, ρ , velocity, \mathbf{v} , and stress, $\boldsymbol{\tau}$. Of course, at some device length scale the continuum postulate will break down. A general rule of thumb is that the continuum postulate holds for length scales greater than 1 μm for gases and 10 nm for liquids [7].

Besides the continuum assumption, two other major assumptions on the nature of fluid flow are often made and generally hold for most microfluidic devices. First, the stress in the fluid is directly proportional to the strain; therefore, the fluid is Newtonian. Second, any heat flow is proportional to the temperature gradient, hence satisfying Fourier's law of conduction. In the case of liquid-based devices, we also assume incompressibility (constant density) and constant viscosity. All of these assumptions must be reconsidered when addressing extreme cases and complex fluid composition.

2.2 Navier-Stokes Equation

The behavior of liquid flows under these five assumptions can be summarized by the equation of motion (Newton's Second Law), the continuity equation (conservation of mass), and the Newtonian definition of viscous stress. In vector notation, the equation of motion is:

$$\rho \frac{D\mathbf{v}}{Dt} = \rho \mathbf{g} + \nabla \cdot \mathbf{T}, \quad (2.2-1)$$

where \mathbf{g} is the force due to gravity and \mathbf{T} is the stress tensor defined as:

$$\mathbf{T} = -p\mathbf{I} + \boldsymbol{\tau}, \quad (2.2-2)$$

and p , the pressure, is the stress experienced by the fluid at rest (which always acts in the outwardly directed unit normal), \mathbf{I} is an identity matrix, and $\boldsymbol{\tau}$ is the viscous stress tensor

due to the motion of the fluid. Substituting equation (2.2-2) into (2.2-1) and applying the definition of $\frac{D}{Dt}$ ¹ we find:

$$\rho \left(\frac{\partial \mathbf{v}}{\partial t} + \mathbf{v} \cdot \nabla \mathbf{v} \right) = -\nabla p + \rho \mathbf{g} + \nabla \cdot \boldsymbol{\tau}. \quad (2.2-3)$$

For a Newtonian fluid, the viscous stress tensor can be represented as a combination of the rate of strain tensor, \mathbf{d} , fluid velocity vector, shear coefficient of viscosity, μ , and the bulk coefficient of viscosity, κ , as:

$$\boldsymbol{\tau} = 2\mu \mathbf{d} + \left[\left(\kappa - \frac{2}{3}\mu \right) \nabla \cdot \mathbf{v} \right] \mathbf{I}. \quad (2.2-4)$$

The rate of strain tensor can be calculated from the velocity vector as:

$$d_{ij} = \frac{1}{2} \left(\frac{\partial v_i}{\partial x_j} + \frac{\partial v_j}{\partial x_i} \right). \quad (2.2-5)$$

The derivation of the strain tensor is not trivial, and a detailed derivation is available in Whitaker [40]. The continuity equation, a statement of conservation of mass, states:

$$\frac{\partial \rho}{\partial t} + \nabla \cdot (\rho \mathbf{v}) = 0 \quad (2.2-6)$$

which for an incompressible fluid reduces to:

$$\nabla \cdot \mathbf{v} = 0 \Rightarrow \frac{\partial v_i}{\partial x_i} = 0. \quad (2.2-7)$$

Substituting (2.2-7) and (2.2-4) into (2.2-3) we find:

$$\rho \left(\frac{\partial \mathbf{v}}{\partial t} + \mathbf{v} \cdot \nabla \mathbf{v} \right) = -\nabla p + \rho \mathbf{g} + \nabla \cdot (2\mu \mathbf{d}). \quad (2.2-8)$$

¹ $\frac{D}{Dt} = \frac{\partial}{\partial t} + v_x \frac{\partial}{\partial x} + v_y \frac{\partial}{\partial y} + v_z \frac{\partial}{\partial z} = \frac{\partial}{\partial t} + \mathbf{v} \cdot \nabla$ is called the substantial derivative and represents the

Assuming a constant viscosity solution, substituting in equation (2.2-5) and once again applying (2.2-7) reveals the Navier-Stokes equation:

$$\boxed{\rho \left(\frac{\partial \mathbf{v}}{\partial t} + \mathbf{v} \cdot \nabla \mathbf{v} \right) = -\nabla p + \rho \mathbf{g} + \mu \nabla^2 \mathbf{v}}, \quad (2.2-9)$$

which simply states that the time rate of change in linear momentum (left-hand side) must equal the applied body and surface forces (right-hand side). The Navier-Stokes equation is sufficient for isothermal systems; however, if a fluid flow experiences changes in temperature then another equation must be introduced and the assumption of constant viscosity should be reconsidered. For the vast majority of liquid fluid flows not involving chemical reactions in microfluidics, the restricted form of the equation of change for temperature is sufficient and states:

$$\rho C_p \frac{\partial T}{\partial t} = k \nabla^2 T, \quad (2.2-10)$$

where T is temperature, C_p is heat capacity at constant pressure, and k is thermal conductivity (assumed to be constant).

It is convenient to derive a dimensionless form of the Navier-Stokes equation. Three scale factors must be identified. A characteristic length (such as channel diameter), l_0 , velocity (such as average flow velocity), v_0 , and modified pressure (such as the drive pressure at the end of a channel), $\mathcal{P}_0 = p_0 + \rho g h_0$. Using the following definitions the Navier-Stokes equation can be recast

$$\tilde{x} = \frac{x}{l_0} \quad \tilde{y} = \frac{y}{l_0} \quad \tilde{z} = \frac{z}{l_0} \quad \tilde{t} = \frac{t}{l_0} \quad (2.2-11)$$

time rate of change in the moving reference frame of the substance.

$$\tilde{\mathbf{v}} = \frac{\mathbf{v}}{v_0} \quad \tilde{\mathcal{P}} = \frac{(\mathcal{P} - \mathcal{P}_0)l_0}{\mu v_0} \quad (2.2-12)$$

$$\tilde{\nabla} = l_0 \nabla \quad \tilde{\nabla}^2 = \nabla^2 \quad \frac{D}{D\tilde{t}} = \left(\frac{l_0}{v_0} \right) \frac{D}{Dt} \quad (2.2-13)$$

$$\text{Re} = \frac{l_0 v_0 \rho}{\mu} \quad (2.2-14)$$

$$\text{Fr} = \frac{v_0^2}{l_0 g} \quad (2.2-15)$$

$$\text{We} = \frac{\sigma}{l_0 v_0^2 \rho} \quad (2.2-16)$$

where equation (2.2-14) defines the Reynolds number, equation (2.2-15) defines the Froude number, and equation (2.2-16) defines the Weber number in which σ is the interface tension which could appear in the boundary conditions used to solve the partial differential equations. The dimensionless Navier-Stokes equation is

$$\text{Re} \left(\frac{D}{D\tilde{t}} \tilde{\mathbf{v}} \right) = -\tilde{\nabla} \cdot \tilde{\mathcal{P}} + \tilde{\nabla}^2 \tilde{\mathbf{v}} \quad (2.2-17)$$

Equation (2.2-17) shows the importance of the Reynolds number as a metric for determining whether the viscous forces (right-hand side) or inertial forces (left-hand side) dominate. For this reason, the Reynolds number is used to characterize different flow regimes. The first regime is referred to as laminar or creep flow and is characterized by a low Reynolds number ($\text{Re} \ll 1500$) [7]. In the laminar flow regime, the fluid dynamics are dominated by viscous forces and the inertial components of the Navier-Stokes equation can be ignored without introducing large amounts of error into the analysis.

2.3 Stokes Flow

The reduced form of the Navier-Stokes equation in the laminar flow regime is the Stokes flow or creeping flow equation:

$$0 = -\nabla p + \rho \mathbf{g} + \mu \nabla^2 \mathbf{v} . \quad (2.3-1)$$

The Stokes equation is critical for understanding fluid dynamics in microfluidic pressure-driven devices since almost all microfluidic devices satisfy the assumptions and conditions for Stokes flow. Figure 2-1 shows a plot of the Reynolds number for a pressure-driven, room temperature water flow through a cylindrical tube. As is evident from this example, microfluidic devices with typical channel diameters in the 10 to 1000 μm range and volumetric flow rates between 0.1 and 10 $\mu\text{L}/\text{min}$ are low Reynolds number flows. The second regime, “inviscid” or Euler flow, is characterized by a high Reynolds number ($\text{Re} \gg 2100$) [40]. This type of flow is almost never encountered in microfluidic systems, but is common in larger-scale, gaseous flows such as those around airplane wings. In inviscid flow, the viscous terms of the Navier-Stokes equation can be ignored resulting in the Euler equation:

$$\rho \frac{D\mathbf{v}}{Dt} = -\nabla p + \rho \mathbf{g} . \quad (2.3-2)$$

The third regime is the transitory regime in which neither the viscous or inertial components of the flow can be safely ignored.

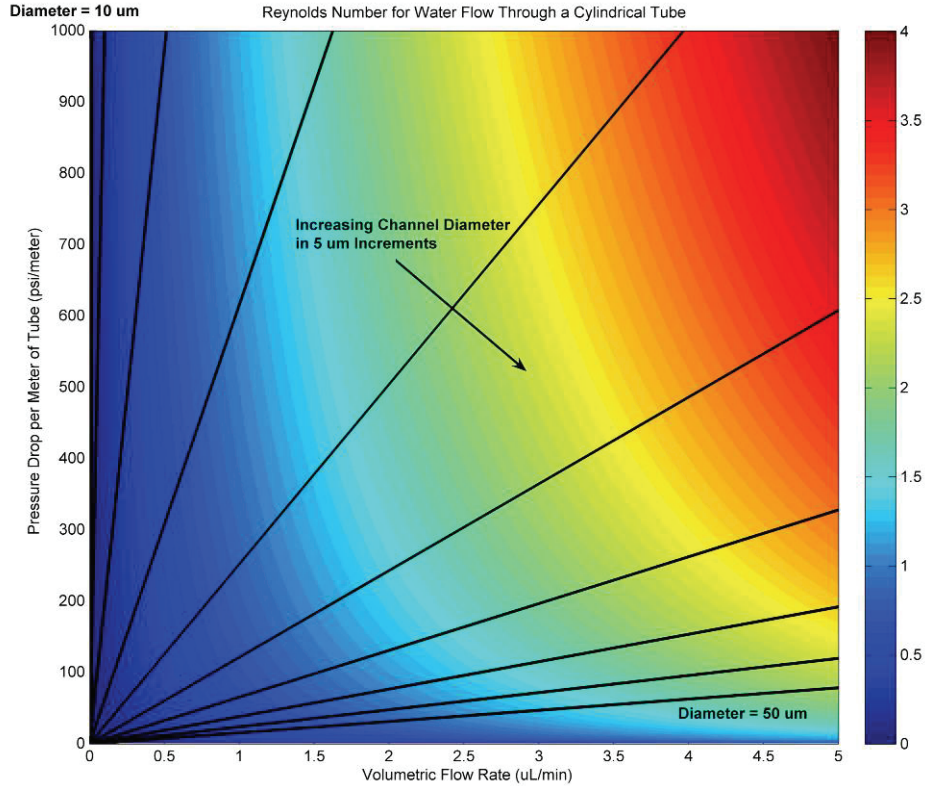


Figure 2-1: Color plot of the Reynolds number for room temperature water flowing in a cylindrical tube. Lines indicating various tube diameters are given for reference.

To solve the Navier-Stokes equations, a set of boundary conditions must be determined. The standard boundary conditions to apply are no-slip and continuous-temperature:

$$\begin{aligned} \mathbf{v}_{wall} \Big|_{liquid} &= \mathbf{v}_{liquid} \Big|_{wall} \\ T_{wall} \Big|_{liquid} &= T_{liquid} \Big|_{wall} \end{aligned} \quad (2.3-3)$$

These conditions state that the velocity and temperature of the liquid at the point of contact with a wall are equivalent to the velocity and temperature of the wall at the point of contact with the liquid. For most applications in microfluidics, these conditions are excellent models of fluid behavior; however, there are two cases that can result in a violation of the no-slip condition. The first case is fairly uncommon and has been studied

by Thompson and Troian [41]. Under instances of extremely high shear stress along the wall, the fluid will no longer behave as a Newtonian fluid resulting in a velocity slip at the fluid-wall interface. A more common example of a fluid violating the no-slip condition is that of capillary action in which a fluid creeps along a stationary wall.

2.4 Capillary Action and Laplace Pressure

Capillary action can occur at an interface of a solid, liquid, and gas. At such a three-phase interface, several forces will act on the molecules at the liquid's surface. First consider the gas-liquid interface. The molecules of liquid at the interface experience two opposing attractive intermolecular forces, commonly referred to as *Van der Waal forces*. The interface molecules are weakly attracted by the relatively low density of gas molecules on one side of the interface, and strongly attracted to the tightly packed bulk liquid molecules on the other side. This force differential over the surface area of the interface induces both a surface tension, σ , and a pressure drop across the interface. In the case of a freely suspended liquid droplet of radius, r_{drop} , the pressure drop is:

$$\Delta p = \frac{2\sigma}{r_{drop}} \quad (2.4-1)$$

At the liquid-solid interface, however, the interface liquid molecules have strong attractions to both the bulk liquid and the solid. If the intermolecular force balance favors the solid, the liquid will seek to minimize the total surface energy by spreading out along the solid's surface, a process called *wetting* [42]. A solid surface that water will wet is *hydrophilic*. If the intermolecular force balance favors the bulk liquid, the liquid will not wet the surface but instead form a bead or spherical shape in an effort to minimize the surface energy. A solid surface that induces this behavior from water is *hydrophobic*.

The angle the bead of liquid makes with the solid surface is called the contact angle, θ_c , and can be related to the surface tension of the various interfaces in the following equation:

$$\sigma_{sl} + \sigma_{lg} \cos \theta_c = \sigma_{sg} \quad (2.4-2)$$

This relationship was first suggested by Thomas Young [43] and later proven from first principles by Collins and Cooke [44]. A quantitative definition of hydrophobicity is based on the contact angle and states that a hydrophilic surface is one with a contact angle less than 90° , while a hydrophobic surface has a contact angle greater than 90° .

As with the liquid-gas interface, there is a pressure drop across a three-phase interface. By combining equations (2.4-1) and (2.4-2), the pressure drop across a meniscus in a capillary tube of radius, r , can be determined to be [7, 45, 46]:

$$\Delta p = \frac{2\sigma_{lg} \cos \theta_c}{r} \quad (2.4-3)$$

This surface tension induced pressure, referred to as the *Laplace pressure*, can play a significant role in microfluidics. For example, a glass capillary with a $5 \mu\text{m}$ radius placed in contact with room temperature water ($\sigma_{lg} = 0.073 \text{ N/m}$ and $\theta_c = 0^\circ$) will have a Laplace pressure of 4.24 psi. Laplace pressures can affect device performance, fabrication, and even design.

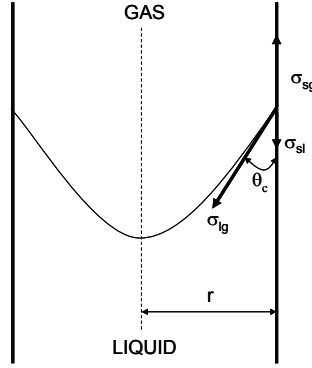


Figure 2-2: Diagram of a meniscus in a capillary tube

2.5 Laminar Flow in a Cylindrical Tube

The majority of microfluid flows can be understood by solving the Stokes flow equation (2.3-1) using the no-slip boundary conditions (2.3-3). The most general geometry to consider is that of a long, horizontal, cylindrical tube of radius, r_0 , and length, L , that extends along the z -axis. We can make several intuitive arguments about the flow in this geometry. First, the pressure drop across the tube will only occur in the z -direction and hence p will not be a function of r or θ . Second, because the fluid is assumed to have a constant density it must also have a constant volumetric flow rate through any cross-section of the tube, hence, the velocity can not be a function of the θ or z . Third, the velocity of the fluid must be finite. Using these three arguments the Stokes equation can be reduced to:

$$\frac{\partial p}{\partial z} = \frac{P_{z=0} - P_{z=L}}{L} = -\frac{\Delta p}{L} = \mu \frac{1}{r} \frac{\partial}{\partial r} \left(r \frac{\partial v_z}{\partial r} \right) \quad (2.5-1)$$

where v_z is the z -component of the fluid velocity. The no-slip boundary condition becomes:

$$v_z(r = r_0) = 0 \quad (2.5-2)$$

This partial differential equation is easily solvable with a double integration over

r :

$$r \frac{dv_z}{dr} = -\left(\frac{\Delta p}{L}\right) \frac{r^2}{2\mu} + C_1 \quad (2.5-3)$$

$$v_z = -\left(\frac{\Delta p}{L}\right) \frac{r^2}{4\mu} + C_1 \ln(r) + C_2. \quad (2.5-4)$$

Since r can reach 0 and v_z must be finite it is clear that $C_1 = 0$. Now applying the boundary condition of (2.5-2) we find:

$$C_2 = \left(\frac{\Delta p}{L}\right) \frac{r_0^2}{4\mu}. \quad (2.5-5)$$

The velocity profile is now fully determined:

$$v_z = \left(\frac{\Delta p}{L}\right) \frac{r_0^2}{4\mu} \left[1 - \left(\frac{r}{r_0}\right)^2\right]. \quad (2.5-6)$$

The functional form of the velocity profile indicates that the fluid front is a parabolic shape. A parabolic-shaped fluid flow profile is characteristic of almost all pressure-driven flows in microfluidic devices. From this velocity profile, several important parameters can be calculated. The maximum linear flow velocity, $v_{z,max}$, which occurs at $r = 0$ is:

$$v_{z,max} = \left(\frac{\Delta p}{L}\right) \frac{r_0^2}{4\mu}. \quad (2.5-7)$$

The volumetric flow rate, Q , can be calculated as the integral of the linear velocity profile over the cross section:

$$Q = \int_0^{2\pi} \int_0^{r_0} v_z r \, dr d\theta = \frac{\pi r_0^4}{8\mu} \left(\frac{\Delta p}{L} \right). \quad (2.5-8)$$

Equation (2.5-8) is known as the Hagen-Poiseuille Law. The average linear flow velocity, \bar{v}_z is defined by the ratio of the volumetric flow rate to the cross-sectional area, A ,

$$\bar{v}_z = \frac{Q}{A} = \frac{Q}{\pi r_0^2} = \frac{r_0^2}{8\mu} \left(\frac{\Delta p}{L} \right). \quad (2.5-9)$$

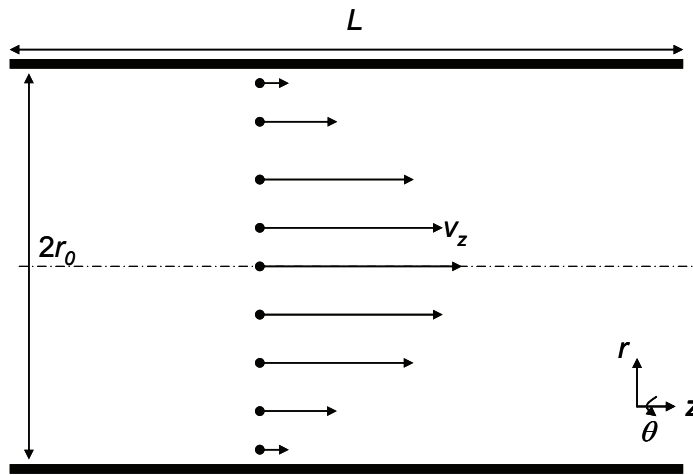


Figure 2-3: Cross-sectional diagram of laminar flow in a cylindrical tube

2.6 Laminar Flow with Non-Circular Cross Sections

The Stokes equation with no-slip boundary conditions can be applied to a variety of cross-section geometries. In many cases, analytical solutions to the equations exist describing the velocity profile and the volumetric flow rate in the laminar flow regime. Analytical solutions by Berker [47] and Shah and London [48] for rectangular and isosceles-triangular are given here for reference:

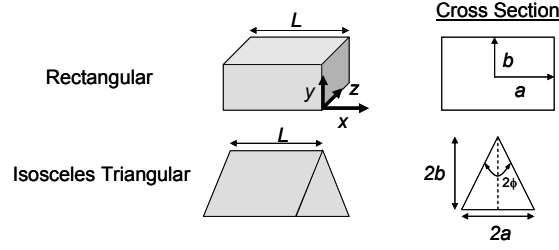


Figure 2-4: Diagrams of some channel geometries with analytical solutions

Rectangular:

$$v_x(y, z) = -\frac{16a^2 \Delta p}{\mu \pi^3 L} \sum_{i=1,3,5,\dots}^{\infty} (-1)^{(i-1)/2} \left[1 - \frac{\cosh(i\pi z / 2a)}{\cosh(i\pi b / 2a)} \right] \frac{\cos(i\pi y / 2a)}{i^3} \quad (2.6-1)$$

$$Q = -\frac{4ba^3 \Delta p}{3\mu L} \left[1 - \frac{192a}{\pi^5 b} \sum_{i=1,3,5,\dots}^{\infty} \frac{\tanh(i\pi b / 2a)}{i^5} \right] \quad (2.6-2)$$

Isosceles Triangular:

$$v_x(y, z) = -\frac{\Delta p}{\mu L} \frac{y^2 - z^2 \tan^2 \phi}{1 - \tan^2 \phi} \left[\left(\frac{z}{2b} \right)^{B-2} - 1 \right] \quad (2.6-3)$$

$$Q = -\frac{4ab^3 \Delta p}{3\mu L} \frac{(B-2) \tan^2 \phi}{(B+2)(1 - \tan^2 \phi)} \quad (2.6-4)$$

where

$$B = \sqrt{4 + \frac{5}{2} \left(\frac{1}{\tan^2 \phi} - 1 \right)}. \quad (2.6-5)$$

For arbitrary cross-sections, a couple of general methods have been proposed. Bahrami et al. [49] propose using the square root of the cross-sectional area, \sqrt{A} , as the defining length scale and derived approximations to the pressure drop across the channel. Bahrami's method achieves an accuracy of $\pm 8\%$ compared to known analytical solutions.

The conventional choice, however, for the defining length scale is the hydraulic diameter, D_h , which is defined as:

$$D_h = \frac{4 \times \text{Cross Sectional Area}}{\text{Wetted Perimeter}} = \frac{4A}{P_{wet}}. \quad (2.6-6)$$

For a channel that is entirely filled with liquid, the wetted perimeter is equivalent to the geometric perimeter. The concept behind the hydraulic diameter is to model any arbitrary channel cross-section as an equivalent circular cross-section channel with a diameter of D_h . Once an appropriate diameter has been calculated, an approximation to the flow rate and pressure drop across a channel can be made by using the analytical solutions for a channel with a circular cross-section. One must be very careful in using this empirical approach. Its accuracy improves at higher Reynolds numbers and for channel cross-sections more closely resembling a circle, meaning its application to microfluidic channels may result in relatively large estimation error [50]. For laminar, low Reynolds number flows in high-aspect ratio channels mean that the hydraulic diameter estimation technique can result in errors as high as fifty percent [50, 51].

There are two common channel cross-sections in microfluidics (rounded rectangle and trapezoid). The hydraulic diameters for these geometries are:

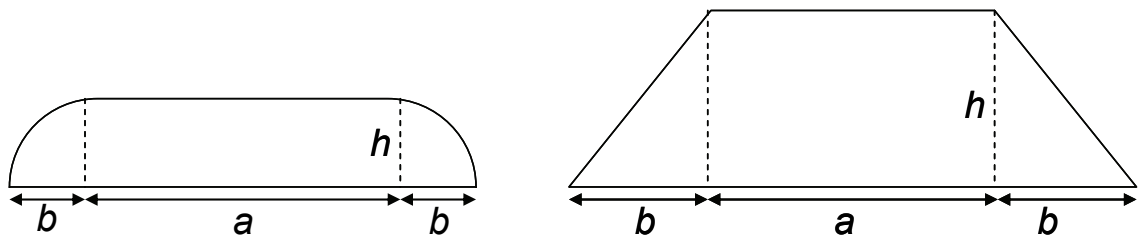


Figure 2-5: Common channel cross sections in microfluidic devices

Rounded rectangle:

$$D_h = \frac{4\left(ah + \frac{\pi}{2}bh\right)}{2(a+b) + 2b \int_0^{\pi/2} \sqrt{1 - \frac{b^2 - h^2}{h^2} \sin^2 \theta} d\theta} \approx \frac{2ah + \pi bh}{a + b + \frac{\pi}{2} \sqrt{\frac{(b^2 + h^2)}{2}}}. \quad (2.6-7)$$

Trapezoid:

$$D_h = \frac{4\left(\frac{h}{2}(a+b)\right)}{a+b + 2h \sqrt{1 + \left(\frac{a-b}{2h}\right)^2}} = \frac{2h}{1 + \frac{2h}{a+b} \sqrt{1 + \left(\frac{a-b}{2h}\right)^2}}. \quad (2.6-8)$$

The hydraulic diameter is a useful tool in estimating flow rates and pressure drops across microfluidic channels. The most common estimation for the pressure drop across a channel of arbitrary cross-section and length L is taken from equation (2.5-9) and is expressed in terms of the Reynolds number:

$$\Delta p = \text{Re } f \frac{\mu L}{2D_h^2} \bar{v}, \quad (2.6-9)$$

where f is the Fanning friction factor² and \bar{v} is the average linear flow velocity. Most microfluidic devices, however, do not consist just of fully developed flows. We must gain some understanding of when a flow can be considered fully developed.

2.7 Entrance Length

A laminar flow will develop a steady-state flow profile some distance from the inlet of the channel. This distance is referred to as the entrance length, L_e . The entrance

² The Fanning friction factor is generally a function of the flow regime (Reynolds number), roughness of the channel sidewalls, level of development of the flow, channel cross-section, and possibly other factors. For circular cross-section channels in a well-developed laminar flow regime $\text{Re } f = 64$. For rectangular cross-section channels $\text{Re } f$ is typically between 50 and 60.

length is defined quantitatively by Shah and London [48] as the point at which the centerline velocity in the channel reached 99% of its fully developed value. The entrance length has been analytically and experimentally related to the channel diameter and the Reynolds number of the flow according to [7, 40, 48, 50]:

$$L_e \approx D_h \left(\frac{0.6}{1 + 0.035 \text{Re}} + 0.056 \text{Re} \right). \quad (2.7-1)$$

This expression shows that the entrance length for low Reynolds number flows approaches 60% of the hydraulic diameter. Hence, any analysis of the velocity profile assuming a fully developed flow is only valid at distances of at least $0.6D_h$ away from any entrance or exit. For example, consider a $100 \mu\text{m}$ wide by $25 \mu\text{m}$ tall rectangular cross-section microchannel operating at a constant volumetric flow rate of $1 \mu\text{L}/\text{min}$ (estimated linear flow velocity of $0.027 \text{ m}/\text{sec}$ and $\text{Re} = 1.064$). In this example, the entrance length would be approximately $0.634D_h = 25.38 \mu\text{m}$. Further discussion of entrance effects, non-Newtonian flow behavior, viscosity changes, and other second-order considerations in analysis and visualization of fluid flows in microfluidic systems can be found in articles by Koo and Kleinstreuer [52] and Tompson et al. [53].

2.8 Stream Function and Velocity Potential

Hydraulic diameter is a useful tool in determining the input and output behavior of a microfluidic system. To gain some understanding of the internal flow velocity profile in a channel of complicated geometry in which analytically solving the Navier-Stokes equations is difficult or impossible, it is often beneficial to consider a two-dimensional model of the flow through the device. This simplification is reasonable for

most microfluidic devices. When using this simplification, one must remember that the analysis will only be valid in regions far from any changes in geometry involving the ignored dimension. A good rule of thumb is that the analysis is valid for areas in which the flow is fully developed (i.e., at least an entrance length away from any geometrical variations). The most powerful tools in two-dimensional analyses of flows are the *stream function* and *velocity potential*. While these tools are used typically in two-dimensional analysis the concepts can be extended to three dimensions [54-57].

The stream function, $\psi(x, y)$, and velocity potential, $\phi(x, y)$, are mathematical entities constructed such that they satisfy the Cauchy-Riemann equations:

$$\frac{\partial \phi}{\partial x} = \frac{\partial \psi}{\partial y} \quad (2.8-1)$$

and

$$\frac{\partial \phi}{\partial y} = -\frac{\partial \psi}{\partial x} . \quad (2.8-2)$$

The velocity field of a two-dimensional incompressible, irrotational flow ($\nabla \times \mathbf{v} = 0$) must satisfy:

$$\text{(irrotational)} \quad \nabla \times \mathbf{v} = \frac{\partial v_x}{\partial y} - \frac{\partial v_y}{\partial x} = 0 \quad (2.8-3)$$

$$\text{(continuity equation)} \quad \nabla \cdot \mathbf{v} = \frac{\partial v_x}{\partial x} + \frac{\partial v_y}{\partial y} = 0 . \quad (2.8-4)$$

By combining the Cauchy-Riemann equations with equations (2.8-3) and (2.8-4) the stream function and velocity potential can be differentially defined in terms of the flow velocity field:

$$\frac{\partial \psi}{\partial x} = v_y \quad \text{and} \quad \frac{\partial \psi}{\partial y} = -v_x \quad (2.8-5)$$

$$\frac{\partial \phi}{\partial x} = -v_x \quad \text{and} \quad \frac{\partial \phi}{\partial y} = -v_y. \quad (2.8-6)$$

Once a suitable stream function is found, it is possible to construct a family of stream lines by setting the function equal to a constant, thus generating a different stream line for each constant chosen. A similar approach can be used with the velocity potential to produce a family of equipotential lines. Stream lines and equipotential lines are useful in the study of microfluidic devices because of several convenient analytical and experimental properties. A few of these properties are:

- Stream lines and equipotential lines never intersect themselves.
- Stream lines are everywhere perpendicular to equipotential lines.
- Stream lines are everywhere tangent to the fluid velocity.
- A solid surface placed along a stream line will not affect the flow velocity.
- Changes in distance between stream lines are indications of changes in fluid-flow velocity, with denser stream lines indicating higher flow velocity.
- For steady flows the stream lines represent the path an infinitesimal particle will take through the channel when that particle is placed on the stream line.

The last property given about stream lines is the most commonly used in the study of microfluidics. By injecting small particles or dye molecules into the fluid flow stream, lines can be traced or visualized experimentally, giving an idea of the behavior of larger particles in the flow [58-60]. Stream lines are also often used in analytical or finite element analysis of fluid flows to better understand device function (Figure 2-6).

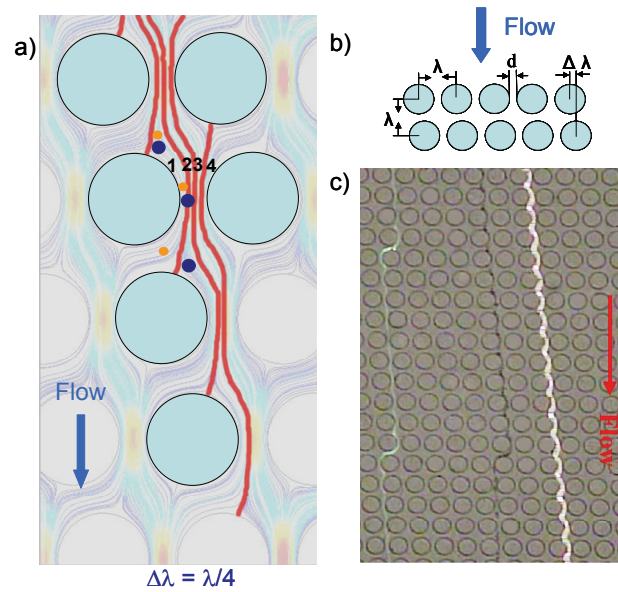


Figure 2-6: Example of the use of streamline analysis in microfluidic devices. Streamlines used to analyze flow behavior of 5 μm , 8 μm , and 10 μm fluorescent beads in a deterministic lateral displacement filter. (a) Finite-element analysis of periodic column geometry with flowlines between stagnation points highlighted. (b) Diagram of device geometry. (c) Visualized separation of beads in continuous flow. (Images adopted, with permission, from [60])

3 MICROFLUIDIC PACKAGING: MICROGASKETS AND MEMS O-RINGS

3.1 Introduction

Packaging is the term used to describe any method, material, or technology used to interface a micro scale device to the macro scale world or to link multiple devices together into a complete system. Packaging is one of the most challenging and often overlooked aspects of microfluidic system design. It plays a major role in overall system performance and can have an enormous influence on the extent to which a technology is adopted for use in research or commercial applications. When done properly, packaging will hardly be noticed; however, poor packaging can lead to problems that can easily dominate a user's time and adversely affect device performance.

One reason device packaging is a difficult problem is that there are many considerations that must be taken into account for it to be successful. Ideally, microfluidic packaging will allow the device to exhibit low or no leak rates, high maximum sealing pressures, no clogging, excellent thermal stability, chemical inertness, high mechanical strength, low dead volume, reusability, easy integration into fabrication processes, scalability with device feature size, and a user interface that is easy-to-use and gracious in its failing when misused. In extreme circumstances such as those involved in space flight, biomedical implants, and military applications, packaging must be highly

durable, biocompatible, and unaffected by long exposure to extreme heat, cold, and radiation.

In the case of microfluidic devices, an aspect of packaging that is of critical importance is the fluidic interconnect. Similar to electrical interconnects in many other MEMS applications, fluidic interconnects provide the physical path for fluid to enter and leave the micro system. Fluidic interconnects are the center of microfluidic packaging. A variety of interconnect technologies have been developed since the advent of microfluidics, yet, the vast majority of reported microfluidic devices still use very rudimentary interconnect technology. A review article by Fredrickson and Fan covers many of the current and historical approaches to the problem [61]. Interconnect technologies can be categorized into four types: 1) reservoirs, 2) glues and epoxies, 3) press-fit, and 4) compression. Several interconnect schemes consist of varied combinations of these four basic technologies.

Each of the four basic interconnect technologies has its benefits and drawbacks. Reservoirs require little to no specialized micromachining steps yet they can not be used with externally driven pressure flows and are prone to complications arising from evaporation. Glues- and epoxy-based interconnects can handle pressure driven flows and require almost no specialized micromachining, but can cause clogging and must be manually added to each device after fabrication. Press-fit interconnects are simple and easy-to-use but are limited to classes of devices made from soft materials, such as PDMS. Press-fit interconnections based on coupler technology are compatible with silicon-based microfluidics but require specialized fabrication steps. Compression interconnects can withstand the highest operating pressures and are compatible with silicon and glass

microfluidics but require a jig or other auxiliary packaging setup. Only compression interconnect techniques can be readily applied to coupling directly between two microfluidic devices without use of external tubing. The use of surface micromachined microgaskets and MEMS O-rings allows for fully integrated, low dead volume interconnects between multiple microfluidic devices with only minimal increase in fabrication complexity.

3.2 Reservoirs

Reservoirs are the simplest interconnect technology. Reservoirs are large-volume containers, either machined into the device or attached to it, that store the working fluid. Reservoir systems typically rely on capillary action to fill the system with fluid (see Section 2.4). This interconnect technology is particularly useful in electroosmotic systems where fluid flow is induced between reservoirs through the application of large electric fields. Reservoir systems are sensitive to evaporation of the working fluid and hydrostatic pressure flows. *Hydrostatic pressure* arises from the collective weight of the fluid. In a reservoir, the pressure at the bottom of the reservoir containing a static ($\mathbf{v} = 0$) fluid column of height, h , can be easily derived from (2.3-1):

$$p_{static} = p_{atm} + \rho gh, \quad (3.2-1)$$

where p_{atm} is the atmospheric pressure above the liquid column, ρ is the density of liquid, and g is the acceleration due to gravity. In a system of two or more connected reservoirs the hydrostatic pressure in each reservoir must be equal, otherwise a pressure-driven flow will result from the reservoir of higher pressure to that of lower pressure until an equilibrium is reached. As a result, relative height differences of the liquid columns in

the reservoirs need to be constantly controlled in this packaging scheme in order to avoid any unexpected pressure gradients.

The maximum unrestricted evaporation rate of a liquid can be estimated using the Hertz-Knudsen-Schrage relationship:

$$E_{max} = \eta_{ev} A P_v \sqrt{\frac{M}{2\pi RT}} \quad (3.2-2)$$

where η_{ev} is Schrage's correction factor (traditionally taken as 2 but more recently found to be 1.667 [62]), A is the area of the fluid/gas interface, M is the molar mass of the liquid, R is the ideal gas law constant, P_v is the equilibrium vapor pressure at the liquid surface, and T is the absolute temperature [62, 63]. This maximum is hardly ever achieved in real devices because of the presence of a relatively stagnant vapor layer between the liquid interface and top of the reservoir. Because hydrostatic pressure is not a function of reservoir cross-sectional area, the fluid level in all reservoirs must be at the same height for a system in equilibrium. Evaporation rate, however, is a function of reservoir geometry and hence if reservoirs are not carefully designed and filled, a near constant non-equilibrium state could result. Furthermore, because the equilibration process is driven by relatively weak hydrostatic pressure differences through high-resistance fluidic channels, systems using reservoir interconnects can take a long time to equilibrate often exacerbating the evaporation problem. Although minimization of evaporations effects is typically desirable, they can be used as an actuating mechanism for reservoir-based pressure-driven devices [64].

3.3 Glues and Epoxies

The simplest pressure-tolerant interconnect technology used in microfluidics are tubes manually glued to the surface of the microfluidic device (Figure 3-1). Even with its simplicity and obviation of any special microfabrication process, this technique has many obvious disadvantages, including possible clogging, need for manual alignment, and incompatibility with some surface-machined devices. The process of attaching the tubes can also be time consuming and is prone to a low success rate. Glued or epoxied interconnects are permanent and tend to have relatively low maximum operating pressures. More recently glues and epoxies have been used to augment other interconnect technologies to improve mechanical strength and pressure tolerance. Table 3-1 compares the operating range of several pressure-tolerant interconnect technologies.

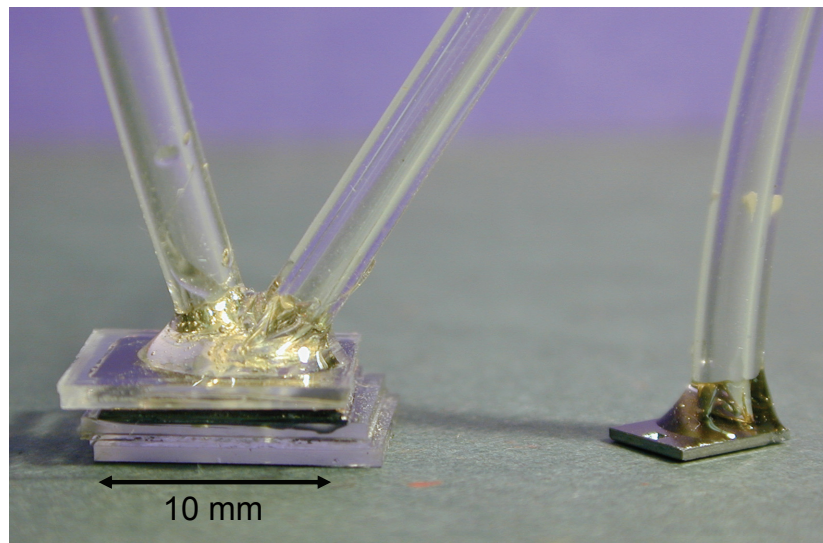


Figure 3-1: Photograph of microfluidic device with glued tube interconnect [65]

Table 3-1: Operation Ranges of Various Interconnect Technologies [65]

Interconnect Technology	Operation Range	Reference
Polyethylene Coupler/Tubing and Epoxy Reinforcement	> 5 kPa (0.7 psi)	[66]
Mylar Sealant and Epoxy Reinforcement with Capillary	~ 190 kPa (28 psi)	[67]
Polyimide/Parylene Ribbon Cable Style Interconnect	~ 200 kPa (29 psi)	[68]
Silicon Finger Microjoint with Silicone Gasket & Tygon Tubing	> 210 kPa (30 psi)	[69]
Thermoplastic Retaining Flange with PEEK Tubing	> 210 kPa (30 psi)	[70]
PDMS Press fit	~ 300-700 kPa (40 -100 psi)	[12]
Silicon/Plastic Coupler with Silicone Gasket & Capillary	~ 410 kPa (60 psi)	[71]
Silicone Gasket Sealed Silicon Coupler with Capillary	~ 550 kPa (80 psi)	[72]
Photopatternable Silicone O-rings	> 1.7×10^3 kPa (250 psi)	[25]
Silicon Sleeve Coupler with Capillary	~ 3.6×10^3 kPa (500 psi)	[71]
Polymer Coupler with Fused Silica Capillary	~ 6.2×10^3 kPa (900 psi)	[65]
Silicon Bulk Coupler with Cryogenically inserted PEEK Tubing	> 9×10^3 kPa (1300 psi)	[73]
Silicon Post Coupler with Fused Silica Capillary or PEEK Tubing	> 9×10^3 kPa (1300 psi)	[73]
Silicon Flanged Coupler with PEEK Tubing	> 1×10^3 kPa (1500 psi)	[65]
Mismatched Silicon Coupler with Capillary	> 1.2×10^3 kPa (1740 psi)	[74]

3.4 Press-Fit Interconnects

While glues and epoxies might be the simplest pressure tolerant interconnect technology, the most popular pressure tolerant microfluidic interconnect is probably the press-fit, or interference-fit, interconnect. There are several version of press-fit interconnects but all work by sliding a capillary tube into a specially made via or coupler. A variety of press-fit interconnect schemes have been developed for use in silicon-based

microfluidics [73]. For silicon and surface micromachined based microfluidics press-fit connectors are more difficult to use because silicon is not elastic enough to provide sidewall compression and surface machined microfluidic devices are too thin to provide the mechanical stability necessary for such interconnects. The silicon-based press-fit interconnects require a coupler that attaches to a capillary and can be either glued or snapped into a specially machined receiving port on the device [73]. The capillary is inserted into the coupler after being frozen in liquid nitrogen and is allowed to warm to room temperature [73]. The warming process causes the capillary to expand and press up against the walls of the coupler, producing a locking force.

The reason press-fit interconnects are so popular today is that they are the ideal type of connector for a soft, compressible material such as PDMS. Since press-fit interconnects are used so often in PDMS microfluidics, it is valuable to examine this case. Typically, the interconnection is made by first boring a via with a needle or other sharp coring tool (Figure 3-2). The boring procedure can have a large effect on the pressure tolerance of the final interconnect. The best interconnects are formed in at least 3 mm thick PDMS using a sharpened flat-tip needle and a slight downward twisting motion [12]. Next a capillary, usually made of stainless steel, is inserted into the bored hole. The outer diameter of the capillary must be larger than the boring tool's inner diameter, ideally several hundred microns larger. A typical boring tool is a 20 gauge (610 μm inner diameter) flat-bottom needle. An unmodified 20-gauge needle flat-bottom luer adapter (953 μm outer diameter) is a convenient capillary since it allows for easy connections to other fluidic components off-chip. Any spiral or vertical cracks in the bored hole will result in leaking, even at low operating pressures.

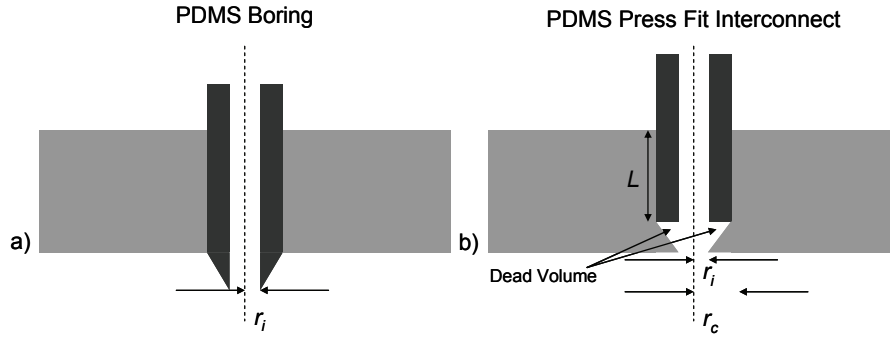


Figure 3-2: PDMS press fit interconnects. (a) PDMS interconnect being bored with sharp coring tool. (b) PDMS press fit interconnect showing possible regions of dead volume

Press-fit locking force, the force required to remove a press-fit connector, can be estimated by first assuming that the elasticity of the PDMS is much greater than the elasticity of the capillary and hence no deformation of the capillary will occur. It should be noted that this assumption is not generally true of all press-fit connections since most involve fitting of two metals, but in the case of PDMS and either a metal or glass capillary this assumption is reasonable. We also assume that the frictional force on the sidewall of the capillary can be approximated by a Coulomb friction (linear) relationship with coefficient of friction, μ_f , and we find:

$$\varepsilon_r = \frac{r_c - r_i}{r_i} \quad (3.4-1)$$

$$\sigma_r = E_r \varepsilon_r \quad (3.4-2)$$

$$F_{lock} = 2\pi r_c \mu_f \int_0^L \sigma_r dz \quad (3.4-3)$$

$$F_{lock} = 2\pi \mu_f E_r L (r_c - r_i) \frac{r_c}{r_i} \quad (3.4-4)$$

where ε_r is the radial strain, σ_r is the radial stress, E_r is the Young's modulus in the radial direction (for PDMS typically between 360 and 870 kPa, and usually close to 600 kPa [33]), L is the length of capillary inserted into the PDMS, r_c is the outer radius of the capillary, and r_i is the initial radius of the via before capillary insertion. Equation (3.4-4) makes the further assumption that the radial stress is constant along the length of the capillary. Many factors can affect the locking force of a press-fit interconnect and several more complex estimation methods have been proposed [75, 76]. A compilation of coefficients of friction for PDMS is given in Table 3-2. Researchers have also noted that the locking force tends to reduce over time due to material relaxation and with repeated insertions of capillary tubes.

Table 3-2: Table of PDMS Coefficients of Friction

Materials	Coefficient of Friction, μ_f	Reference
PDMS Bulk-Silicon	$0.11 \pm 10\%$	[33]
PDMS Film-PDMS Film	$0.43 \pm 10\%$	[33]
PDMS Bulk-PDMS Bulk	$0.51 \pm 10\%$	[33]
PDMS Bulk-Stainless Steel	$0.58 \pm 10\%$	[75]

To prevent the interconnection from blowing out, the locking force must exceed the maximum hydrostatic end force, $H_{G,max}$, applied to the capillary by the working pressure of the fluid, p , in the system [77]:

$$H_{G,max} = \pi r_c^2 p, \quad (3.4-5)$$

$$p \leq 2\mu_f E_r L \left(\frac{1}{r_i} - \frac{1}{r_c} \right). \quad (3.4-6)$$

The locking force for the PDMS press-fit connection made using a 20-gauge flat-bottom needle and 20-gauge luer adaptor is approximately 1.76 N and is theoretically capable of withstanding a maximum working pressure of 2.46 MPa (357 psi). Practically, these

types of interconnects are rarely operated over 700 kPa (~100 psi) because the PDMS/substrate adhesion is not sufficient to withstand such high pressures [12]. PDMS press-fit interconnects can contain some dead volume, as depicted in Figure 3-2, when the insertion length is less than the thickness of the PDMS. This interconnect dead volume is usually quite small and tends not to be a factor in device performance. There is no doubt that the availability of an easy-to-use, unrestrictive, reliable, and versatile interconnect methodology is a key factor in the widespread use of PDMS in modern microfluidics.

3.5 Compression Interconnects

While the press-fit interconnect has gained wide acceptance in PDMS microfluidics, its use has been very limited among other microfluidic fabrication technologies. Microfluidic devices made using fabrication technologies such as bulk micromachining and surface micromachining tend to rely on compression interconnects when a reusable, unrestrictive, and reliable interconnect is required. Compression interconnects in microfluidic systems are similar to the interconnections found in macroscopic fluidic systems. Specifically, the fundamental sealing technology is gaskets and O-rings.

Gaskets are compressible membranes of any shape that typically seal multiple fluidic paths simultaneously and have holes in them through which fasteners are placed to apply the compressive force between the bottom flange and the top flange. O-rings are continuous rings of constant cross-sectional shape placed between the fluid flow path and an arrangement of fasteners used to compress the O-ring and seal the connection. O-

rings are usually compressed individually and seal only one fluidic path at a time. Figure 3-3 illustrates the basic differences between gaskets and O-rings.

Both gaskets and O-rings require a compressive force first to seat them and then to maintain enough pressure to prevent the working fluid from leaking. The compressive force developed by a set of N fasteners is:

$$F_{compress} = \sum_{i=1}^N \frac{T_i}{KD_{f,i}} \quad (3.5-1)$$

where T_i is the torque on the i^{th} bolt, K is the fastener friction factor (typically 0.20 for a dry fastener and 0.16 for a lubricated fastener), and $D_{f,i}$ is the nominal fastener diameter of the i^{th} bolt [78]. For a set of identical, equally torqued bolts equation (3.5-1) reduces to:

$$F_{compress} = \frac{NT}{KD_f} \quad (3.5-2)$$

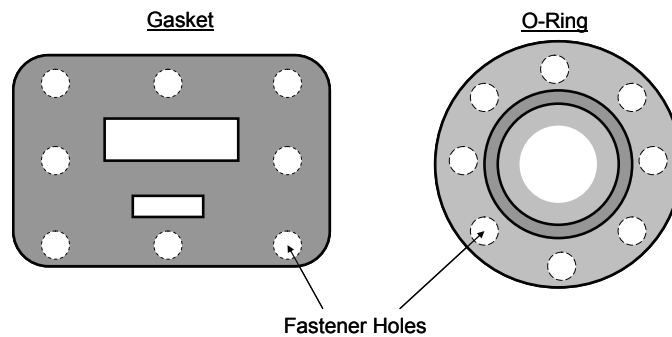


Figure 3-3: Diagrams of a gasket and O-ring connection. The gasket is shown with two fluid flow paths and cut-outs for fasteners. The O-ring is shown with a single fluid flow path and fastener holes surrounding the O-ring.

Gaskets require a minimum seating stress to initially seat the gasket during joint assembly [78]. This minimum seating stress, σ_y , is a function of gasket material and

flange geometry and must be experimentally determined. Once σ_y is known, a minimum fastener torque must be applied to seat the gasket such that [78]:

$$T \geq \frac{A_s K D_f \sigma_y}{N} \quad (3.5-3)$$

where A_s is the seated area of the gasket. After seating the gasket a constant compressive force must be maintained such that the gasket stay seated and that it overcome any hydrostatic end force that develops.

In the case of O-rings, it is unclear at what point in the O-ring the hydrostatic load reaction occurs. This causes difficulty in defining the seated area. The diameter associated with the point of load reaction is termed G . According to the American Society of Mechanical Engineering (ASME) Code for Pressure Vessels Section VIII Division 1 [79], for typical O-ring sizes used in microfluidic systems, G can be taken as the mean gasket diameter:

$$G = D_g - W_g \quad (3.5-4)$$

where D_g is the outer O-ring diameter and W_g is the width of the O-ring. For other types of flange and O-ring geometries G is defined differently, often moving it closer to the edge of the O-ring for O-rings wider than 0.5 inches [79]. The ASME Code, however, does not offer an analytical definition of G and has changed how it is calculated over time [79, 80]. Some authors have expressed discontent at the ASME Code and use the inner O-ring diameter instead of G . Bouzid et. al. [81] define $G/2$ analytically as the radial location at which the total torque on the gasket due to compressive stress, $S_g(r)$, is equivalent to the torque developed from a force applied at a distance $G/2$ equal to the total geometric gasket area, A_g , times the average compressive stress per gasket, \bar{S}_g .

This analytical definition closely conforms to the ASME Code for thin gaskets and can be used for nonlinear gasket behavior induced by flange rotation. Furthermore, it can be expressed mathematically as:

$$\int_{D_g/2-W_g}^{D_g/2} 2\pi r^2 S_g(r) dr = \frac{G}{2} A_g \bar{S}_g. \quad (3.5-5)$$

Under uniform radial stress:

$$G = D_g - W_g + \frac{W_g^2}{3(D_g - W_g)}. \quad (3.5-6)$$

In the case of uniform radial stress, the definitions for G according to Bouzid and the ASME code only differ by a small factor.

Hence, to seat an O-ring the minimum seating torque per fastener, using the AMSE definition of G , is:

$$T_{\min} = \frac{\pi K D_f W_g (D_g - W_g) \sigma_y}{2N}. \quad (3.5-7)$$

The maximum fluid working pressure, p , an O-ring interconnect formed with N identical, equally torqued fasteners can withstand is:

$$p_{\max} = \frac{4NT}{\pi K D_f (D_g - W_g)^2}. \quad (3.5-8)$$

Microfluidic systems have a major advantage in using compression interconnects over macroscale fluidic systems due to the inverse square relationship between maximum sustainable pressure and O-ring diameter. While compression interconnections are ideal for high-pressure microfluidic applications, their major drawback is the need for a more complex packaging scheme. The only way to apply compression interconnects is with the use of a jig. The jig is used to hold the microfluidic device, and external fluidic

tubing, and help alignment of the O-rings or gasket with the vias on the device (Figure 3-4). Jigs tend to be custom-made for each microfluidic system, meaning substantial increases in the system cost, size, and development time. Jigs, however, offer excellent mechanical stability, the opportunity to readily interface with the wide array of commercially available products for handling fluids off-chip, and protection for the microfluidic device. Most jig designs also attempt to incorporate a method for providing electrical interconnects to the microfluidic system. By solving both the electrical and fluidic interconnect problems, jigs can prove to be well worth the investment. In any commercial application, jigs will likely be a requirement because most microfluidic devices are too delicate to be used outside of a laboratory setting in an unpackaged state.

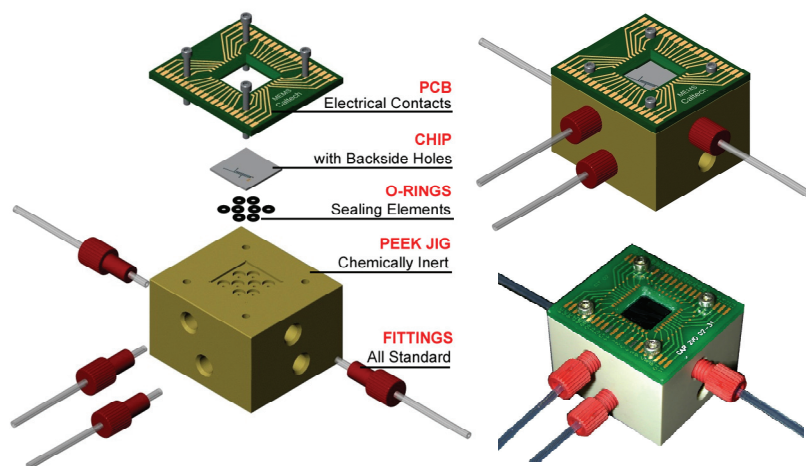


Figure 3-4: Example of high-pressure microfluidic system using compression interconnects. Left and top-right images are rendered computer models. Bottom-right image is a photograph of the assembled system. (Images adopted, with permission, from [82])

Compressive interconnect technologies can be used both to connect microfluidic devices to the outside world and to connect multiple microfluidic devices together. In order to successfully accomplish the goal of interconnecting multiple microfluidic

devices, the compressive interconnect technology must be miniaturized and integrated into the microfluidic device fabrication. These miniaturized compressive interconnects are called microgaskets and MEMS O-rings.

3.6 Microgaskets and MEMS O-rings

Commercial O-rings are the most common sealing mechanism used in compression interconnects. Commercial O-rings, however, must be manually aligned and ultimately are limited in minimum size. The desire for arbitrary shaped fluidic vias, high density interconnections, and extremely high accuracy alignment has led to the need for fully integrated MEMS O-rings. Silicone rubbers have proven successful as a material for commercial O-rings and gaskets. Silicone rubber is the most likely candidate for MEMS O-rings because of its relative thermal stability, chemical stability, great compressibility, and weak adhesion to many materials (important because the O-ring should not stick or bond to the flange) [83]. The major difficulty with silicone MEMS has been finding a way to pattern the silicone that allows for integration with other MEMS materials and processes. Therefore, photodefinable silicone is ideal for MEMS application as a microgasket or MEMS O-ring.

3.6.1 Photodefinable Silicone as a MEMS Material

Silicone rubber is a well-characterized, commonly used material in modern manufacturing. Silicones are composed of siloxane bonds, silicon atoms bound to each other by an oxygen atom, along with hydrocarbon radicals directly bonded to the free silicon valences. This structure places the properties of silicone between organic and

inorganic compounds. For example, silicone's Young's modulus is orders of magnitude smaller than most metals and silicon.

Silicones' small Young's modulus and low durometer (hardness) means silicones are especially well suited for compression-based sealing applications. In particular, their unique chemical properties make them a useful MEMS O-ring material [83]. Silicone rubbers have a broad operating temperature range, typically ranging from -60°C to 200°C , with fluorosilicone based elastomers going above 250°C . Additionally, silicones are porous and hydrophobic due to the open structure afforded by the flexibility of the siloxane backbone and freely orientated methyl groups. Simultaneously, silicones are permeable to steam and attacked at high temperatures. Most silicone rubbers are naturally transparent.

There are several challenges in using silicone as a MEMS material. The most limiting aspect of using silicone for the fabrication of MEMS devices comes in devising a method to pattern the silicone layer. Since most silicones are not UV sensitive, they can not be directly photopatterned. In addition, most silicones are not easily etched with chemicals or plasmas. For this reason, the most common method of patterning silicone is either through molding or replica casting, both of which are typical of PDMS-based microfluidic devices [83]. Silicones also exhibit poor adhesion to most common MEMS materials, such as silicon, glass, and metal. Special processing steps must be used to treat the silicone or the surface of the device to achieve good adhesion. Furthermore, cured silicone elastomers tend to swell in many organic solvents and oils [18]. They can also be attacked by strong acids and bases; hydrofluoric acid, in particular, reacts strongly with the siloxane backbone causing breakdown of the polymer.

In 2003, Dow Corning reported on the development of a UV photopatternable silicone (Figure 3-5) for application in the electronics packaging industry [84-86]. Dow Corning is attempting to develop a compressible electronic interconnect technology, but the availability of a commercially produced photopatternable silicone may have wider implications for MEMS. A photopatternable silicone can be used in surface micromachined devices as a flexible membrane, gasket, or O-ring. Dow Corning's WL-5150 represents the only soft, photodefinable material commercially available to the MEMS community. Dow Corning's processing parameters and photolithography results are listed in Table 3-3 and Table 3-4, respectively.

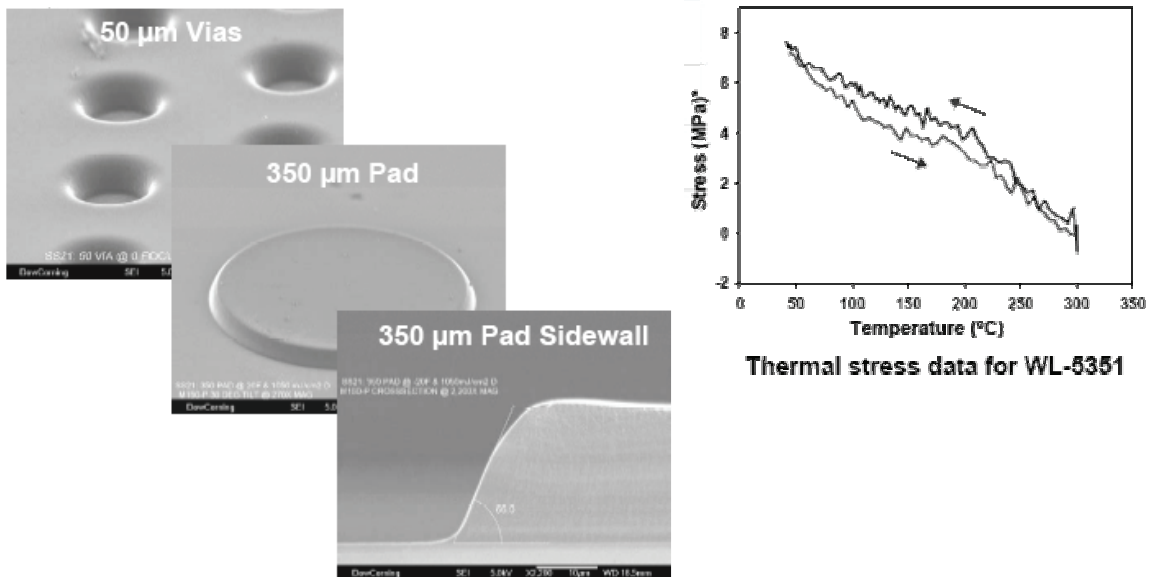


Figure 3-5. Photodefinable silicone from the Dow Corning Corporation [87]

Table 3-3. Processing Parameters for Dow Corning WL-5150 [87]

Process Step	Standard Conditions
<i>Spin Coat</i>	
a) Spread	500 rpm/10 sec
b) Spin	500-2500 rpm/30 sec
c) Edge bead	1500 rpm/30 sec
<i>Soft Bake</i>	Hot Plate 110°C/120 sec
<i>UV Exposure</i>	<i>i</i> -line or Broadband 1000 mJ/cm ²
<i>Post Exposure</i>	Hot Plate 150°C/120 sec
<i>Bake</i>	
<i>Development</i>	
	Solvent
a) Etch	60 sec NRD puddle
b) Spin rinse	NRD rinse 15 sec
	IPA rinse 15 sec
c) Spin dry	3000 rpm/30 sec
<i>Hard Bake</i>	
	Oven
	150°C/60 min or
	180°C/60 min or
	250°C/30 min

Table 3-4. Photolithography Performance of Dow Corning WL-5150 [87]

Process Property	Value
Film Thickness Range	15 to 40 μm
Minimal Feature Size	15 μm
Aspect ratio (h/w)	< 1.3
Height Uniformity	< 5%
Sidewall Slope	~ 60°
Film Retention	80 to 90%
Film Shrinkage (During Hard Bake)	~ 2%

WL-5150 is a negative photoresist, meaning UV exposure activates a cross-linking agent in the silicone precursor. An elevated temperature is used to aid in cross-linking the silicone film after exposure. Several experiments were carried out to determine if the post-exposure bake temperature of WL-5150 could be reduced. A reduced post-exposure bake would be beneficial to Parylene-based microfluidic processing because reduction of the post-exposure bake temperature would reduce any outgassing of the sacrificial photoresist layer during the bake. The experiments indicated that the WL-5150 processing is highly sensitive to temperature both for the prebake and

post-exposure bake. A comparable cross-linking strength was not obtained from post-exposure baking at lower temperatures, so later fabrication using WL-5150 was performed at the manufacturer's recommended temperature. Using pre- or post-exposure bake temperatures above the manufacture's recommendation resulted in a fully cross linked film, causing loss of photosensitivity. When post-bake temperatures below the recommendation were used a failure to fully cross-link exposed areas resulted, leaving a nucleated film that had many surface cracks (Figure 3-6). Such surface cracking or nucleation could cause leaks when the silicone is used as a gasket material and should therefore be avoided.

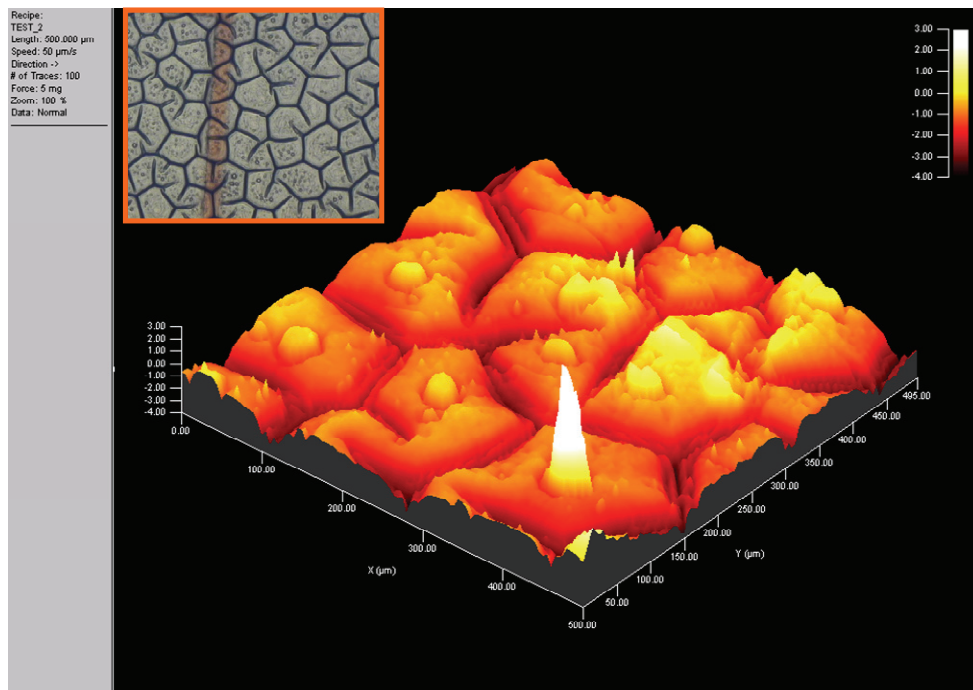


Figure 3-6. Surface profile of nucleated silicone due to insufficient post-exposure baking

3.6.2 Silicone Microgasket Fabrication

A process for microgasket and MEMS O-ring fabrication has been developed using Dow Corning WL-5150 as the gasket and O-ring material. Additionally, these

were tested using two fabricated microfluidic chips: 1) an interconnect chip which houses the microgasket and couple between the jig and dummy device chip, and 2) a dummy device chip that acts as a generic microfluidic device.

Interconnect and device chips are microfabricated using embedded Parylene microchannel technology. The fabrication processes for the two types of chip are nearly identical, although there is no requirement that the device chip be fabricated using the interconnect chip process. Cross-sectional diagrams of the fabrication process are shown in Figure 3-7. Soda-lime glass substrates were used for both device and interconnect chips.

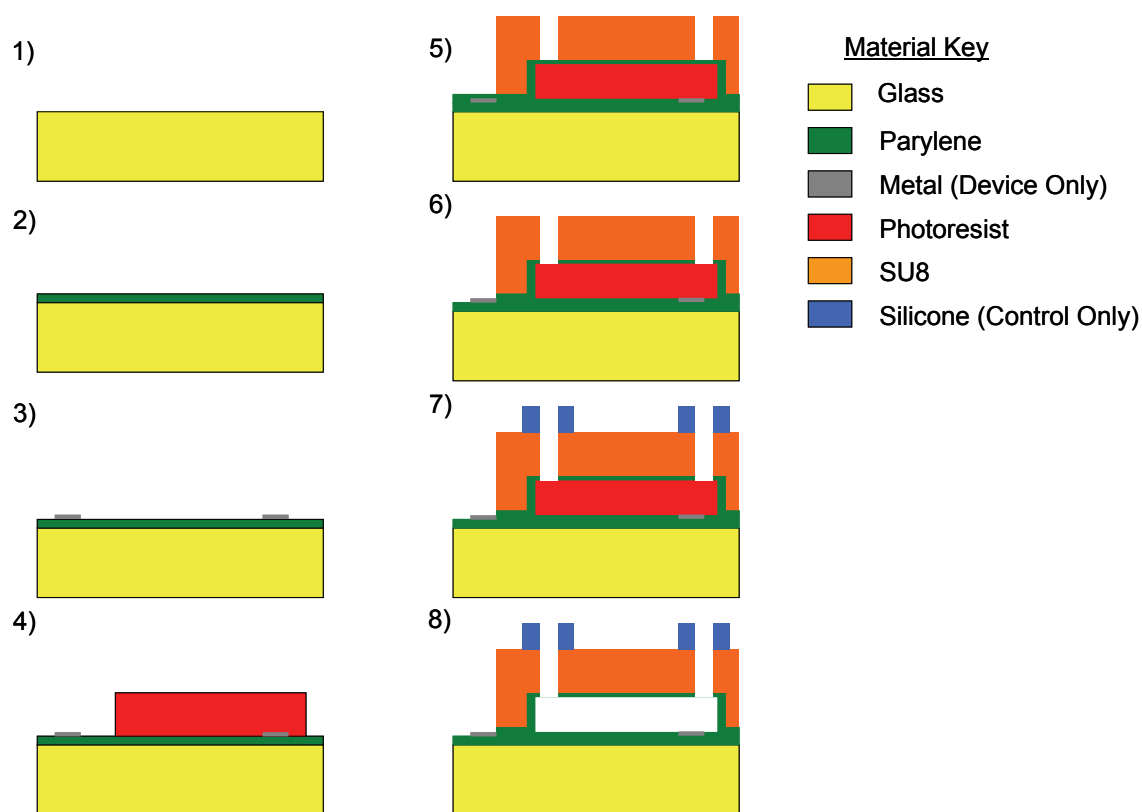


Figure 3-7. Cross-sectional diagram of device and control chip fabrication

The processes begin with a 3 μm layer of Parylene-C deposited on both devices, using silane-based A174 as an adhesion promoter. Next, a metal layer is added to the

device chip substrate by electron-beam evaporation and patterned by liftoff technique. Microchannels are formed by patterning thick photoresist (20 to 30 μm). This sacrificial layer of photoresist is then conformally coated with a second, 3 μm layer of Parylene. Subsequently, the surface of the wafer is planarized using a 65 μm thick layer of SU8. The SU8 is patterned to open the fluidic vias. The Parylene beneath the SU8 vias is then removed using oxygen plasma in a reactive ion etcher (RIE). The O_2 etch also roughens the SU8 surface, drastically increasing the adhesion of the photodefinable silicone to the SU8 (Figure 3-8).

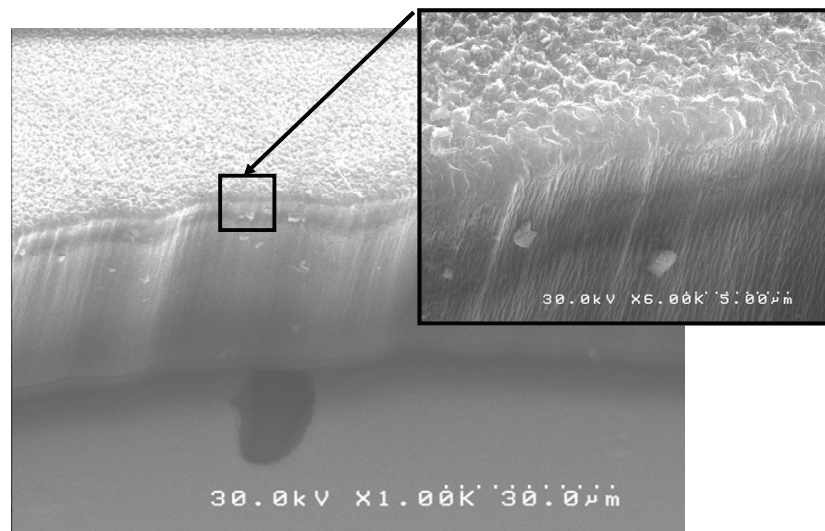


Figure 3-8. SEM of SU8 surface after O_2 etch. Closeup shows roughened surface.

For interconnect chip fabrication a layer of photodefinable silicone WL-5150 is spun on to a thickness of approximately 30 μm and patterned. After development of the silicone it is necessary to remove all residual silicone scum from the vias. The scum layer is removed using an SF_6/O_2 plasma in a RIE. A dry etching rate for the silicone of approximately 0.15 $\mu\text{m}/\text{min}$ was achieved using 75 sccm O_2 , 50 sccm SF_6 at 200 mtorr chamber pressure, and 180 W of RF power. Finally, the wafer is diced and the sacrificial

photoresist is released in isopropyl alcohol at 80°C. The SU8/silicone stack acts as the photodefinable microgasket (Figure 3-9). The silicone layer can also be patterned into annulus shapes around the vias to produce MEMS O-rings (Figure 3-10). When the chips are squeezed together, the silicone compresses, sealing the fluidic vias on the device chips.

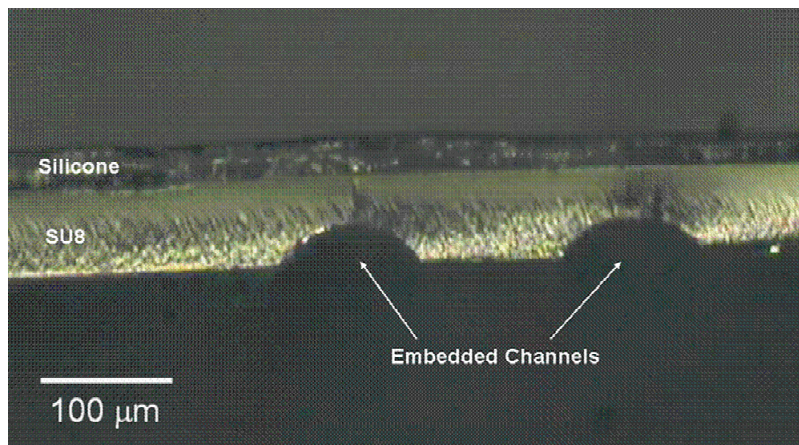


Figure 3-9. Cross section of gasket structure

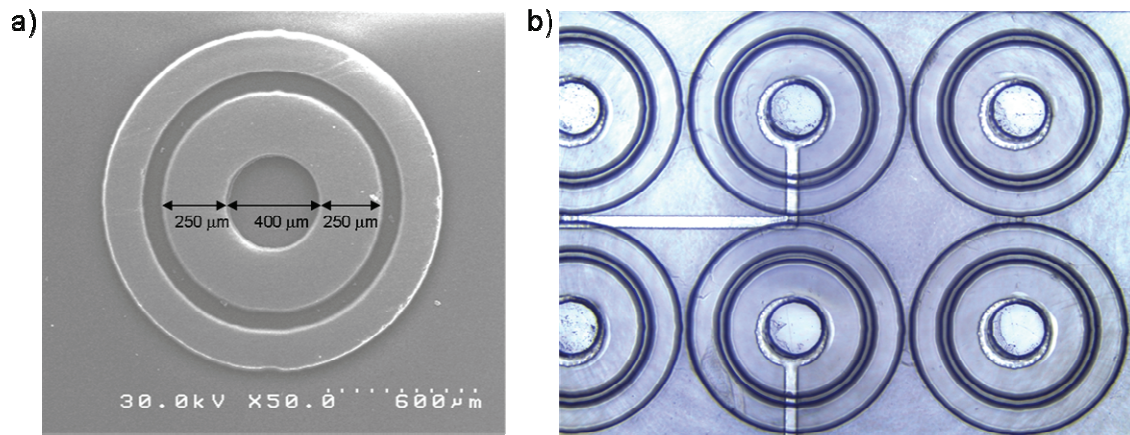


Figure 3-10. Images of MEMS O-rings. (a) SEM of a MEMS O-ring. (b) Photograph of array of MEMS O-rings with open vias and microfluidic channels beneath

3.6.3 Microgaskets and MEMS O-Rings Theory

For a proper seal, the microgasket must form an enclosed contact with the device chip around the vias. The gasket must also be under enough compressive force to both initially seat the gasket and overcome any hydrostatic end force developed by the internal fluid. For any gasketed-flange system to be leak-free the compressive force on each gasket supplied by the screws must exceed the hydrostatic end force applied to the flange by the fluid in the system. The analysis is similar to that of a single O-ring system as discussed in Section 3.5. This balance can be expressed mathematically for a multiple annular gasket geometry made from a self-energizing gasket material (gasket factor, $m = 0$) as:

$$H_G = M\pi\left(\frac{G}{2}\right)^2 P, \quad (3.6-1)$$

$$H_G \leq \frac{NT}{KD_f}, \quad (3.6-2)$$

where H_G is the hydrostatic end force, M is the number of identical gaskets under simultaneous compression, G is the diameter at location of gasket load reaction, P is the internal working pressure, N is the number of bolts, T is the torque on each bolt, K is the bolt friction factor (typically 0.20 for a dry bolt and 0.16 for a lubricated bolt), and D_f is the nominal bolt diameter [78]. The force balance and system geometry is depicted in Figure 3-11 for a two-device, single interconnect system. Using the ASME definition of G and rearranging equations (3.6-1) and (3.6-2) to show the maximum working pressure sustainable:

$$P_{\max} = \frac{4NT}{\pi MKD_f (D_g - W_g)^2}. \quad (3.6-3)$$

For a typical two-chip modular fluidic system $D_g = 900 \mu\text{m}$, $W_g = 250 \mu\text{m}$, and $M = 36$.

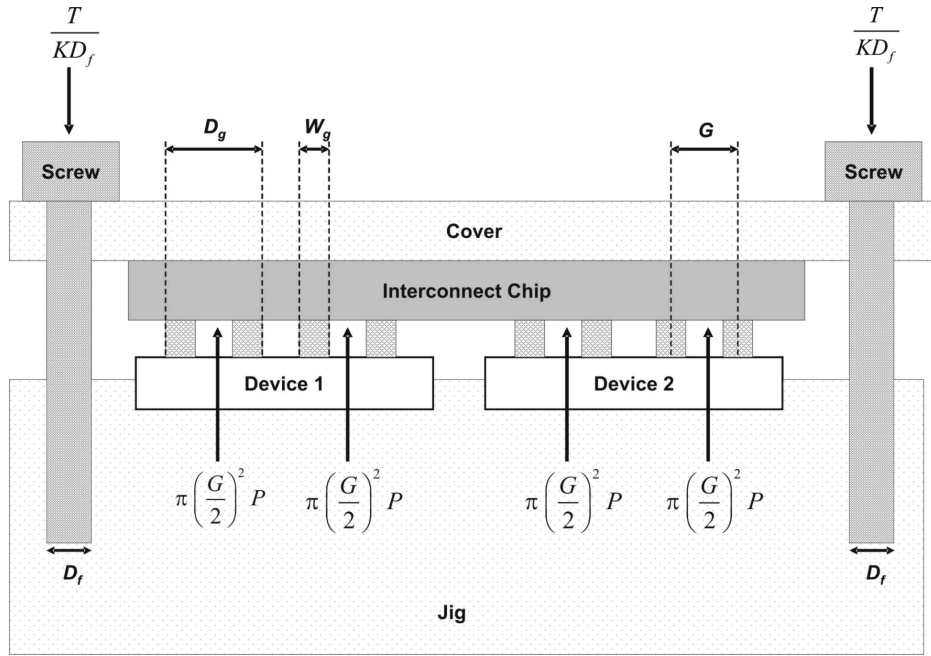


Figure 3-11: Force balance diagram of modular microfluidic system under compression

The flange surface profile plays a critical role in microgasket sealing behavior. Consider two types of microgaskets both of thickness, t , having maximum compressibility percentage, C_{max} , and minimum compression percentage required for sealing, C_{seal} . The first type of gasket is a flat gasket that covers the entire surface of the interconnect chip except the vias. The flange surface must have a global height minimum, y_{min} , and maximum, y_{max} . The second type of gasket is a patterned gasket, or MEMS O-ring, that has a sealing radius, r , that must be in contact with the device chip surface to seal. For the MEMS O-rings we define a local minimum, y_{min}^r , and local maximum, y_{max}^r , on the flange surface within a radius r of the via. To guarantee the flat gasket seals across the surface

$$y_{max} - y_{min} \leq (C_{max} - C_{seal})t. \quad (3.6-4)$$

For the MEMS O-rings to seal

$$y_{\max}^r - y_{\min}^r \leq (C_{\max} - C_{\text{seal}})t. \quad (3.6-5)$$

To guarantee simultaneous sealing of M MEMS O-rings with sealing radius, r_i

$$\max_{1 \leq i \leq M} [y_{\max}^{r_i}] - \min_{1 \leq i \leq M} [y_{\min}^{r_i}] \leq (C_{\max} - C_{\text{seal}})t. \quad (3.6-6)$$

Note that for the M MEMS O-rings as M grows this case collapses into the flat gasket condition of equation (3.6-4). For a particular gasket thickness, maximum compressibility, and minimum sealing compression, equations (3.6-4) and (3.6-6) bound the allowable surface height variation of the flange. Even without exact parameters, using this worse-case analysis, we can conclude that patterned gaskets, specifically O-rings, can do no worse than the flat gasket and typically will do better.

3.6.4 Silicone Microgasket Compression Testing

As the screws are tightened on the jig a compressive stress develops in the gasket causing it to deform and seal the fluidic vias. The amount of compressive stress achieved as a function of uniform screw torque can be calculated as:

$$\bar{S}_g = \frac{NT}{A_g KD_f}, \quad (3.6-7)$$

where A_g is the total gasket surface area and all other variables are defined as before. During the compression and leak rate tests, a flat gasket under uniform compression was used. A flat gasket, as opposed to a patterned gasket, was necessary to achieve a significant range of compressive stress given the resolution of the torque wrench. To achieve uniform compression each screw was tightened with a torque wrench in 2 in-lb increments in a crisscross pattern until the final desired torque was reached.

An indirect measurement technique based on parallel-plate capacitance sensing was used to monitor the change in thickness. The first capacitor is formed by SU8 with a reported relative permittivity, ϵ_r , of 4 and is assumed to be fixed [88]. The second capacitor is formed by the silicone and is expected to vary as the silicone is compressed. The silicone manufacturer reports a relative permittivity of 3.2 at 1 MHz [87]. The ratio of the change in capacitance to the initial capacitance is a function of the thicknesses and relative permittivities of the layered materials, and can be expressed as:

$$\frac{\Delta C}{C_0} = \frac{\epsilon_{r,SU8} (t_{silicone}^0 - t_{silicone}^c)}{t_{SU8} \epsilon_{r,silicone} + t_{silicone}^c \epsilon_{r,SU8}}, \quad (3.6-8)$$

where 0 indicates pre-compression conditions, c indicates conditions under compression, C is capacitance, t is thickness, and ϵ_r is relative permittivity. The surface area is assumed to be unchanged by the compression. Using this model, the compressibility of the microgasket can be measured as a function of compressive stress (Figure 3-12). The silicone can compress to approximately 25% of its initial thickness and is fully compressed by a compressive stress of 750 psi.

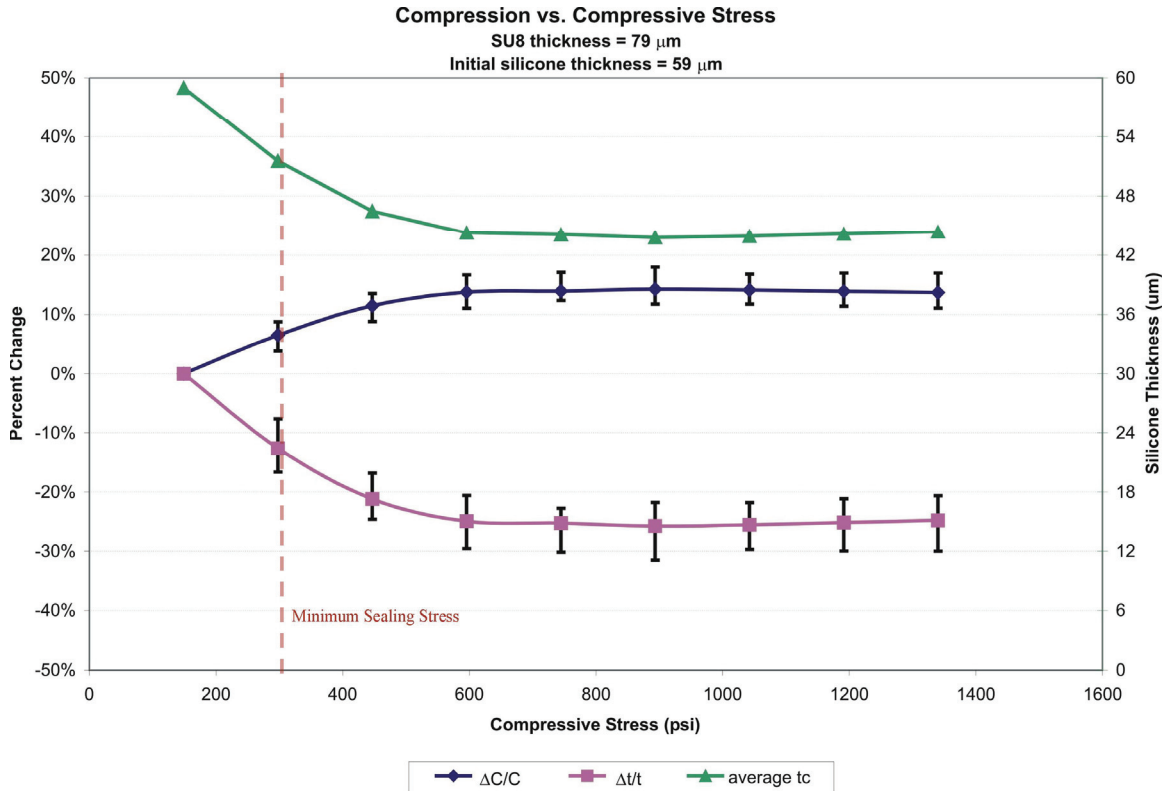


Figure 3-12: Compressibility of SU8/silicone microgasket. Each data point represents the average of five measurements at the indicated compressive stress and the error bars mark the minimum and maximum values obtained during all trials (only average data for compressed silicone thickness is shown). The capacitance (blue diamonds) and thickness (purple squares) change data is plotted against the left axis while the average thickness data (green triangles) is plotted against the right axis. Data shows a maximum compressibility of 25% and a minimum sealing compressibility of approximately 12%.

3.6.5 Silicone Microgasket Sealability

The leak rate of a system consisting of a single device chip and an interconnect chip was measured. A constant volumetric flow rate test at 5 $\mu\text{L}/\text{min}$ showed the system sealed between 300 and 400 psi of compressive stress with no measurable leak rate for compressive stresses at or above 300 psi. This corresponds to a minimum sealing compressibility of approximately 12%.

In the second test, a constant compressive stress of approximately 1100 psi was applied to fully compress the gasket. The system was then filled with food coloring to aid in visualization of fluid flow. The outlet port on the jig was sealed using a screw and

Teflon tape. Varying amounts of pressure were applied using pressurized nitrogen gas. The change in position of the fluid front was monitored over time to determine the system leak rate. Leak rates below 2.3 nL/min were observed for all inlet pressures below 250 psi with no observable leak below 50 psi (Figure 3-13).

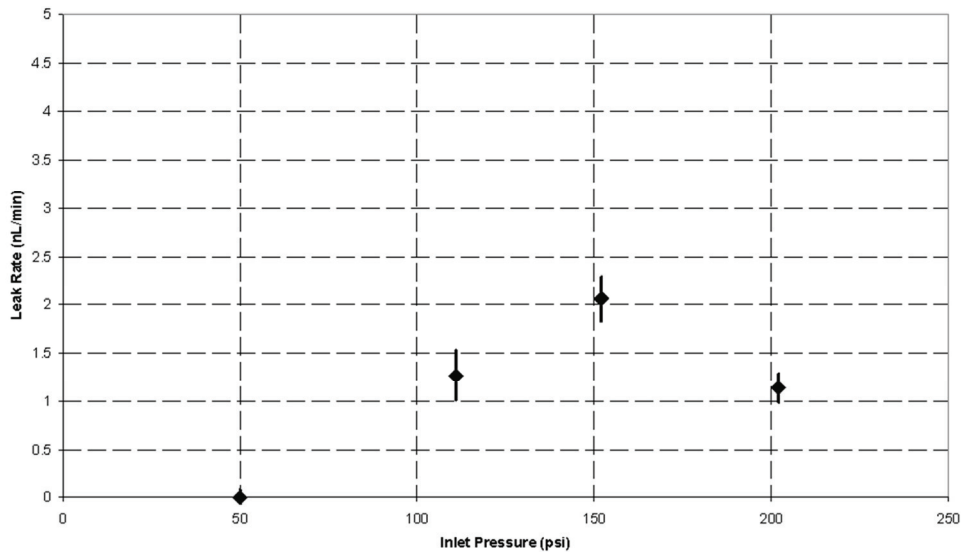


Figure 3-13. Leak rate test results. Maximum leak rate is 2.3 nL/min with no observable leak below 50 psi operating pressure. Error bars show uncertainty in measurement.

The leak rate reported here is that of the entire system. It is believed that the microgaskets did not leak but instead the observed leak was from the commercial fittings and plug screw. No leaking could be observed from the microgasket regions under the microscope. The system failed at inlet pressures above 250 psi. The failure occurred in the embedded Parylene channels when the two layers of Parylene delaminated under high pressure. This failure mode was observed in all trials at approximately 250 psi. No other failure mode was observed. High-pressure Parylene channel designs have been reported and their incorporation into future devices could allow working pressures over 800 psi [38].

The failure of the embedded channel structure at 250 psi has precluded experimentally determining the maximum sustainable working pressure of the microgaskets. The microgasket theory predicts high working pressures, but also shows that surface profile variations of the device chips can cause sealing problems. While it is possible to achieve sealing using flat gaskets, these systems have been experimentally limited to a single device chip. To extend the usefulness of this design concept, multiple device chips must be sealed simultaneously. The MEMS O-rings offer a superior gasket geometry proven to seal across multiple devices. MEMS O-rings were used to simultaneously seal between one and three device chips to the interconnect chip.

The microgaskets and MEMS O-rings proved to be reusable under practical operating conditions. The main factor effecting reusability is adhesion of the gasket to the flange after initial compression. If the microgasket or MEMS O-ring sticks to the flange after the compressive stress is removed, the force required to separate the two components typically destroys the silicone layer. Adhesion problems can be greatly reduced by limiting the initial compressive stress applied to the gasket material. We found a significant increase in adhesion incidences when compressive stress above 600 psi was used to seal the system. For compressive stress in excess of 1000 psi, the flange edge was observed occasionally biting into the gasket material with enough force to cause either a permanent rip or deformation in the material (Figure 3-14). Reused gaskets were not observed to have degraded in performance; however, exhaustive testing was not performed.

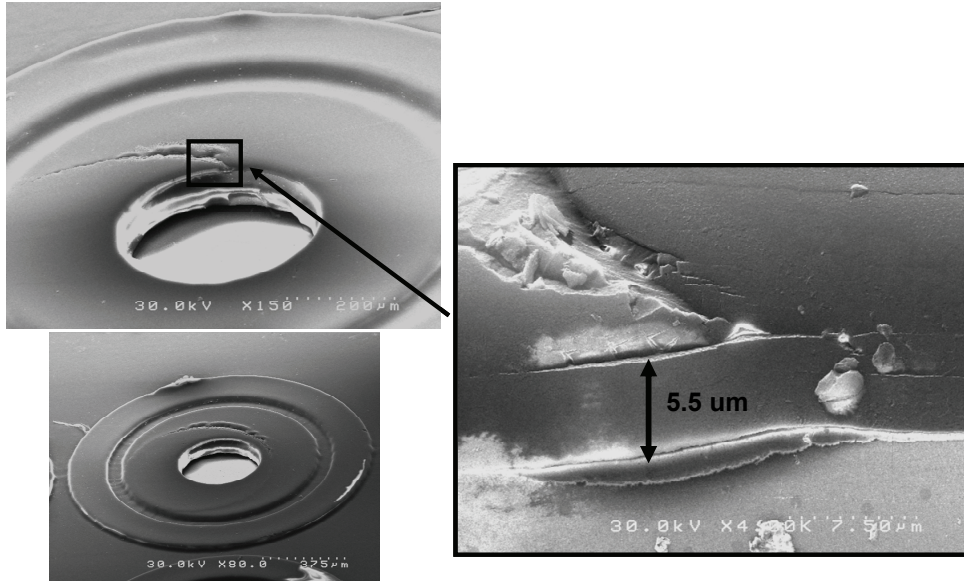


Figure 3-14. MEMS O-rings after excessive compressive stress was applied to seal the system. Initial gasket thickness was between 28 and 30 μm .

Experimental observations also suggest that the relative shape of the vias on the device and interconnect chips is important in establishing a good seal. Three circular geometries were studied: smaller device vias, smaller interconnect vias, and same-size vias. All three geometries were capable of establishing a seal but, when used in multiple device systems, smaller interconnect vias were the most robust (able to seal the most vias simultaneously). We believe this is because the smaller interconnect vias have a portion of the gasket material that overlaps the edge of the device via (Figure 3-16). It is at this point of overlap that the strongest seals are formed because the gasket material deforms into the device via instead of merely being compressed around it. This effect is similar to that of a raised-ridge design in a standard gasketed-flange system. All multiple device systems used for testing were designed with the smaller interconnect via geometry.

3.6.6 Via Dead Volume

Another concern of any microfluidic system is the minimization of dead volume. For purposes of quantitative assessment, we will define the dead volume in the via as that volume of liquid that achieves a fluid velocity less than 1% of the inlet flow velocity to the via [70]. The three-dimensional flow velocity profile for a 4 mm/sec inlet flow velocity of room-temperature water was numerically simulated using COMSOL Multiphysics Package with Matlab based on the fabricated via geometry (Figure 3-15). Using the finite element simulation the dead volume in the via is estimated to be approximately 9 nL for 750 μm diameter vias. The dead volume can be minimized by reducing the channel diameters and the inner gasket and flange diameters subject to the alignment constraints. Using optimal via geometry for 100 μm x 25 μm channels, the dead volume was reduced to approximately 1 nL per via (Figure 3-16 and Table 3-5).

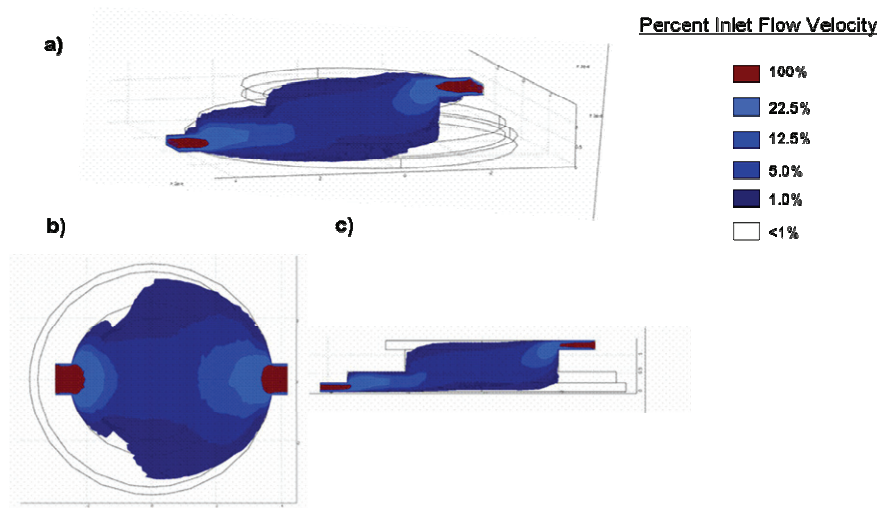


Figure 3-15: Numerically simulated fluid flow velocity profile through a via. Surfaces of different colors indicate relative flow velocity (100%, 22.5%, 12.5%, 5%, and 1%) compared to the inlet velocity. White area indicates a relative flow velocity less than 1% and hence depicts the dead volume in the via. (a) Perspective view. (b) Top view. (c) Side view.

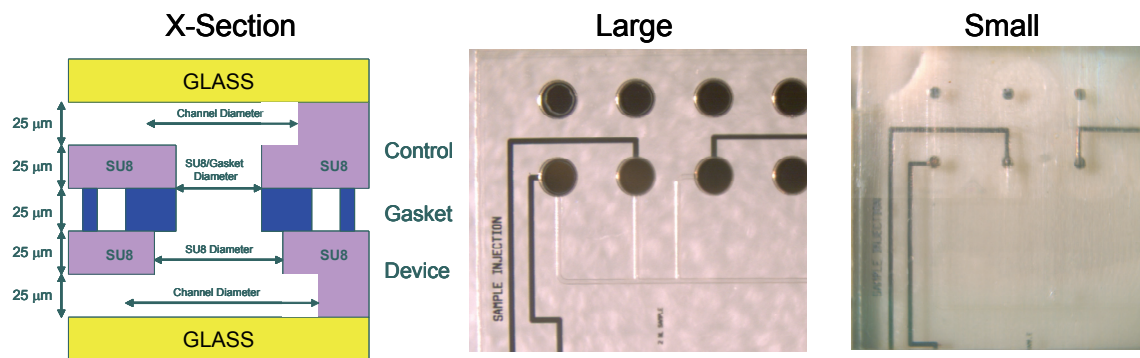


Figure 3-16. Different fabricated via geometries and cross sectional diagram

Table 3-5. Details of Different Fabricated Via Geometries

Device channel diameter:	750 μm	250 μm
Device SU8 diameter:	700 μm	200 μm
Gasket/SU8 inner diameter:	400 μm	115 μm
Control channel diameter:	500 μm	150 μm
Total Via Volume:	31.86 nL	2.97 nL
Est. Dead Volume*:	9 nL	0.85 nL

* Assuming ideal alignment.

3.7 Conclusions

A major challenge in developing appropriate devices for many microfluidic applications remains in how to package and connect the various components [89]. Bridging the micro/macro divide is the fundamental problem facing device packaging and is particularly difficult in the area of fluidics. Fluidic packaging is not just a matter of simple connectivity, as in electronic interconnects, but one of geometry and material as well since these factors can influence device performance through dead volume effects and reagent compatibility. Hence, microfluidic packaging that exhibits low leak rates, high maximum sealing pressures, no clogging, chemical inertness, low dead volume, integrated fabrication, and user friendliness has been desired for almost ten years, yet has

proven elusive [61]. Researchers have suggested a variety of techniques involving glues, epoxies, specially fabricated couplers, press fit tubing, gaskets, and O-rings.

The introduction here of a robust, easy-to-use, fully integrated interconnect technology makes the possibility of widespread interchangeable microfluidic devices and complex modular microfluidic systems feasible. The microgasket sealing theory confirms the feasibility of surface micromachined gaskets for use in modular microfluidic systems. It is concluded that MEMS O-rings are superior over unpatterned gaskets. As the complexity of microfluidic systems increase, the need to independently design and fabricate system components will become greater for many applications and so will the value of integrated interconnect technologies such as photodefinable silicone microgaskets and MEMS O-rings.

4 MODULAR MICROFLUIDIC NANO HIGH-PERFORMANCE LIQUID CHROMATOGRAPHY

4.1 Modular Microfluidics

Almost all published fluidic packaging work addresses bridging the macro/micro divide, but a few scientists and engineers have proposed developing multiple microfluidic systems that do not involve a macro scale interface between various micro components. These multiple device systems that do not require macro scale interconnects are referred to as modular microfluidic architectures. A modular microfluidic architecture is advantageous over individual devices. For example, modular design allows for increased system flexibility by allowing devices with incompatible fabrication processes to be combined at the system level. Additionally, modular design contributes to increased system robustness by enabling broken components to be individually exchanged without replacing the entire system, individual device optimization without system fabrication, and generic device design.

Shaikh et al. [26] developed a complex but functional PDMS-based modular microfluidic architecture that requires through-wafer deep reactive ion etching to form the fluidic vias and multilayer PDMS processing to make the devices, but lacked electrical components. Suk et al. [13] also used PDMS to make a modular microfluidic system that incorporated electrical, as well as fluidic, interconnects. In this system,

PDMS forms interconnects between the device chips in addition to forming microchannels on the device chips. In both cases, PDMS bonding was used to seal the multi-device system.

A valuable addition to the search for a modular architecture is a system capable of operating at high working pressures with no chemical compatibility limitations. In the following sections, a unique modular architecture is presented, along with high-efficiency nitrate/nitrite separation data. The separation data shows no significant degradation in performance due to the modular design. Accordingly, this chapter will consist of three sections: 1) A discussion of the modular fluidic packaging scheme, 2) an introduction to nano high-performance liquid chromatography (nHPLC), and 3) a description of the modular nHPLC system used for nitrate/nitrite separation, along with a presentation of separation results.

4.2 Microfluidic Jig Design

This work presents an easy-to-reconfigure modular microfluidic system architecture that allows replacement of device and control chips; up to 12 fluidic and 12 electrical interconnects per device chip; four re-usable, independent device chips; and is compatible with embedded Parylene microfluidic technology (Figure 4-2a). The system consists of a chemically resistant polyetheretherketon (PEEK) body. The PEEK body is machined into a jig that has cutouts for four microfabricated device chips and one control chip. The backside of the jig has twelve fluidic ports used with commercial tubing and fittings to couple fluid into the system. Small O-rings are utilized to seal the fluidic connection from the jig to the control chip. The control chip is fabricated on a soda-lime glass substrate for optical transparency and incorporates a novel, integrated microgasket

(see Section 3.6) that seals the vias between the control and device chips. The entire system is compression-sealed using four screws and an acrylic cover piece. Electrical connections to the device chips can be made using pogo-pegs (Interconnect Devices Inc., Kansas City). The pogo-pegs make contact with metal pads on the device chips and can be soldered to or compressed against a custom PC board, allowing for routing of the 48 electrical connects and integration with other electrical components of the system (Figure 4-1a and Figure 4-1c).

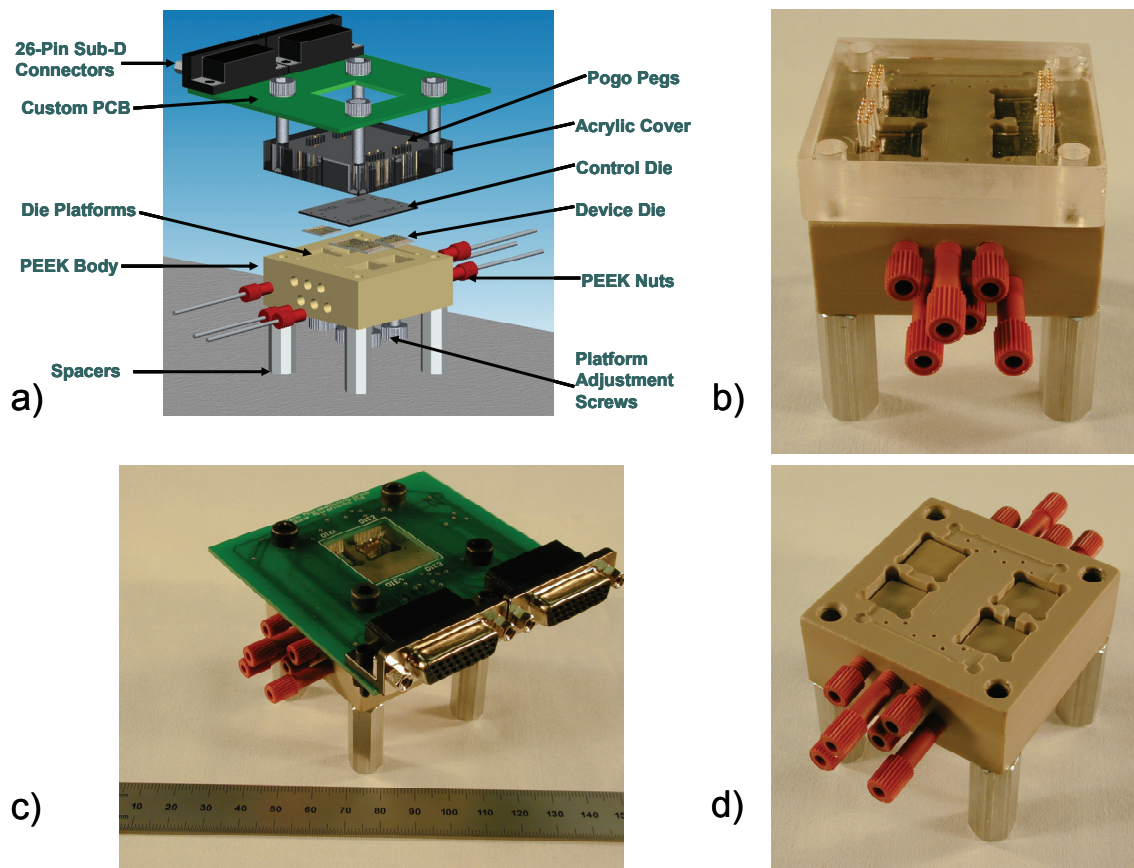


Figure 4-1. First attempt at modular microfluidic jig. (a) Computer rendering. (b) Side view without PCB and control chip. (c) Perspective view with all components. (d) Top view without PCB, cover, or chips

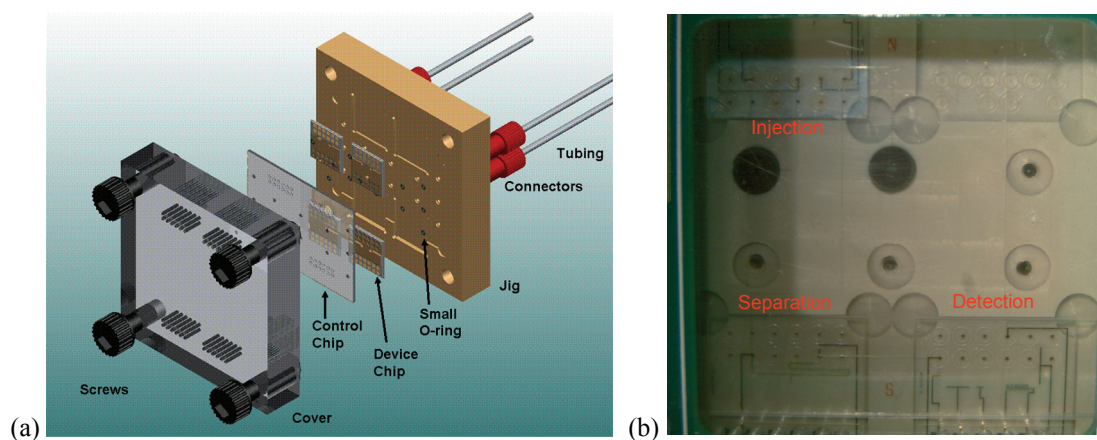


Figure 4-2. Final jig design for modular microfluidic system. (a) Exploded view of modular microfluidic system. Not shown are the pogo-pegs for electrical interconnects and the PC board. (b) Assembled modular microfluidic system with injection, separation, and detection device chips. The 1 cm separation column is dyed green to aid visualization.

The jig is made from PEEK sheet and is computer-numerical-controlled (CNC) machined, which makes the system self-aligning. Alignment is one of the major challenges in modular microfluidic systems. Using this jig, the control chip and device chips can typically be aligned to within 50 μm . The alignment error results from the jig's machining tolerances and the accuracy of the chip dicing and is one source of dead volume in the microfluidic system. Complete mechanical drawings for the circuit board, jig, and acrylic cover are in Appendix A. Microfabricated mechanical alignment structures have been suggested to aid in multiple device alignment in modular microfluidic systems [90] and similar structures can be incorporated into this design.

Properly sealing the system requires torque be carefully applied to the four screws. Experience has proven that the best way to seal the system is to start all four screws finger-tight. Next, the torque should be increased on the screws in 2 in-lb increments in an alternating pattern until a total of 6 in-lb of torque is achieved on each screw. Too much torque on the screws can result in two problems. Firstly, the maximum

safe compressive stress on the microgaskets will be exceeded, causing damage. Secondly, the mechanical deformation of the jig body or acrylic cover could cause the control chip to separate from the device chips, resulting in a leak. The jig body and acrylic cover thickness should be sufficient to produce minimal bending at operational loads on the screws.

4.3 High-Performance Liquid Chromatography

High-performance liquid chromatography is the dominant analytical separation tool in many industries. It is extensively used in the pharmaceutical and chemical industries, as well as in environmental and biochemical laboratories. Modern HPLC emerged in approximately 1973 with the development of column packing techniques that could reproducibly pack a separation column with 10 μm particles [91]. Chromatography describes any separation technique based on the differences in relative migration velocities of analytes and typically involves a stationary and a mobile phase. Typically during liquid chromatography, the mobile phase is a liquid and the stationary phase is a column of tightly packed silica beads with diameters of 10 μm or less. As the mobile phase passes through the stationary phase, the analytes in the mobile phase interact with the stationary phase. Each analyte interacts differently giving each a different migration velocity. Due to the differences in migration velocity, analytes will elute, or exit, the stationary phase at different times (Figure 4-3). High-performance chromatography simply refers to the high pressures used to reduce separation times. When HPLC is used for analytical studies, the eluent must be passed through a detector. Many different types

of detectors are used in HPLC but some of the most common are mass spectrometry, ultraviolet absorption, laser-induced fluorescence (LIF), electrochemical, and conductivity.

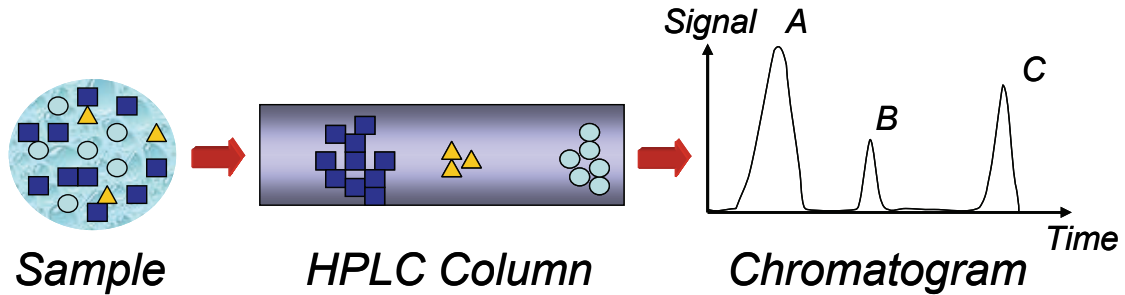


Figure 4-3. Illustration of analytical liquid chromatography

As the analytes travel through the separation column, they are separated by their different migration velocities and simultaneously brought closer together by diffusion. The longer they remain in the column, the more time they have to diffuse toward one another. The effect of diffusion can be seen most easily on a chromatogram as an increase in the peak width. Chromatography works because the band broadening effects of diffusion scale at a slower rate relative to the band separating effects of differential migration. More specifically, the band width scales as the square root of the length traveled along the column, while the band separation scales linearly with the length traveled. The resolution of the separation, R_s , can then be said to scale as follows [91]:

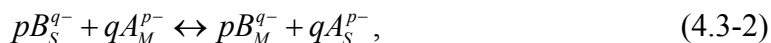
$$R_s \propto \frac{\Delta L}{w} \approx \frac{L}{\sqrt{L}} = \sqrt{L} . \quad (4.3-1)$$

Equation (4.3-1) indicates that separations are possible even with very short columns. Although this follows theoretically, the initial band width caused by finite injection volume places limits on minimum column length.

Traditional, or normal-phase, chromatography was performed with a polar stationary phase and a nonpolar mobile phase, but this has been replaced in 70 to 80% of chromatography applications with reverse-phase chromatography, which has a nonpolar stationary phase and polar mobile phase [91]. Other chromatography variants include hydrophobic interaction chromatography, ion-exchange chromatography, and size-exclusion chromatography. Of particular interest to this work is ion-exchange chromatography because of its applicability to the separation of inorganic ions.

4.3.1 Ion-Exchange Chromatography Theory

Ion-exchange chromatography requires a separation column packed with functionalized silica beads with a fixed charge. If the fixed charge on the beads is negative, the column is a cation exchange column, whereas if the fixed charge is positive, it is an anion exchange column. The fixed charge on the beads must be neutralized by an equivalent counter ion. Separation is accomplished as ions in the mobile phase pass pores on the silica beads and some of the analyte ions enter the pores in exchange for some of the counter ions (Figure 4-4). Consider the generic anion exchange system with analyte A^{p-} , counter ion B^{q-} , and fixed charges C_S^+ in equilibrium:



where subscript S indicates stationary phase and subscript M indicates mobile phase. If the charge on the counter ion is monovalent ($q = 1$) then the retention factor, k , is

$$k = \frac{V_S}{V_M} K_{\text{ex}} \frac{[C_S^+]^p}{[B_M^-]^p}, \quad (4.3-3)$$

$$K_{iex} = \frac{[A_S^{p-}]^q [B_M^{q-}]^p}{[B_S^{q-}]^p [A_M^{p-}]^q}, \quad (4.3-4)$$

where V_S is the volume of stationary phase, V_M is volume of the mobile phase, [] indicate concentration, and K_{iex} is the equilibrium constant.

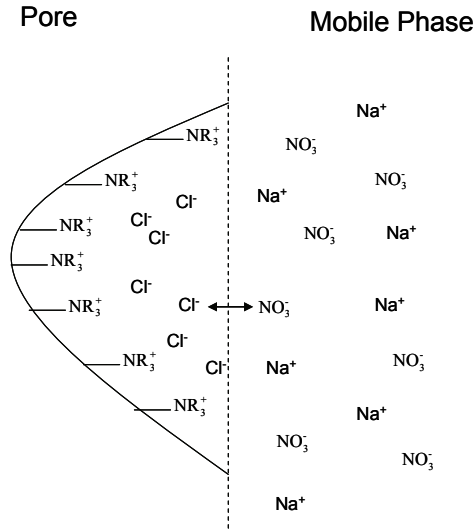
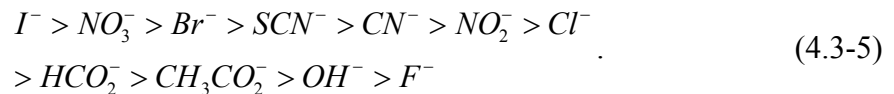


Figure 4-4. Illustration of anion exchange principle. The counter ions (Cl^-) are exchanged for the analyte anions (NO_3^-).

From equation (4.3-3), it can be shown that the retention factor is a function of the analyte charge, p , as well as the analyte size and polarizability (factors affecting the equilibrium constant). Experimental results have determined a relatively consistent elution strength scale (listed in order of highest retention factor to lowest retention factor) for common monovalent anions [91]:



Elution order will vary inversely with retention factor. Hence, we can expect to see Cl^- elute off of the stationary phase before I^- .

4.3.1.1 Sample Injection

Sample plug volume is a critical factor in isocratic liquid chromatography. Because the analytes are not concentrated on the column and separately eluted, the sample plug volume must be much less than the separation column volume to achieve separation. In macro HPLC systems with typical column lengths in excess of 10 cm and column diameters as large as several millimeters, sample plug volumes in the 0.1 μL to several μL range are acceptable. On-chip HPLC columns, however, are much smaller. In the case of the system presented in Section 4.3.2, the column is $0.1 \times 0.025 \times 10 \text{ mm}^3$, a column volume of approximately 25 nL. Such small column volumes necessitate extremely small sample plugs. The ideal maximum sample volume can be roughly estimated from the packing bead diameter, d_p , column cross-sectional area, A_c , and column length, L , according to [92] :

$$V_{s,max} = 0.85 A_c \sqrt{L d_p} . \quad (4.3-6)$$

For a 1 cm column packed with 7 μm beads, the maximum sample volume corresponds to approximately 2.25% of the column volume. Reliably injecting sub-nanoliter plugs is extremely difficult because this volume often exceeds the displacement volume of external valves used to switch fluid flow from the buffer and sample channels.

4.3.1.2 Peak Analysis

For many sensing mechanisms used in HPLC, the output is a chromatogram. The chromatogram shows the sensor response as a function of time. Typically chromatograms contain several peaks, each related to an individual analyte.

Understanding the distribution of the peaks allows the user to investigate the composition of the sample and the efficiency of the separation. A typical chromatogram with two peaks is shown in Figure 4-5.

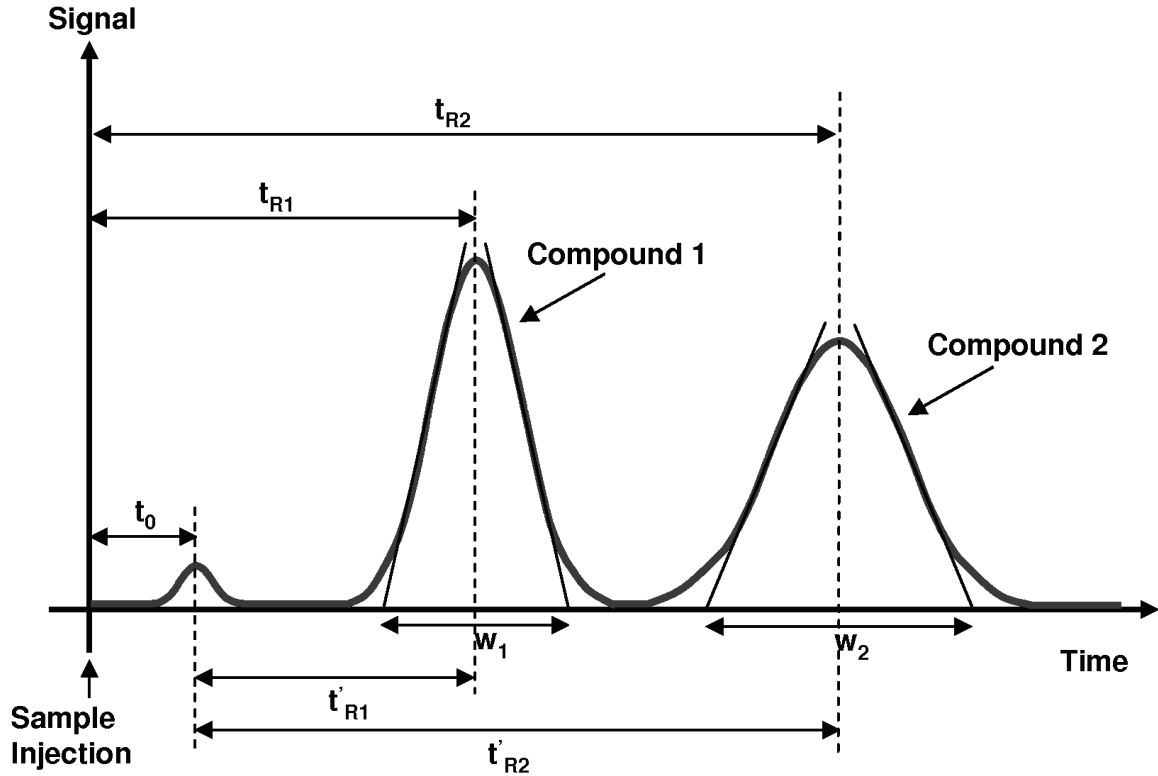


Figure 4-5. Illustration of a typical chromatogram showing two analyte peaks. Break through time, t_0 , retention times, t_{R1} and t_{R2} , and peak widths, w_1 and w_2 , are indicated.

In the past, peak analysis was performed by manually measuring the peak widths. The peak variance was then estimated using simple formulas. Today, peak analysis can be performed using computers to fit the peaks to Gaussian profiles. Each peak is independently fit using three fitting parameters (a , μ , σ) to the following equation:

$$I(t) = a \exp \left[-\frac{(t - \mu)^2}{2\sigma^2} \right]. \quad (4.3-7)$$

Using the mean, μ , and standard deviation, σ , determined from the curve fits, estimated retention times, t_R , and peak variances, σ^2 , are obtained. Retention time is calculated as

the fit mean minus the time at the end of the plug injection. The peak current, I_p , is calculated by subtracting the peak current in the data from the baseline current. Three commonly used separation efficiency metrics can then be calculated:

$$N = \frac{t_R^2}{\sigma^2}, \quad (4.3-8)$$

$$A_s = \sqrt{\frac{(t_{5\sigma})^2}{(f_{5\sigma})^2}}, \quad (4.3-9)$$

$$R_s = \frac{R_{t,2} - R_{t,1}}{2(\sigma_2 + \sigma_1)}, \quad (4.3-10)$$

where N is the number of theoretical plates in the column, A_s is a measure of peak asymmetry, $f_{5\sigma}$ is the width of the peak from the moment the signal passes 4.4% of the maximum peak current until the peak current is reached, $t_{5\sigma}$ is the width of the peak from the time the peak current is reached until the moment the signal passes 4.4% of the maximum peak current, and R_s is a measure of resolution between analytes 1 and 2 [93].

4.3.1.3 Amperometric Detection

A common technique used for detection in HPLC systems is direct current (dc) amperometry. DC amperometry is a form of electrochemical detection. Amperometric detection works by establishing a potential on one electrode and measuring the current through a second electrode also in contact with the test solution. In DC amperometry the applied potential is constant and the current is recorded as a function of time which makes this a special case of chronoamperometry. Other electrochemical detection techniques make use of time varying potentials. As with all electrochemical detection

techniques, DC amperometry is a selective detection mechanism that relies on the electroactivity of the target analytes.

The selection of the applied, or detection, potential is critical. Different molecules will undergo reduction or oxidation (redox) at different working potentials. Furthermore, the transition from active to inactive is not sharp, but instead extends over a range of potentials and conversion efficiencies. The effects of proper selection of the detection potential are illustrated in Figure 4-6. If analyte *a* is of primary interest, selecting potential E_1 is optimal. If analyte *b* is of primary interest than a potential between E_2 and E_3 should be chosen such that peak blending is minimized. If just analyte *c* is of interest than potential E_4 is the most useful. In any separation system, there will always be multiple analytes and therefore, the measured signal is a complex mix of several elements.

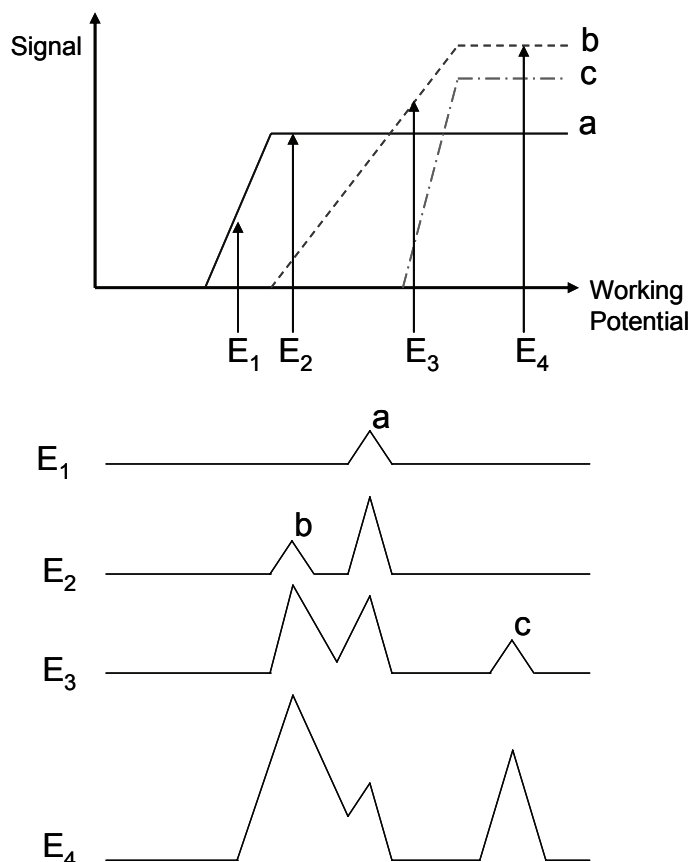


Figure 4-6. Relationship between voltammetric response of compounds *a*, *b*, and *c* and the applied potential on the selectivity in HPLC [94]

The total current measured by an amperometric detector is the sum of three contributing currents:

$$i_{total} = i_{F(analyte)} + i_{F(background)} + i_{NF(capacitive)}, \quad (4.3-11)$$

where F indicates a faradaic current, current resulting from oxidation or reduction, and NF indicates a non-faradaic current, current resulting from the movement of ions. The desired signal is the analyte redox current which should be optimized by selection of a proper detection potential. The major source of background current is the oxidation or reduction of species other than the analyte of interest. In most HPLC systems, the most worrisome interfering species is water. The applied potential must be kept between the oxidation and reduction potentials for water, called the “water window.” Working

electrode material, buffer composition, and pH can all affect the exact size and location of the water window. The water window typically does not extend to potentials below -1.2V or above +1.2V [95]. Use of totally nonaqueous buffer systems can extend the working potential range but are not typically seen in HPLC applications. In DC amperometry systems, fixed potential operation naturally minimizes the non-faradaic component because there is no need to continuously redistribute charge in the double layer (see Section 5.2.1).

4.3.2 A Modular nHPLC System for Nitrate/Nitrite Detection

A modular nHPLC-ECD was designed for the separation and detection of nitrate and nitrite. The goal of this system is to demonstrate the feasibility of using a modular microfluidic design approach to the construction of a high-quality on-chip separation system. The modular nHPLC-ECD system consists of an injection, separation, and electrochemical detection device (Figure 4-7 and Figure 4-2b). The injection device is designed for use in a novel, valveless injection scheme capable of repeatable insertion of nanoliter volume sample plugs into the buffer flow stream. The separation column is 1 cm in length and is packed with 7 μm diameter poly(styrene-divinylbenzene) (PS-DVB) anion exchange beads functionalized with trimethyl-ammonium ions ($[\text{NH}(\text{CH}_3)_3]^+$). The electrochemical detector consists of several working electrode designs and a large counter electrode.

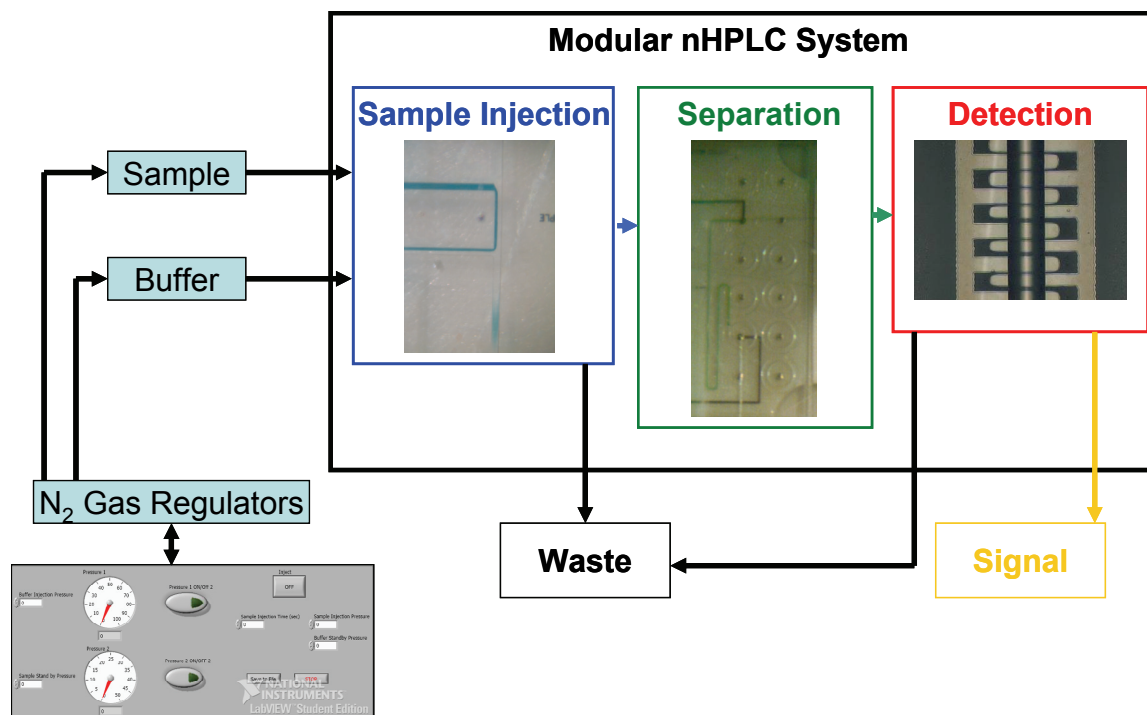


Figure 4-7. Schematic of nHPLC system

The fluidic via volume was minimized and resulted in an estimated dead volume of 0.85 nL per via where dead volume is defined as the volume of fluid in the via exhibiting a flow velocity less than 1% of the inlet flow velocity [70]. The major concern with any modular separation system is that the dead volume between the separation column and the detector will cause unacceptable amounts of band broadening. The goal of this work is to show that this modular design has sufficiently minimal band broadening effects due to via dead volume. The relatively large dead volume in the jig to chip interconnects does not effect separation efficiency since the sample injection, separation, and detection occur without passing through these interconnects.

4.3.2.1 nHPLC Component Microfabrication

The control and device chips are microfabricated using the embedded Parylene microchannel technology discussed in Sections 1.2.2 and 3.6.1. The fabrication processes for the two types of chips are nearly identical, although there is no requirement that device chips be fabricated using the control chip process. Cross-sectional diagrams of the fabrication process are shown in Figure 4-8. Detailed fabrication recipes for the control and device chips are available in Appendices B and C, respectively. Soda-lime glass substrates were used for both device and control chips. Photographs of three types of device chips after fabrication are shown in Figure 4-9.

A 3 μm layer of Parylene-C is deposited on both devices using Silane A174 (Specialty Coating Systems) as an adhesion promoter. A metal layer is added to the device chip substrate by electron beam evaporation and patterned by lift off. Microchannels are formed by first patterning approximately 25 μm photoresist. The photoresist is patterned using a two-step, two-mask exposure to allow for shorter channel heights in select sections of the channel. The shorter sections are used as particle filters during bead packing (see Section 4.3.2.2). The sacrificial layer of photoresist is then conformally coated with a second, 3 μm layer of Parylene-C. The second layer of Parylene is etched in oxygen plasma for two minutes to improve SU8 adhesion. The surface of the wafer is planarized using approximately 60 μm thick layer of SU8. The SU8 is patterned to open the fluidic vias. Next, the Parylene beneath the SU8 vias is removed using oxygen plasma in a RIE. For control chip fabrication a layer of WL-5150 photodefinable silicone (see Section 3.6.1) is spun on to a thickness of approximately 25 μm . The silicone is then lithographically patterned and developed.

After development of the silicone, residual silicone scum is removed from the vias using SF_6/O_2 plasma in a RIE. After the silicone residue is removed, the wafer is diced and the sacrificial photoresist is released in isopropyl alcohol at 80°C . Release times for channel lengths up to 2 cm and a width of $100\ \mu\text{m}$ can take up to 14 days. Release time can be reduced by using room temperature acetone, though this is not recommended for more than three continuous days since this can reduce SU8/Parylene adhesion. Some minor delamination around the vias was observed after the long release process. This is most likely a result of the well-known volume expansion of SU8 during liquid soaking.

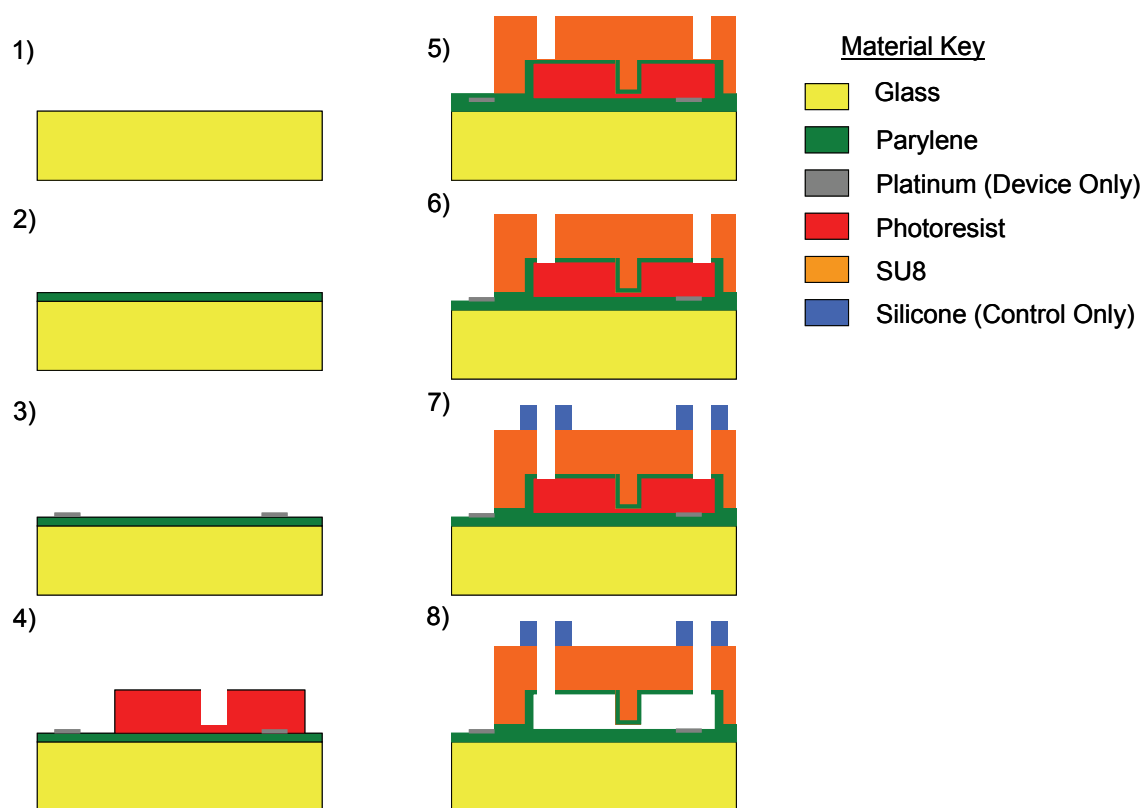


Figure 4-8. Cross-sectional diagrams of device and control chip fabrication for nHPLC. Fabrication proceeds from top-left to bottom-right. The metal layer is not typically used in the fabrication of control chips and the silicone layer is not typically used in the fabrication of device chips.

Adhesion between the two layers of Parylene is the weakest part of the device and the point of failure in high-pressure flows. The Parylene/Parylene adhesion fails at

pressures above 250 psi in the control chip but can withstand higher pressures in the device chips. Maximum device chip working pressures of up to 400 psi were attained. To improve Parylene to Parylene adhesion, an oxygen plasma etch is performed to remove any organic contaminants introduced by the sacrificial photoresist lithography. The oxygen etch is followed by a ten-second dip in buffered hydrofluoric acid to increase the hydrophobicity of the first Parylene layer. This process is thought to improve Parylene to Parylene adhesion by reducing the quantity of water trapped at the interface between the two layers.

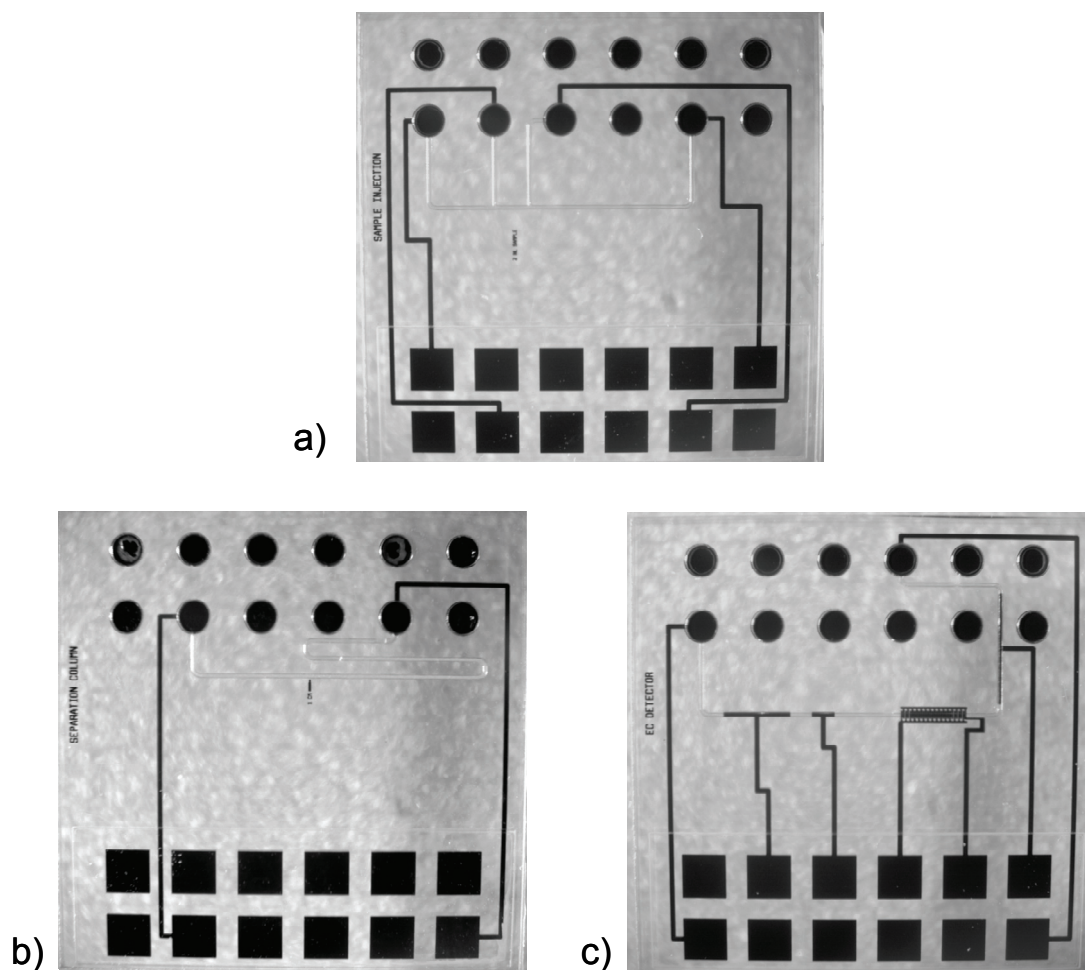


Figure 4-9. Photographs of three fabricated device chips with large vias. (a) injection device, (b) separation device, and (c) detection device. All device chips are 10 x 10 mm².

4.3.2.2 HPLC Column Packing

The separation device must be packed with 7 μm diameter PS-DVB anion exchange beads before use. To prevent beads from escaping from the column during the packing a 5 μm high filter region is defined at the end of the column structure using a partial exposure of the sacrificial photoresist (Figure 4-12). The 7 μm beads are suspended in deionized water to form a slurry using a mixing ratio of 1 mg beads per mL of water, resulting in a slurry concentration of approximately 4.5 beads/nL (Figure 4-10).

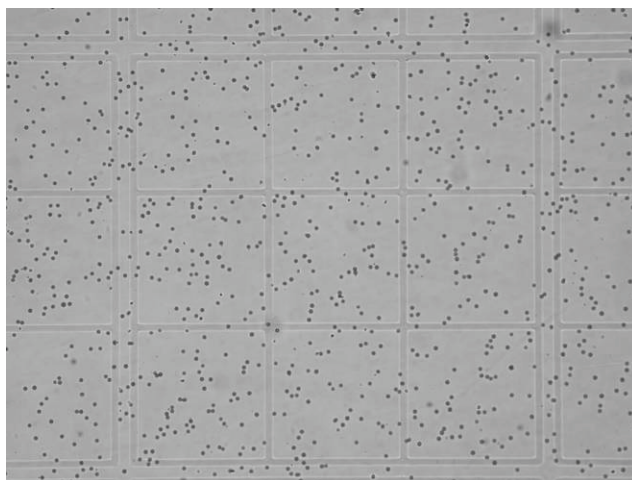


Figure 4-10. 7 μm bead slurry on cytometer. Each square contains a volume of 11.1 nL.

The slurry is then pumped through the separation column at a constant pressure of between 300 and 400 psi. The slurry is allowed to flow through the device until a 1 cm packed column length is achieved. The slurry is continuously stirred to prevent bead settling during the packing procedure. The column is then flushed with deionized water at 400 psi. Figure 4-11 shows the bead packing setup and jig.



Figure 4-11. HPLC column packing setup

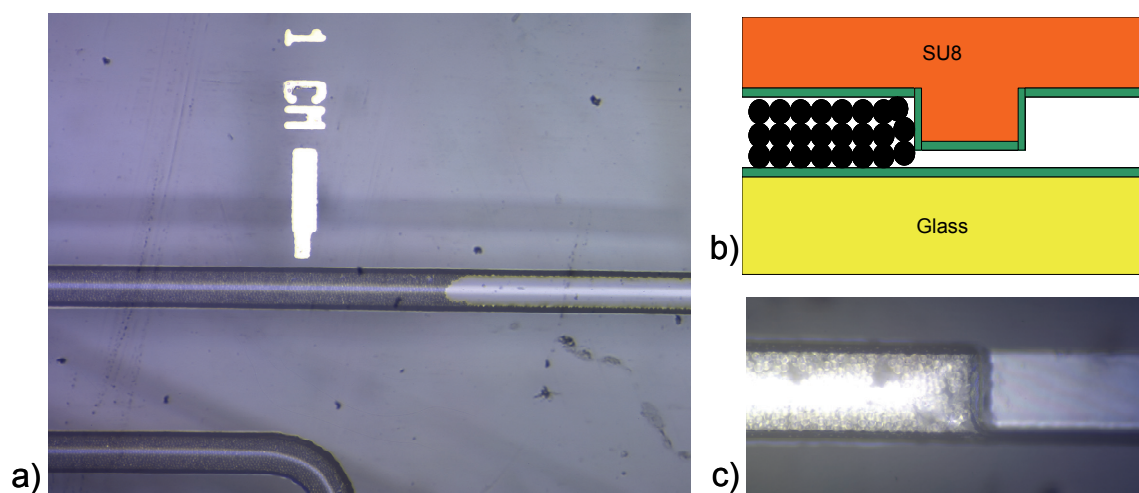


Figure 4-12. Illustrations of the HPLC separation column. (a) Fully packed separation column. (b) Cross-sectional diagram of filter region after packing. (c) Photograph of the filter region after packing

4.3.2.3 Valve-Less Injection

The injection device was designed using a π -shaped channel junction. The scheme is similar to that explored by O'Neill et al. [96], but accomplished the same functionality without the use of any external shut-off valves. The injection sequence begins with the buffer inlet pressure set to 30 psi and the sample inlet pressure set to 15 psi. Generally, the sample inlet pressure should be set such that a thin pinch flow region is formed in the junction. The injection is begun by simultaneously switching the sample inlet pressure to 30 psi and the buffer pressure to 15 psi, causing the sample solution to

fill the junction. The injection settings are held for a variable period of time to form the plug, which forms in the region downstream of the waste channel. At the end of the injection, the buffer and sample pressures are reset to their initial values, causing the back of the plug to be pinched off and reestablishing buffer flow toward the column. Figure 4-13 shows photographs of the various stages of the injection sequence. By varying the injection hold time, different plug volumes can be achieved. We were able to reliably achieve plug lengths as small as 200 μm , which corresponds to a minimum plug volume of approximately 0.5 nL.

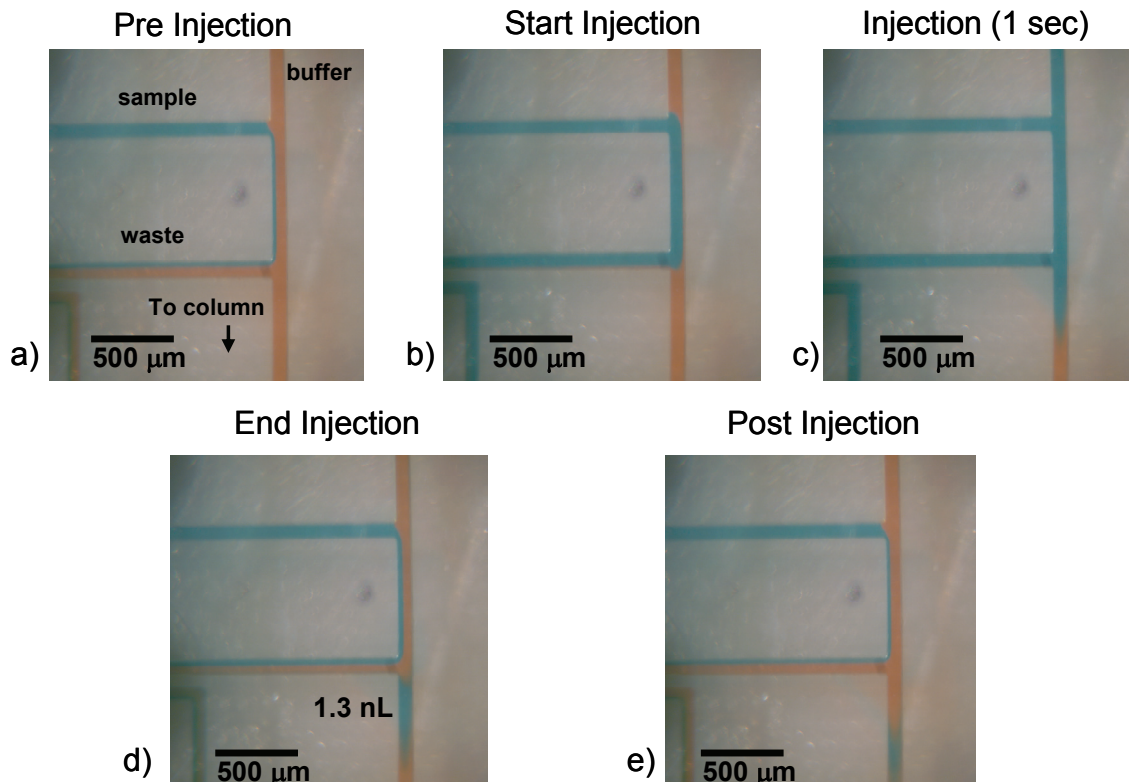


Figure 4-13. Images of valveless injection scheme. (a) Pre-injection with buffer pressure of 30 psi and sample pressure of 15 psi. (b) Start of injection with buffer pressure switching to 15 psi and sample pressure switching to 30 psi. (c) Injection settings held for 1 second. (d) End of injection with buffer pressure switching to 30 psi and sample pressure switching to 15 psi. The sample plug has been separated from the bulk sample flow. (e) Post-injection with buffer pressure of 30 psi and sample pressure of 15 psi. The plug will continue toward the separation column.

4.3.2.4 Nitrate/Nitrite Separation and Detection

Sample mixtures were prepared by dissolving reagent-grade sodium nitrate (NaNO_3) and sodium nitrite (NaNO_2) salts in deionized water and food coloring. The food coloring was used to visualize plug formation and exhibited no electrochemical activity at the detection voltage. A buffer solution of 0.1 M sodium hydroxide (NaOH) was prepared by dissolving reagent grade NaOH salt in deionized water. The system was flushed with the 0.1 M NaOH solution for at least 30 minutes to fully activate the column. This flushing procedure was repeated if a significant drop in separation efficiency was observed. The detector consisted of a $500 \times 90 \mu\text{m}^2$ thin-film platinum working electrode and a $2500 \times 90 \mu\text{m}^2$ thin-film platinum counter electrode. A cyclic voltammogram (see Section 5.2.2) of the sample solution was taken and the optimal detection voltage, the voltage producing the largest current before the onset of water hydrolysis, was found to be -0.800 V . All detections were performed at a working voltage of -0.800 V using a Princeton Applied Research Model 263A potentiostat and accompanying data acquisition software.

The sample was loaded at constant pressure until a thin flow layer was formed in the π -junction on the injection device. The injection sequence was automated through LabVIEW using two voltage-controlled gas pressure regulators. The data acquisition system on the potentiostat was initiated prior to the sample injection. The program automatically switched buffer and sample pump pressures as described in Section 4.3.2.3 to form an approximate 1.3 nL sample plug. The current between the working and counter electrodes was recorded for 150 seconds at a sampling rate of 6.66 samples/sec or for 300 seconds at a sampling rate of 3.33 samples/sec.

Several separation trials were performed using both a 100 mM sample mixture and 1 mM sample mixture. A typical chromatogram is shown in Figure 4-14 along with the peak analysis. A summary of several trials is given in Table 4-1. The peak analysis was performed using equations (4.3-8) to (4.3-10). Each peak was fit to a Gaussian distribution as described in equation (4.3-7).

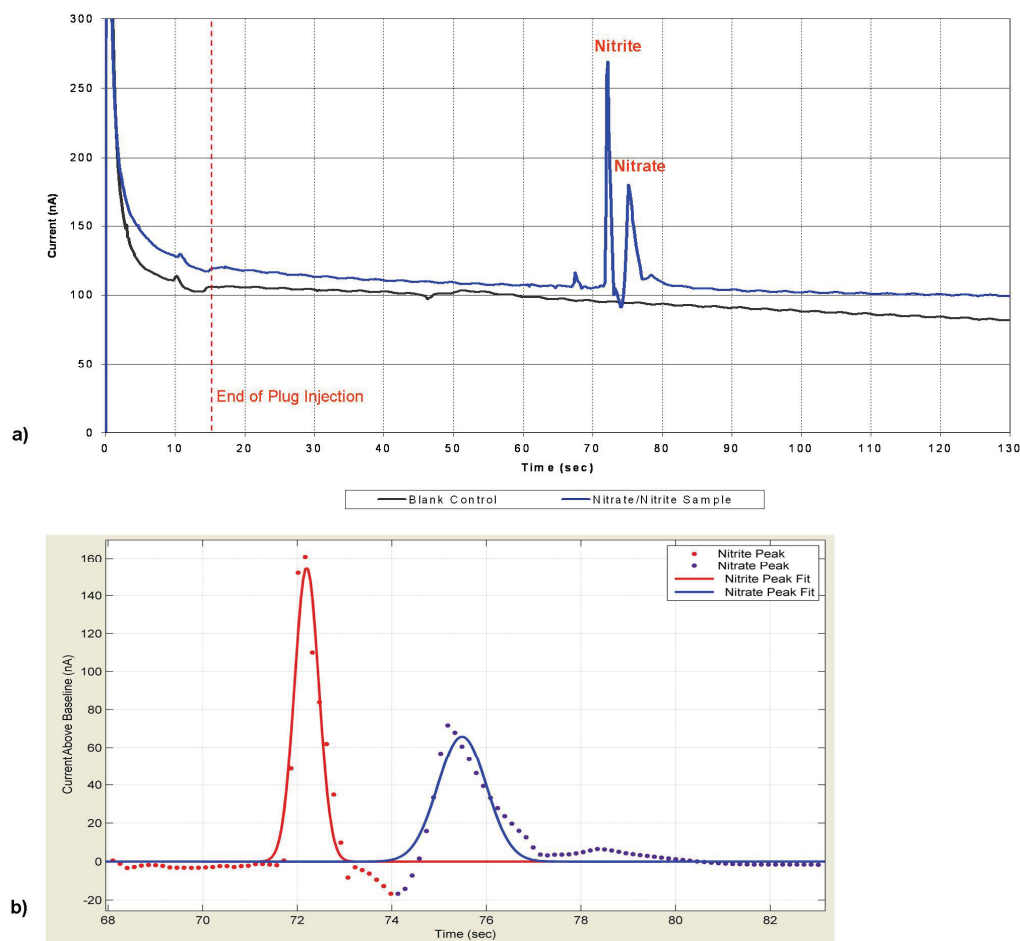


Figure 4-14. Nitrate/nitrite separation results and analysis. (a) Typical separation chromatogram showing nitrate and nitrite separation. The chromatogram corresponds to Trial 2. The end of the plug injection sequence, t_0 , is marked. The blank control data shows the detector response for a sample plug containing only food coloring and no nitrate or nitrite. (b) Peak analysis done using MatLab by fitting Gaussian profiles to the individual peaks. The baseline current is 108.1 nA and t_0 is 17.1 seconds. Nitrite peak fit parameters are $a = 154.9$, $\mu = 72.2$, and $\sigma = 0.2538$ resulting in an $R^2 = 0.9304$. Nitrate peak fit parameters are $a = 65.78$, $\mu = 75.48$, $\sigma = 0.5108$ resulting in an $R^2 = 0.8795$.

Table 4-1: Nitrite/Nitrate Separation Analysis

Trial	Analyte	C (mM)	I _p (nA)	R _t (sec)	σ ² (sec ²)	A _s	N	R _s
First	Nitrite	100	162.01	80.80	0.079	2.171	82,537	2.725
	Nitrate	100	54.11	85.80	0.405	10.524	18,195	
Second	Nitrite	100	160.87	55.10	0.064	1.793	47,143	2.145
	Nitrate	100	71.67	58.38	0.261	7.074	13,063	
Third	Nitrite	100	170.57	84.40	0.037	2.470	193,045	2.306
	Nitrate	100	57.57	87.70	0.274	11.212	28,081	
Fourth	Nitrite	1	62.16	98.59	0.343	Blend*	28,363	0.560
	Nitrate	1	59.86	101.49	4.013	Blend*	2,567	

*Indicates that the peaks blend with one another before reaching the 5σ width

4.3.3 Summary

The separation performance of the modular system compares very favorably to most commercial HPLC systems. Most modern macro HPLC columns between 1 and 15 cm in length will report plate counts in the range of 10,000 – 25,000 [97-100]. This system achieved an average nitrite plate count of 87,772 and an average nitrate plate count of 15,477. As in all HPLC systems any transit time from the sample injector to the column and from the column to the detector, referred to as auxiliary transit time, will allow increased band broadening. Due to the system's on-chip design and high flow rate, however, the total auxiliary transit time is relatively small allowing for the high-efficiency separation. In one case, the separation efficiency approached that normally achieved in capillary electrophoresis systems, 10⁵ to 10⁶ theoretical plates, which have very little or no auxiliary transit time [101]. This level of performance was achieved with almost no optimization of buffer composition or flow parameters.

One of the drawbacks to the current experimental setup is the inability to monitor the buffer flow rate. A buffer flow rate between 150 nL/min and 250 nL/min was estimated from images taken during the injection sequence but accurate *in situ* measurement was not possible. Of course, due to the nature of the modular design

addition of a flow sensor, most likely after the detector, could be accomplished in the future with relative ease. Another drawback is the system reliance on a constant pressure source maintained by the two voltage-controlled gas regulators which are operated near the low end of their range. This resulted in significant drift in the pump pressures of up to ± 2 psi. The drift in the pressure source, and accompanying change in flow rate, accounts for the variation in retention times observed in the various trials.

4.4 Conclusions

The presented modular microfluidic technology offers great flexibility in application. The modular nHPLC system clearly demonstrates that modular microfluidic systems, when properly designed, can maintain the high performance offered by device size reduction and on-chip fabrication. The introduction of a robust, easy-to-use, fully integrated interconnect technology makes the possibility of widespread interchangeable microfluidic devices and complex microfluidic systems feasible. Future works include characterization and optimization of the detector for use in the investigation of single-cell metabolic activities in microfluidic systems. Primary application of the modular approach using MEMS O-rings lies in either commercial microsystems that will benefit from routine but non-destructive maintenance or prototype laboratory systems requiring frequent but functionally isolated design changes. In commercial applications jig design will be extremely important because overall ease-of-use is strongly influenced by the packaging.

As the complexity of microfluidic systems increases, the need to independently design and fabricate system components will become greater for many applications. Modular microfluidics will be necessary to reduce system research and development

time, improve system flexibility, and allow for system maintenance. By separating system component fabrication, individual parts can be more readily optimized and characterized. These advantages of modular microfluidics outweigh the minimal increase in cost and complexity associated with the fabrication of an interconnect chip.

5 WORKING ELECTRODE MATERIALS FOR INTEGRATED ELECTROCHEMICAL DETECTORS

5.1 Introduction

Electrochemical detectors (ECDs) are a key component in high performance liquid chromatography systems. On-chip HPLC, or nano HPLC (nHPLC), systems use relatively small sample volumes compared to conventional HPLC, while offering comparable separation performance [38]. The small fluid volumes, however, contain insufficient analytes for UV absorption detection. ECDs offer a viable alternative for electrochemically active analytes with the advantage of enhanced selectivity in detection. This detection method is ideal for use in nHPLC, systems since it responds to analyte concentration without regard for the total amount of analyte. ECD have the additional advantage of being easier to fabricate using MEMS technology relative to other detection schemes.

ECDs with detection limits as low as 0.1 pM have been reported under special conditions but practical limits over a wide variety of analytes tend to be above 0.1 μ M [95, 102]. It has been reported that nanoarrays of vertical carbon nanotubes can achieve detection limits on the order of 1 nM [103]. The development of ultra-low detection limit ECDs coupled with a nHPLC will facilitate selective trace analyte measurement.

Electrochemical detector performance depends on many factors. Most factors such as buffer composition, pH, and operating temperature also affect separation performance, hence there is limited room over which to optimize these elements. One factor that plays a major role in detector performance is the composition of the working electrode. Working electrode composition is not limited to just the working electrode material selection, but also any pretreatment or activation procedures performed to improve sensitivity, responsivity, or selectivity. Typical working electrode materials include platinum (an inert metal), mercury (an atomically smooth liquid electrode), and carbon.

This chapter will investigate several new carbon-based materials for use as ECD working electrode materials. The first material is a thin-film carbon formed from a Parylene-C seed layer. The carbon can conformally coat high surface area structures allowing for considerable increases in the effective surface area of the electrode. The second material is an embedded vertical carbon nanotube array which has individual array elements with diameters of only 100 nm and array densities of 1 element per square micron. The chapter will begin with a short introduction to relevant electrochemical theory and then discuss thin-film carbon electrodes followed by CNT nanoarray electrode fabrication and electrochemical characterization.

5.2 Electrochemical Characterization Techniques

Due to the broad application of electrochemistry to analyte detection, it is difficult to determine the “best” working electrode material. In fact, experience has shown that many materials are suitable for electrochemical detectors, but that most share several common attributes. Good electrode materials are chemically inert and do not degrade as

they are used, do not form an oxide layer (or form one that can be easily removed through polishing or other pretreatment), and generally behave according to electrochemical theory. There are no standardized tests for determining the usefulness of a material as an electrochemical detector. However, several common tests are used in the literature. All of the tests attempt to confirm that the electrode material does not affect the behavior of an analyte that is known to behave according to predictive theories. Several common test analytes are $\text{Fe}(\text{CN})_6^{3-/4-}$, $\text{Ru}(\text{NH}_3)_6^{2+/3+}$, $\text{IrCl}_6^{2-/3-}$, $\text{Co}(\text{phen})_3^{2+/3+}$, and $\text{Co}(\text{en})_3^{2+/3+}$ with $\text{Fe}(\text{CN})_6^{3-/4-}$ and $\text{Ru}(\text{NH}_3)_6^{2+/3+}$ the most common [104].

An electrochemical system consists of two species in solution. One species will be oxidized by losing an electron to an electrode, called the anode, while the second species will be reduced at a different electrode, called the cathode, by receiving an electron. The oxidation and reduction reactions must occur simultaneously with an equivalent charge transfer in each, hence the entire reaction is called a reduction/oxidation or redox reaction. Most redox reactions do not occur spontaneously; rather, they typically require some applied energy in the form of an electric potential. A third electrode, called the reference electrode, is often used as a stable baseline to which the applied potential is added. The applied potential reduces the electron transfer barrier between the electrode and the analyte in solution allowing for charge transfer (Figure 5-1). The rate of charge transfer is typically limited, not by the speed of electron transfer, but instead by the availability of analyte at the electrode surface. In stationary solutions the only means of analyte transport to and from the electrode surface is diffusion (Figure 5-1). Moving solutions are more difficult to understand analytically and are therefore not typically used

when characterizing electrode materials. Hence, most electrode material studies are carried out in the diffusion-limited regime.

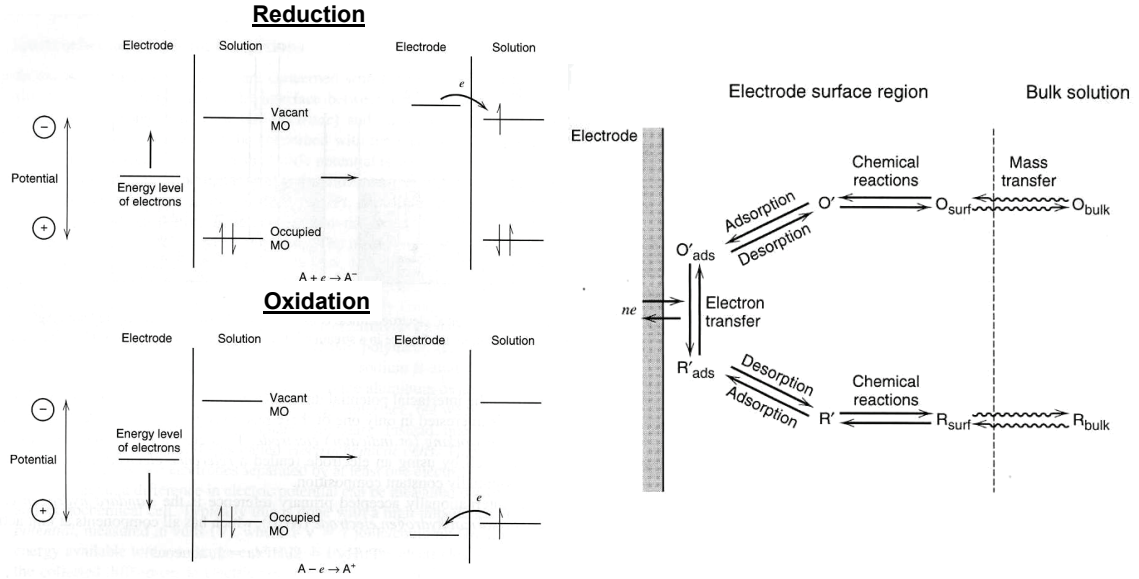


Figure 5-1. Diagram of electron charge transfer at an electrode and mass transport to and from the electrode surface. Images taken from [95].

In the diffusion-limited case it is relatively straight forward to predict the current behavior of a system whose working potential is set at a value large enough to cause oxidation of the analyte (a similar derivation can be done if analyte reduction is of interest). The mass transport mechanism is described by Fick's first and second laws:

$$J_o = -D_o \nabla C_o, \quad (5.2-1)$$

$$\frac{\partial C_o}{\partial t} = D_o \nabla^2 C_o, \quad (5.2-2)$$

where J is the current density, D is the diffusion coefficient, C is concentration profile, and t is time. The current is then given by:

$$i = -nFAJ_o = nFAD_o \left[\nabla C_o \right]_{\text{electrode_boundary}}, \quad (5.2-3)$$

where n is the number of electrons per transfer event, F is Faraday's constant (96485.3 C), and A is the effective electrode surface area. The diffusion coefficient of several common analytes in water is given in Table 5-1.

Table 5-1: Diffusion Coefficients in Water [105]

Solute	T (°C)	D ($\times 10^{-5}$ cm ² /s)	Solute	T (°C)	D ($\times 10^{-5}$ cm ² /s)
Acetone	25	1.28	HCO ₃ ⁻	25	1.185
Acetonitrile	15	1.26	Isopropyl alcohol	15	0.87
Cl ⁻	25	2.032	K ⁺	25	1.957
Ethanol	25	1.24	Na ⁺	25	1.334
F ⁻	25	1.475	NH ₄ ⁺	25	1.957
Glucose	25	0.67	NO ₂ ⁻	25	1.912
Glycine	25	1.05	NO ₃ ⁻	25	1.912
H ⁺	25	9.311	OH ⁻	25	5.273

If the electrode is assumed to be an infinitely long, one-dimensional line and the concentration of analyte far from the electrode is C^* , then the solution to equation (5.2-3) is known as the Cottrell equation:

$$i(t) = \frac{nFAC^* \sqrt{D_0}}{\sqrt{t\pi}}. \quad (5.2-4)$$

For electrode geometries other than an infinite line the current behavior is described as the sum of the Cottrell equation and some other steady or quasi-steady state term of the following form:

$$i_{total} = i_{Cottrell} + i_{(q)ss} = i_{Cottrell} + nFAC^* m, \quad (5.2-5)$$

where m is the geometry dependent term [95]. Table 5-2 gives the value of m for several common electrode geometries in microfluidics where r_0 is the radius of the electrode and w is the width.

Table 5-2. Table of m Factors for Typical Microelectrode Geometries [95]

Band	Cylinder	Disk	Hemisphere	Sphere
$\frac{2\pi D_o}{w \ln(64D_o t/w^2)}$	$\frac{2D_o}{r_0 \ln(4D_o t/r_0^2)}$	$\frac{4D_o}{\pi r_0}$	$\frac{D_o}{r_0}$	$\frac{D_o}{r_0}$

5.2.1 Double Layer Capacitance

When a charged electrode is in solution, the ions in the solution rearrange in the vicinity of the electrode surface to screen the charge. A negatively charged electrode will attract positively charged ions to its surface and repel negatively charged ions. The attracted ions will encounter a layer of adsorbed solvent molecules and other adsorbed ions on the electrode surface. This layer of adsorbed molecules forms the inner Helmholtz plane. The attracted ions will form a second layer called the outer Helmholtz plane, or diffuse layer. Since both of these layers contain charged molecules the combined structure is called the electrical double layer (Figure 5-2a).

The electrical double layer behaves like a standard capacitor in electronics by storing and releasing charge in the diffuse layer as the potential changes. Because of this electrode, interactions are often modeled using circuit theory elements (Figure 5-2b). The double layer capacitance³, C_d , is mainly a function of the electrode material and surface condition. Since the double layer capacitance is a strong function of electrode material, it is usually estimated during electrode characterization. The double layer capacitance is important to electrochemical detectors because it, along with the uncompensated resistance, determines how quickly the detector can react to a change in

³ The double layer capacitance is usually reported as a capacitance per unit surface area and hence has units of F/m². Some authors prefer to report double layer capacitance without normalizing to the electrode surface area. Care must be taken to determine the units of C_d from the context.

input. The double layer capacitance along with other electrochemical behaviors can be investigated using a technique known as cyclic voltammetry.

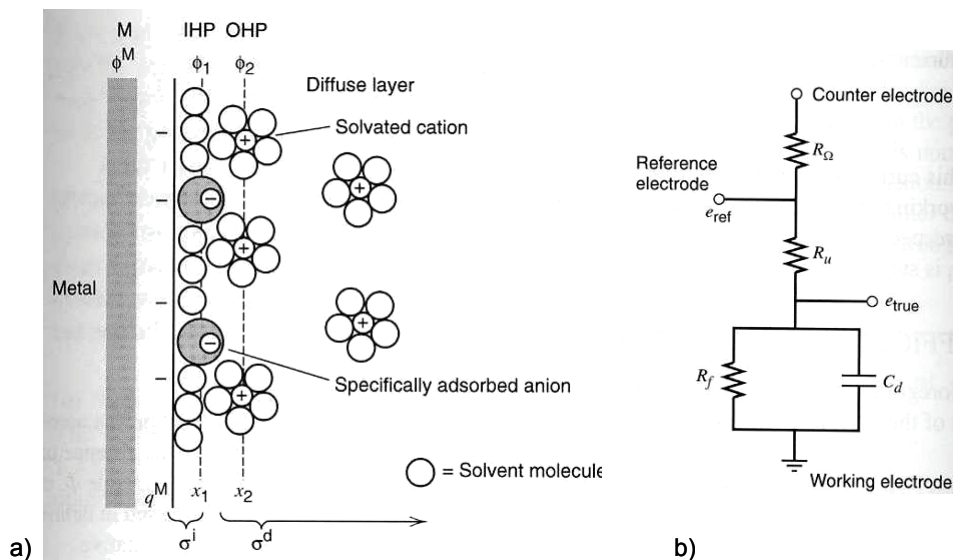


Figure 5-2. (a) Illustration of electrical double layer. (b) Example of a circuit model of an electrode/solution interface. Images taken from [95].

5.2.2 Cyclic Voltammetry

Cyclic voltammetry is a classical electrochemical technique that can be used to investigate either the electrochemical behavior of an unknown analyte or the behavior of an electrode material using a known analyte. The basis of cyclic voltammetry is the use of a time-varying potential that cycles back to its initial point and changes at a constant rate (Figure 5-3). The constant rate of change of potential is known as the scan rate, ν , and is typically between 10 mV/sec and 1000 mV/sec, with the most common values chosen being either 50 mV/sec or 100 mV/sec for electrode characterization. The shape of the voltammogram can be described mathematically. The electrode potential and analyte concentration profile are given by [95] :

$$E(t) = E_i - \nu t \quad (5.2-6)$$

and

$$C_o(0, t) = C_o^* - [nFA(\pi D_o)^{1/2}]^{-1} \int_0^t i(\tau)(t - \tau)^{1/2} d\tau, \quad (5.2-7)$$

$$\int_0^t i(\tau)(t - \tau)^{-1/2} d\tau = \frac{nFA(\pi D_o)^{1/2} C_o^*}{\sqrt{\frac{D_o}{D_R}} \exp[(nF / RT)(E_i - E^{0'} - \nu t)] + 1}. \quad (5.2-8)$$

Now letting

$$\sigma = (nF / RT)\nu, \quad (5.2-9)$$

The total current can be expressed as:

$$i_{total} = i_c + i(t) = AC_d\nu + nFAC_o^*(\pi D_o\sigma)^{1/2} \chi(\sigma t), \quad (5.2-10)$$

where $\chi(\sigma t)$ is derived from equation (5.2-7) and must be solved for numerically at any given t [95]. Numerical evaluation of equation (5.2-10) shows that a peak current exists that is given by [95]:

$$i_p = \max i - i_c = (2.69 * 10^5) n^{3/2} A D^{1/2} C^* \nu^{1/2}. \quad (5.2-11)$$

The important things to note about equation (5.2-11) is that it predicts that the maximum current in the voltammogram minus the capacitive current, called the peak current, will scale linearly with electrode surface area and bulk analyte concentration, and scale proportionally with the square root of the scan rate. In practice, i_c is not always independent of potential. In any case, peak current should always be measured from the i_c baseline, as shown in Figure 5-3.

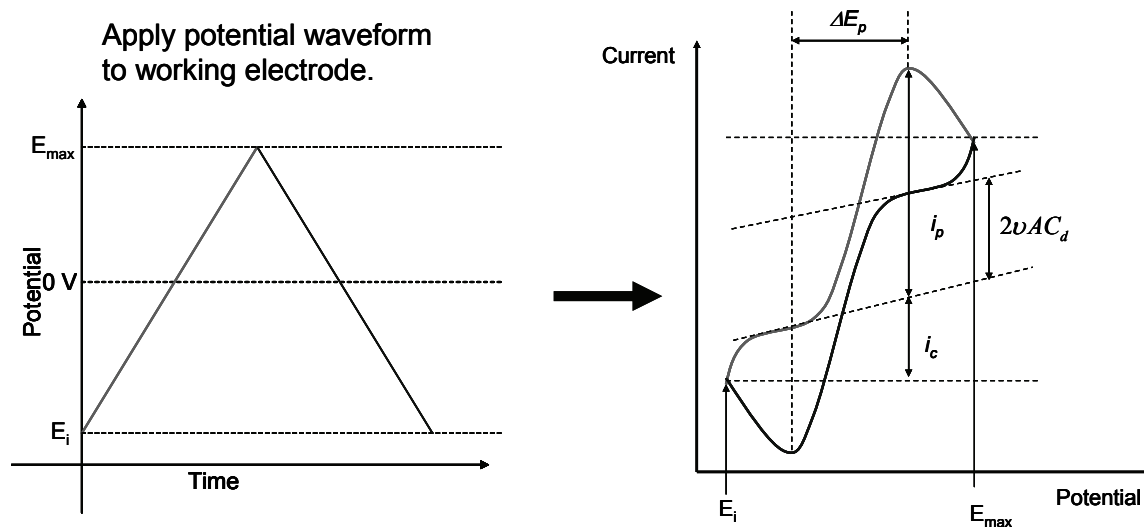


Figure 5-3. Diagram of typical cyclic voltammetry measurement

Since in cyclic voltammetry there is both a forward sweep and a backward sweep, there are two peaks for a reversible reaction, one for each sweep. If an electrochemical reaction is fully reversible and the sweep rate is sufficient that diffusion effects are minimized, the forward and backward sweeps should be identical except for changes in sign. The potential difference between the two peaks can be predicted using electrochemical theory [95]:

$$\Delta E_p = E_p^c - E_p^a = \frac{2.3RT}{nF} \quad (5.2-12)$$

At 25°C for a single electron transfer reaction ($n = 1$), equation (5.2-12) predicts an ideal peak separation of 56.5 mV. Increases in peak separation beyond the ideal value indicate surface contamination problems. Common surface contaminants are adsorbed species, insoluble products of the redox reaction, or an oxide layer. Typically, electrode surfaces are pretreated and then tested using a well known analyte to verify they can achieve close to the ideal peak separation. This procedure is critical in characterizing new electrode materials.

5.3 Thin-Film Carbon as a MEMS Material

Carbon is often the material of choice for electrochemical sensor electrodes because of its high chemical and mechanical stability, relatively high resistance to oxide layer formation, wide potential window, and low cost. Manufacturing of carbon into suitable electrodes is often based on either a pyrolysis technique, such as the making of carbon fibers from polyacrylonitrile fibers, or from a carbon paste containing carbon by-products of petroleum or coal burning [102]. While sufficient for the investigation of electrochemical properties of solutions, carbon electrodes made using these methods are difficult to integrate into many microdevices. Of particular interest in the MEMS community is the ability to fabricate thin-film carbon (TFC) microelectrodes for integration into a variety of chemical and biochemical sensors. Carbon has recently been used in MEMS devices as diverse as an uncooled bolometer [106], a 3D microbattery [107], and a nanofluidic flowmeter [108]. For electrochemical MEMS sensors, carbon films must be compatible with photolithography processing, have good adhesion to the substrate, and still maintain all the electrochemical benefits of carbon.

The most common methods of constructing surface-machined carbon microelectrodes are screen-printing using a carbon paste and sputtering. Recently pyrolysis of photoresists has been explored as another alternative for carbon deposition [107, 109, 110]. Screen printing lacks the ability to make microelectrodes with features smaller than 200 μm or to provide a conformal carbon coating. Pyrolyzed photoresist can provide atomically smooth carbon coatings, but it is not conformal and can limit processing options prior to pyrolysis. Sputtering allows for both small feature sizes and mostly conformal coating but can be limited by shadowing effects and very high aspect

ratios. Another alternative is to use Parylene-C as the carbon source material for microelectrodes [106, 111, 112]. Parylene is conformally deposited at room temperature even over very high aspect ratios, is not limited by shadowing, can be patterned into small features before or after pyrolysis using an oxygen plasma, and shows good adhesion to most materials in both its deposited and pyrolyzed forms. Pyrolyzed Parylene was first used by Hui et al. [113] as a fast-etching, conformal, sacrificial layer in molded polysilicon processes.

5.3.1 TFC from Pyrolyzed Parylene-C

To develop a better understanding of the pyrolysis process for Parylene-C, several tests were performed. A free-standing film of Parylene-C (15.8mg) was examined by simultaneous thermal analysis, which provides thermogravimetric analysis (TGA) and differential scanning calorimetry (DSC). The sample was heated to 1500°C with a heating rate of 5°C/min in flowing Ar (100mL/min). The inert Ar atmosphere was necessary to prevent burning of the carbon. As seen in Figure 5-4, the material undergoes an endothermic phase transition, presumably melting, at 296°C. An exothermic event peaks near 480°C and is accompanied by a weight loss of 66%. The exothermic event at 480°C is believed to be the Parylene-to-carbon transition. Total weight loss to 1500°C is 70.1%.

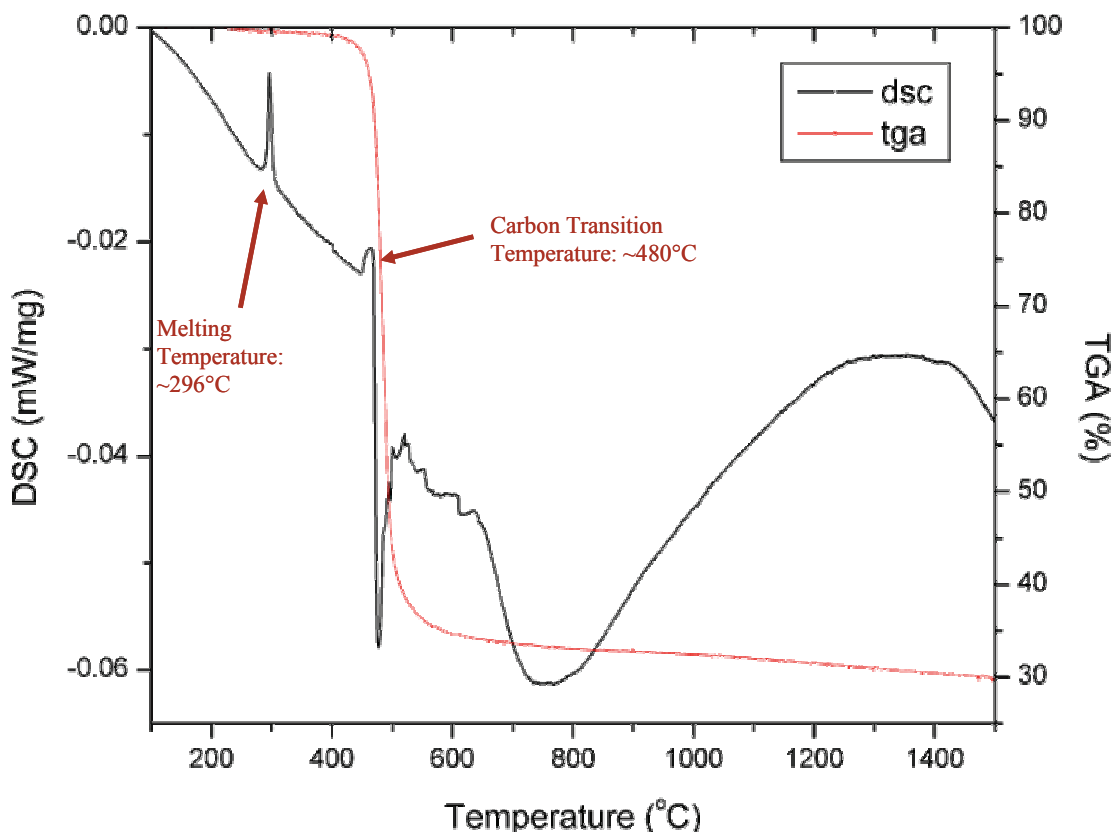


Figure 5-4. Simultaneous thermal analysis data for a free-standing, 15.8 mg film of Parylene-C (heating rate = 5°C/min, in flowing Ar at 100mL/min)

MicroRaman analysis was conducted on both loose film and attached Parylene samples (Figure 5-5). Parylene carbonized at 900°C on Si shows broad and poorly defined G and D1 peaks, whereas carbonization at 1550°C in flowing Ar resulted in narrow and well-defined peaks, indicative of glassy carbon. The band near 1580cm⁻¹ is known as the graphite band (G band) and corresponds to the in-plane vibration of C atoms in graphite structure [114, 115]. For perfect single-crystal graphite, it would be the only band observed. The presence of the so-called defect band (D1) around 1350cm⁻¹ indicates that a finite particle size is associated with carbonized Parylene. The D1 band is broader for poorly ordered carbons, and narrows as increased heat treatment results in increased order, as can be seen in Figure 5-5.

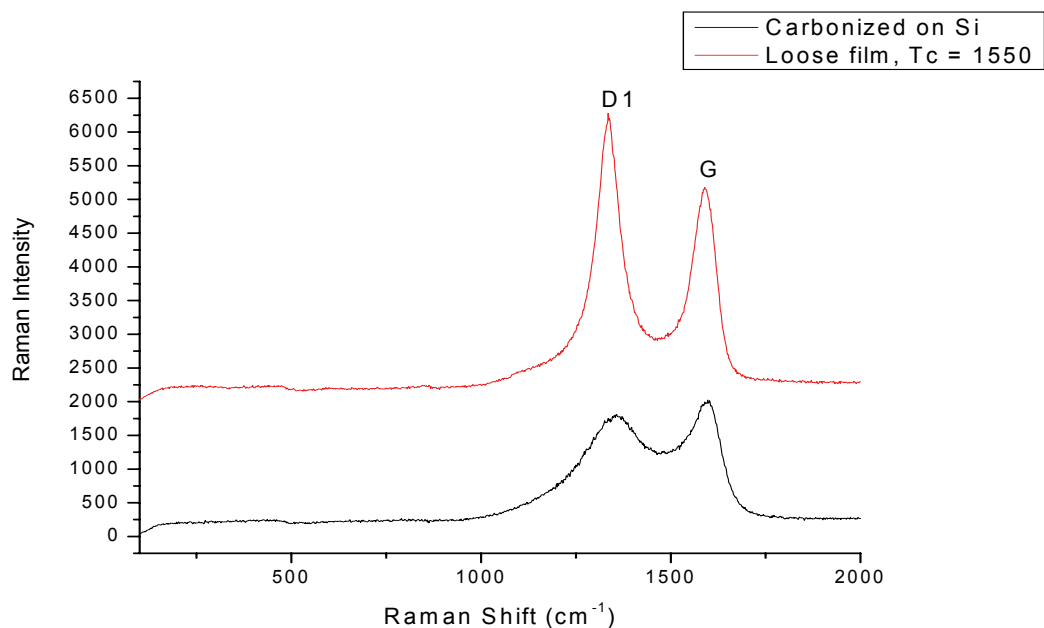


Figure 5-5. MicroRaman data for Parylene C. Parylene C was carbonized in furnace at 1550°C (top - heating rate = 5°C/min, held at temperature for 5 min, flowing Ar @ 100mL/min) and Parylene C carbonized on Si (heating rate = 10°C/min, held at 900°C for 1 hr, flowing N₂ at 100 mL/min) showing clear glassy carbon peaks, labeled D1 and G, according to [114, 115].

Resistivity of pyrolyzed Parylene was measured for pyrolysis temperatures between 600°C and 900°C (Figure 5-6) [116]. The effects of heating rates were also investigated. As shown in Figure 5-6, the resistivity of the thin-film carbon can be changed over 12 orders of magnitude. The lowest resistivity was achieved at the highest pyrolysis temperature. The changes in resistivity are consistent with the MicroRaman data which shows the development of a more ordered and graphite-like structure at high pyrolysis temperatures. For electrochemical detectors, the most graphitic, therefore lowest resistivity, carbon is desired.

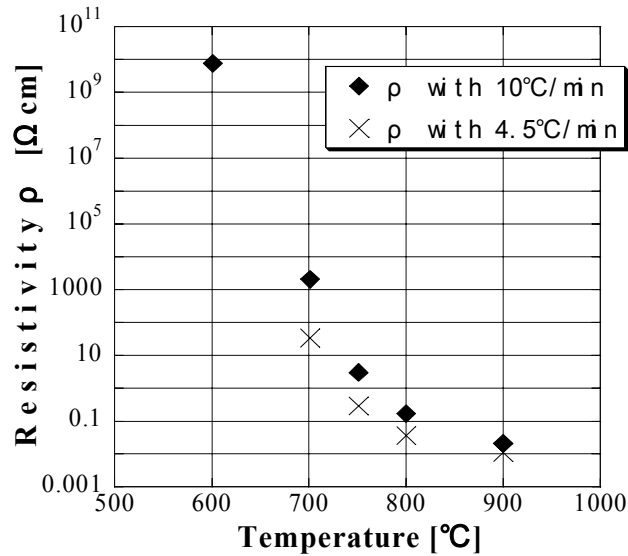


Figure 5-6. Resistivity as a function of pyrolysis temperature and heating rate. Note resistivity is adjustable over 12 orders of magnitude. Figure from [116].

5.3.2 Pyrolyzed Parylene Electrodes

Of particular interest in the MEMS community is the ability to fabricate thin-film carbon microelectrodes for integration into a variety of chemical and biochemical sensors. The carbon films must be compatible with standard MEMS processing, most importantly photolithography, and still maintain all the electrochemical benefits of carbon. Pyrolyzed Parylene-C not only meets these requirements but it is also conformal over high aspect ratio structures (Figure 5-7).

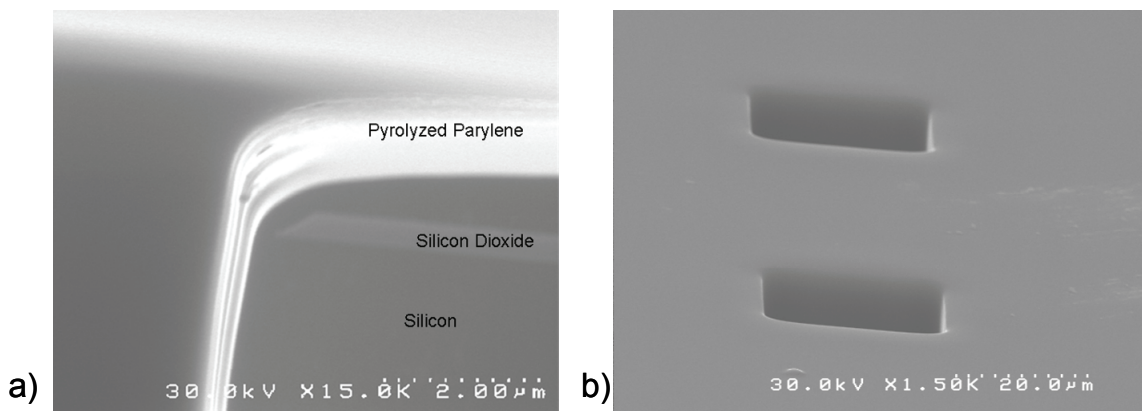


Figure 5-7. Three-dimensional electrodes using pyrolyzed Parylene. (a) Cross-section view of silicon well coated in pyrolyzed Parylene. Note the conformal nature of the coating. Oxide growth done prior to well etch. (b) Top side view of silicon wells coated in pyrolyzed Parylene

The increase, or gain, in geometric surface area obtained by using square posts conformally coated in carbon as an electrode structure can be estimated as

$$G_{square} = \frac{A_{actual}}{A_{projected}} = 1 + \frac{4dw}{(s+w)^2}, \quad (5.2-13)$$

where d is the depth of the silicon posts, s is the closest edge-to-edge separation, and w is the width of the posts. For square-packed cylindrical posts of radius, r ,

$$G_{cyl-square} = 1 + \frac{2\pi rd}{(s+2r)^2}, \quad (5.2-14)$$

and for hexagonally-packed cylindrical posts of radius, r ,

$$G_{cyl-hex} = 1 + \frac{4\pi rd}{\sqrt{3}(s+2r)^2}. \quad (5.2-15)$$

Finally, for a hexagonally-packed, hexagonal post, of side length, w , the gain is:

$$G_{hex-hex} = 1 + \frac{16wd}{\sqrt{3}(2w+s)^2}. \quad (5.2-16)$$

Fabrication constraints require $s \geq 25 \mu\text{m}$, w or $2r \geq 3 \mu\text{m}$, and $d \leq 250 \mu\text{m}$ for $10 \mu\text{m}$ Parylene coatings. For $3 \mu\text{m}$ Parylene depositions, s can be reduced to $9 \mu\text{m}$. Parylene coatings below $3 \mu\text{m}$ could produce films whose mechanical strength is insufficient. The geometric surface area is maximized when the $s = w = 2r$, w is minimized, and d is maximized subject to all constraints. Table 5-3 summarizes the expected gains for the four different post geometries and for the two different Parylene coating thicknesses. Calculations show that hexagonally-packed hexagonal posts will produce the greatest gain in surface area, approximately 29.51.

Table 5-3. Gain in Surface Area Due to 3-D Electrode Structure

Geometry	10 μm Parylene Gain	3 μm Parylene Gain
Square	11	28.78
Cylindrical-Square Pack	8.85	22.82
Cylindrical-Hex Pack	10.07	26.19
Hex-Hex Pack	11.26	29.51

5.3.2.1 TFC Electrode Fabrication

Thin-film pyrolyzed Parylene-C electrodes were fabricated using room temperature polymer vapor deposition onto a Si/SiO₂ substrate. The electrodes were pyrolyzed in a nitrogen atmosphere then patterned using O₂ plasma. Metal contacts were deposited and the 900°C electrodes were then isolated with a second Parylene layer. The isolation Parylene layer was then etched using O₂ plasma to form either single electrodes or an array of electrodes (Figure 5-9). The fabrication process is diagrammed in Figure 5-8.

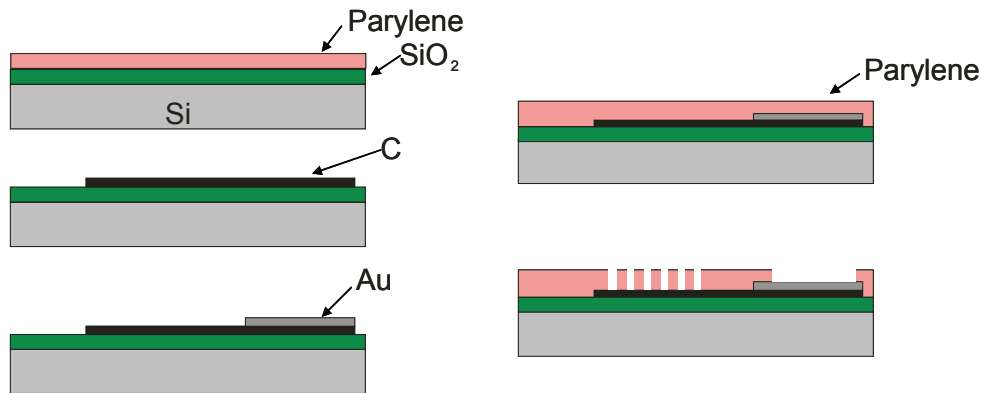


Figure 5-8. TFC electrode fabrication process

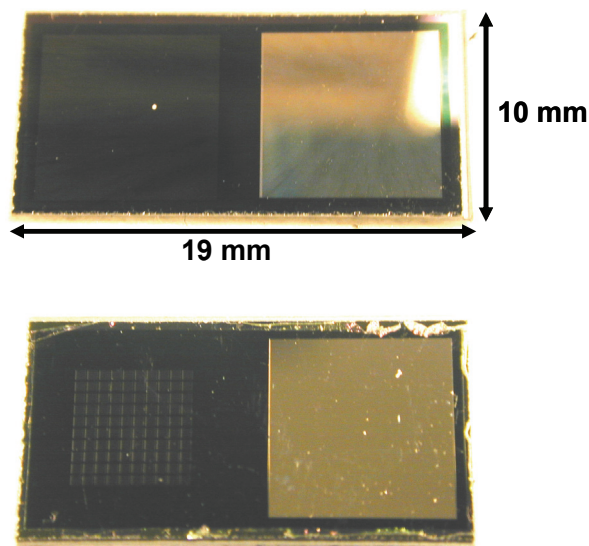


Figure 5-9. Fabricated TFC electrodes. (a) Single 58.06 mm² opening. (b) 10 x 10 array of 0.16 mm² electrodes

5.3.2.2 TFC Electrode Characterization

A simple electrochemical characterization was performed to show that the thin-film carbon has potential as a working electrode material. Figure 5-10 shows cyclic voltammograms of 5 mM $\text{Fe}(\text{CN})_6^{3-/4-}$ in 0.1 M KCl for a pyrolyzed Parylene electrode, as well as a scan using a Pt electrode for comparison. The Parylene was pyrolyzed at 900°C in an N_2 atmosphere. The measured differences in anodic and cathodic peak potentials are 144 mV and 216 mV for the Pt and TFC electrodes, respectively. No pretreatment was performed on the TFC electrode. The Pt electrode was polished by hand using alumina slurry, rinsed thoroughly with deionized water, and dried prior to use. Improvements in electrode kinetics, evident by a reduction in peak-to-peak separation, were observed as carbonization temperature and film thickness are increased (data not shown).

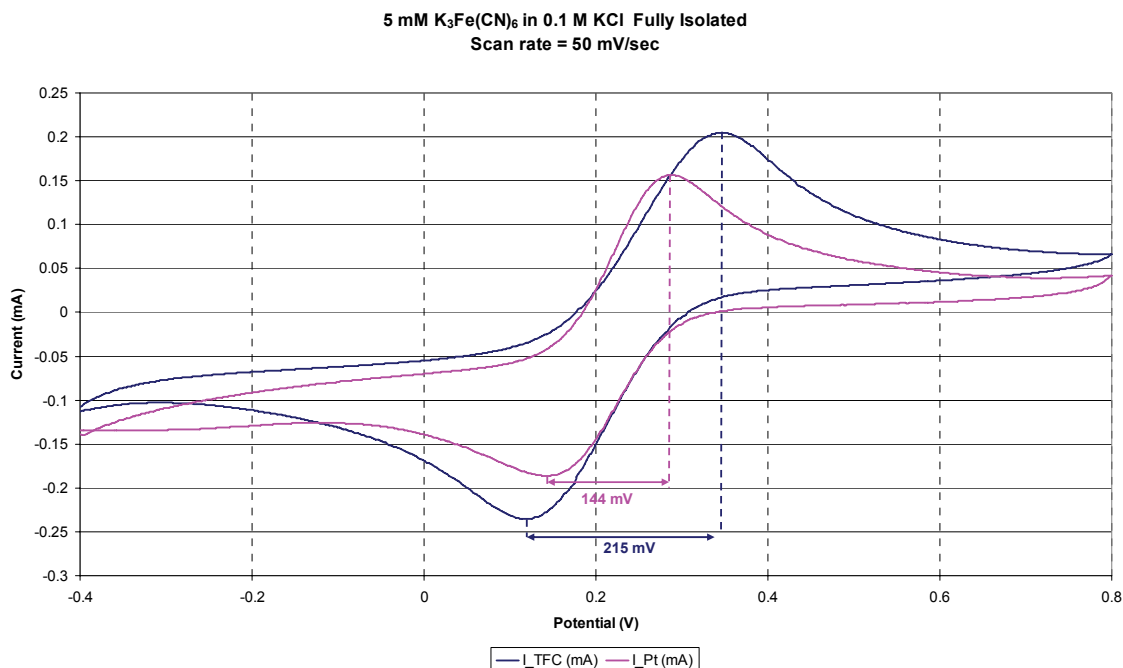


Figure 5-10. Cyclic voltammograms of 5.0 mM hexacyanoferrate in 0.1 M KCl using platinum and pyrolyzed Parylene electrodes. The scan rate is 50 mV/sec. The Parylene was pyrolyzed at 900°C.

The thin-film carbon was prone to adhesion failure to the oxide substrate after several minutes of soaking in the electrolyte solution. The 2nd layer of Parylene deposited for isolation was helpful in minimizing detachment of the film from the substrate. Electrochemical performance of the TFC electrodes was not extensively characterized. Preliminary results show that the TFC can be used as an electrode material with performance slightly worse than platinum wire.

5.4 Carbon Nanotubes Nanoarrays

Carbon nanotubes (CNT) are allotropes of carbon. The nanotube structure can be described as a one atom thick sheet of carbon rolled to form a tube (Figure 5-11). Carbon nanotubes come in two main varieties: 1) single-walled (SWCNT) and 2) multi walled (MWCNT). The discovery of MWCNT is traditionally attributed to Sumio Iijima [117] in 1991, but there exists several earlier publications of similar items [118]. SWCNT were

discovered simultaneously by Iijima and Ichihashi [119] and Bethune et al. [120] in 1993. In 2002, Li et al. [121, 122] developed embedded vertical CNT nanoarrays that could be used as electrochemical detectors.

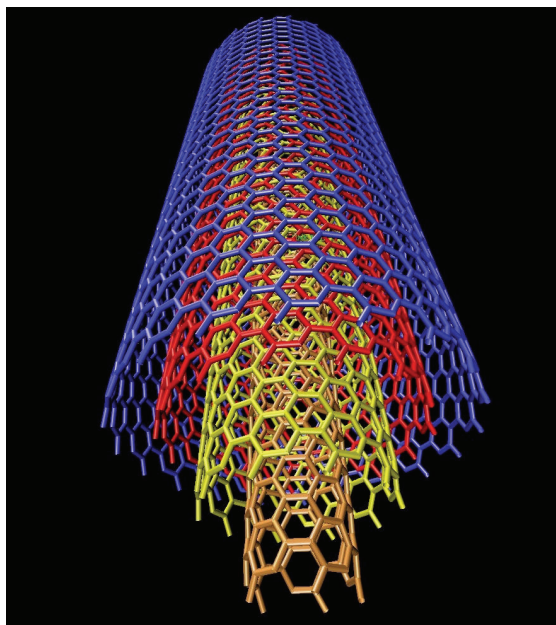


Figure 5-11. Illustration of a multi-walled carbon nanotube. Image taken from [123].

Integration of carbon nanotubes (CNT) with microfluidic HPLC columns presents several major fabrication challenges. For most CNT applications, CNT are grown and put into a liquid suspension and later dispersed on a substrate. An alternative method is to grow the tubes on the device substrate. The tubes naturally grow in a roughly vertical fashion starting with a metal seed layer on the substrate. As grown, vertical carbon nanotubes cannot withstand standard MEMS processing such as photolithography.

The vertical carbon nanotubes must be encased in a stabilizing matrix prior to the fabrication of the microfluidic channels that will deliver the analyte. In the past, thermal chemical vapor deposition (CVD) of tetraethylorthosilicate (TEOS) has been used as a stabilizing matrix, but this method requires the use of chemical mechanical polishing (CMP) to planarize the electrode surface and expose the tips of the carbon nanotubes

[103, 121, 122, 124, 125]. The high-temperature CVD TEOS process and accompanying CMP can make this technique expensive, time consuming, and incompatible with other processing requirements for on-chip fluidic channels. To address these limitations, a process based on room temperature CVD deposition of Parylene-C has been developed to replace CVD TEOS. Parylene can conformally coat the CNTs and be etched back using O₂ plasma to expose the CNT tips. This Parylene process completely removes the need for CVD TEOS and CMP.

5.4.1 CNT Nanoarray Electrode Fabrication

CNT nanoarrays are grown on 100 mm diameter silicon wafers. The steps involved in full-wafer electrode fabrication are:

(1) Metal Film Deposition: A 50 nm barrier layer of Ti is deposited using electron beam evaporation on a Si wafer.

(2) Catalyst Deposition: A 35 nm layer of Ni is deposited using electron beam evaporation for use as the CNT growth catalyst.

(3) PECVD CNT Growth: Vertically aligned multi-walled carbon nanotubes (MWCNT) are grown for 30 minutes from the Ni catalyst in a variety of processing conditions. The processing gas used is a mixture of NH₃ and C₂H₂. The highest quality CNT growth is achieved with a NH₃ to C₂H₂ ratio of 110 mtorr: 25 mtorr and 1510 W of power. Average CNT height and diameter is determined using scanning electron microscopy (SEM) to be approximately 5 μm to 8 μm and 100 nm, respectively. A complete characterization of the growth process has been previously reported [103, 121, 122, 124, 125]. See Figure 5-12 for a diagram of the CNT growth chamber [126] and Figure 5-13 for a photograph of the CNT growth in progress.

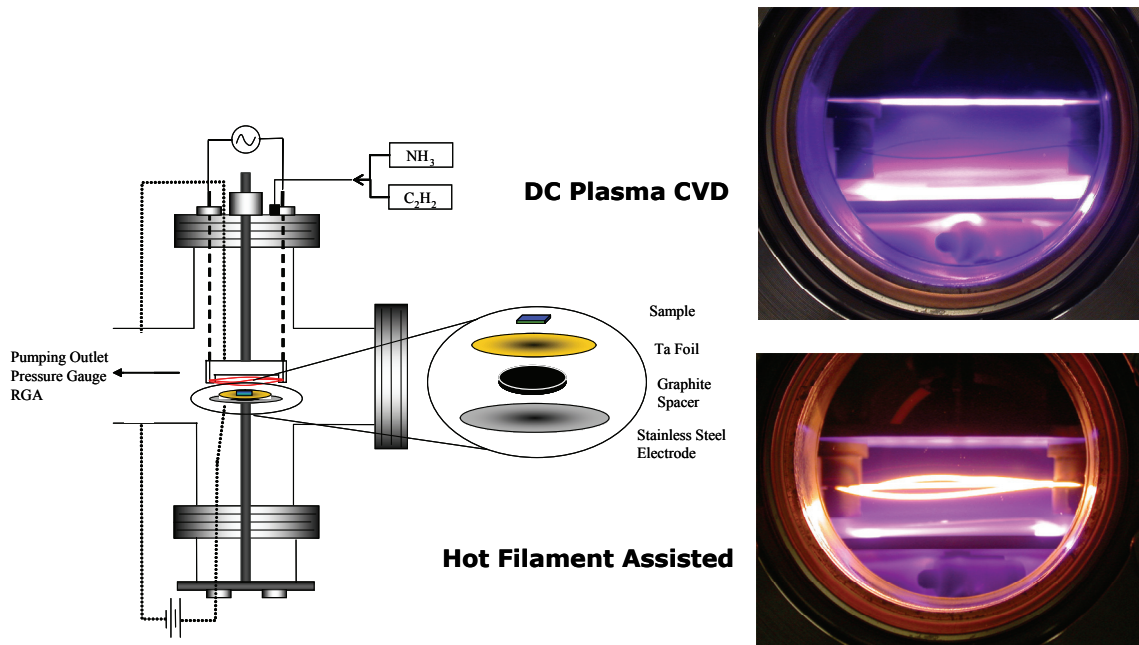


Figure 5-12. PECVD and hot filament assisted vertical CNT growth chamber [126]

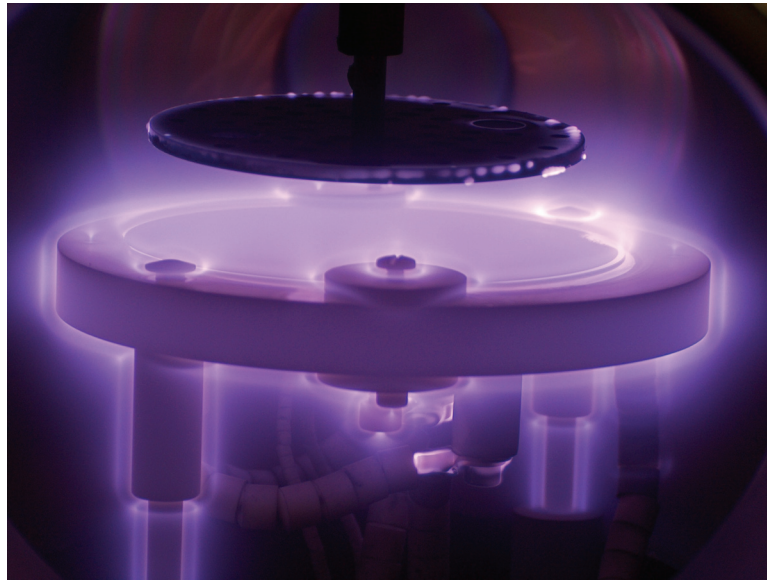


Figure 5-13. Photograph of PECVD vertical CNT growth in progress. Photograph courtesy of Dr. Alan Cassell.

(4) Parylene Deposition and Reflow: Approximately $7 \mu\text{m}$ of Parylene-C is deposited on the wafer. The Parylene deposition is carried out at room temperature using a PDS 2010 Labcoter (Specialty Coating Systems, Indianapolis, IN). After deposition, the wafer is heated to temperatures between 350°C and 375°C for one hour in a N_2 atmosphere to

allow the Parylene to reflow and planarize the surface of the electrode. The wafer is allowed to cool at a rate of 1°C/min. Individually coated CNTs are shown in Figure 5-14 with a 0.34 μm Parylene coating. Figure 5-15a shows CNTs before Parylene deposition.

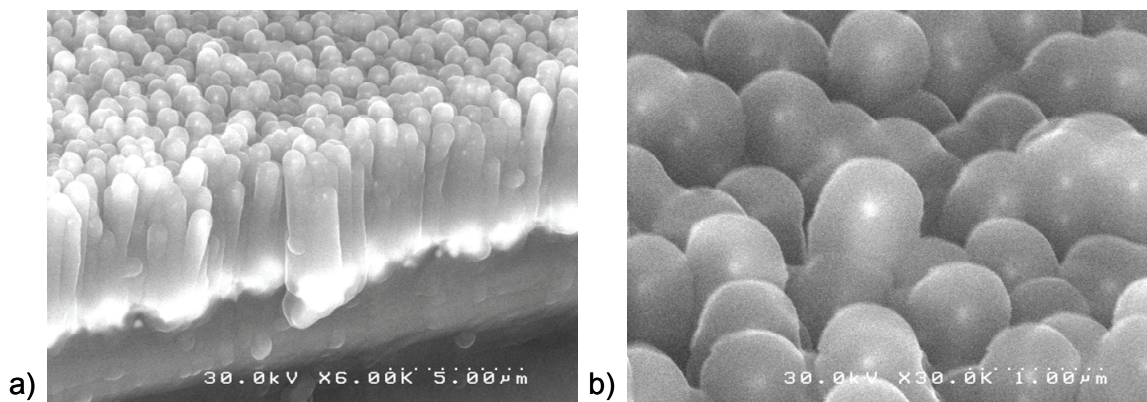


Figure 5-14. Vertical CNTs covered in 0.34 μm of Parylene. (a) Side view of individually coated CNTs 5 to 7 μm in height. (b) Tips of CNTs with Ni seed visible through Parylene coating

(5) CNT Tip Exposure: The Parylene surface is exposed to O_2 plasma to etch several microns of Parylene and reveal CNT tips forming the nanoelectrode array. Figure 5-15b shows a cross-section of the CNT array after completion of the fabrication process. Variations in CNT height in the growth step allowed average tip to tip separation to be controlled through manipulating the O_2 plasma conditions and etch time. The exposed CNT lengths were measured to be approximately 1 μm using SEM and transmission electron microscopy (TEM), but significant length variation was noted (Figure 5-16). SEM and TEM images show that the O_2 plasma can leave some Parylene residue on the exposed stalk. Longer etching times reduce the amount of residue.

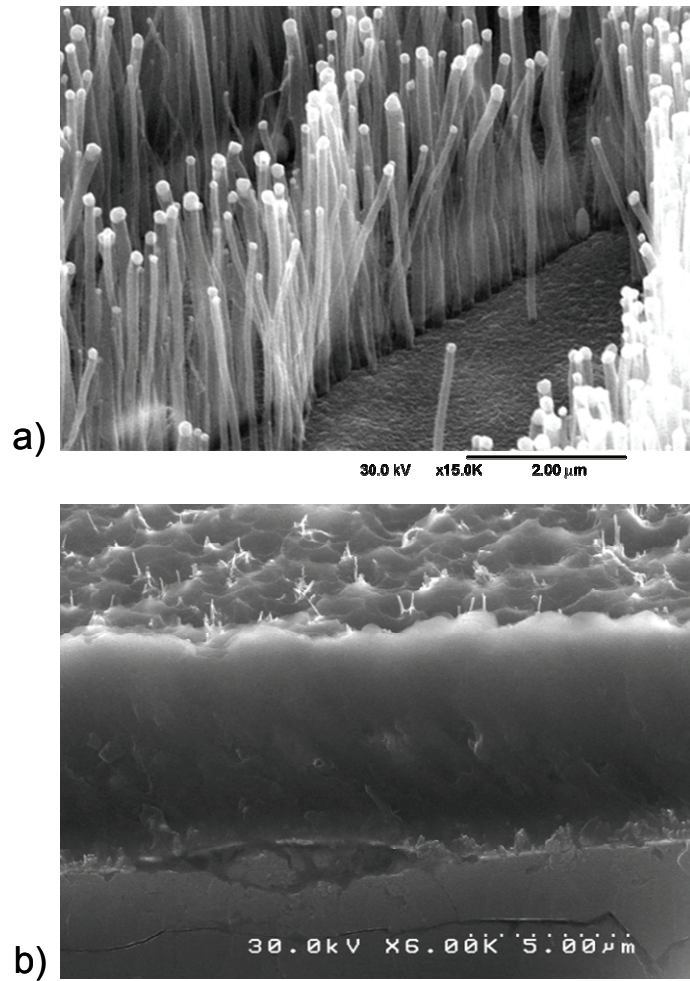


Figure 5-15. (a) CNTs immediately after growth. (b) Cross-section of CNT electrode array. The cross-section image shows the silicon wafer with approximately 7 μm of Parylene embedded CNTs. Approximately 0.5 μm of the CNTs are exposed above the surface of the Parylene. SEM images were taken at a 59 degree tilt angle relative to the surface of the Parylene.

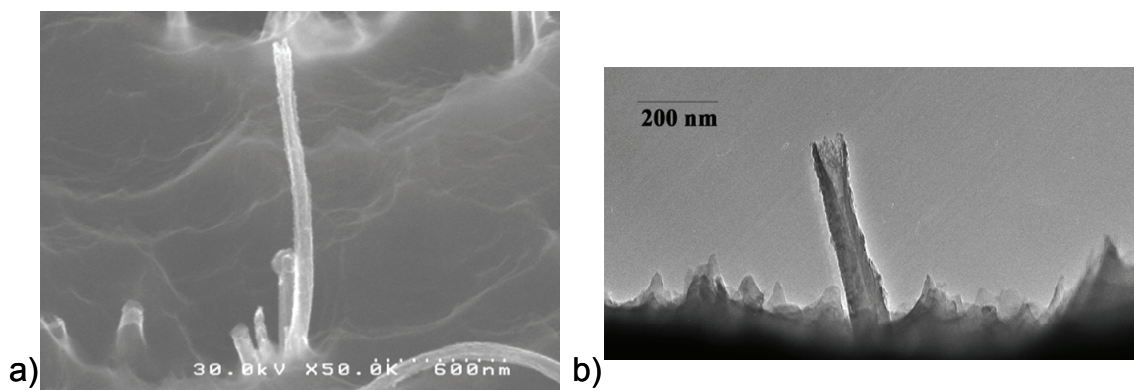


Figure 5-16. (a) SEM of single CNT tip. (b) TEM of single CNT tip. Note removal of Ni seed at the top of the CNT and the removal of Parylene from the exposed tip. SEM image was taken at a 59 degree tilt angle.

(6) Acid Etch: The CNT tips were etched in 1:1:2 ($\text{HNO}_3:\text{H}_2\text{SO}_4:\text{H}_2\text{O}$) for 5 minutes to remove the Ni seeds.

(7) Dicing: The wafer was diced into individual electrode arrays approximately $10 \times 20 \text{ mm}^2$.

Figure 5-17 shows a cross-sectional diagram of the process after steps 2, 3, 4, and 6. A variety of O_2 etch times were tested to achieve the desired tip to tip separation distance of approximately $1 \mu\text{m}$ measured using SEM (Figure 5-18).

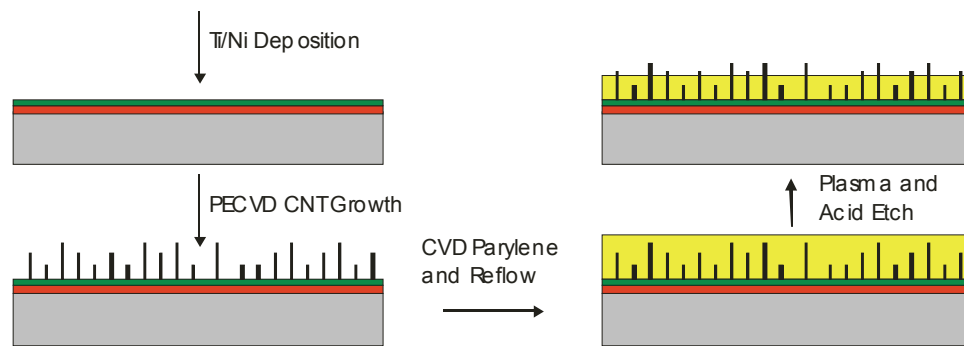


Figure 5-17. Fabrication process flow for CNT nanoarray electrodes

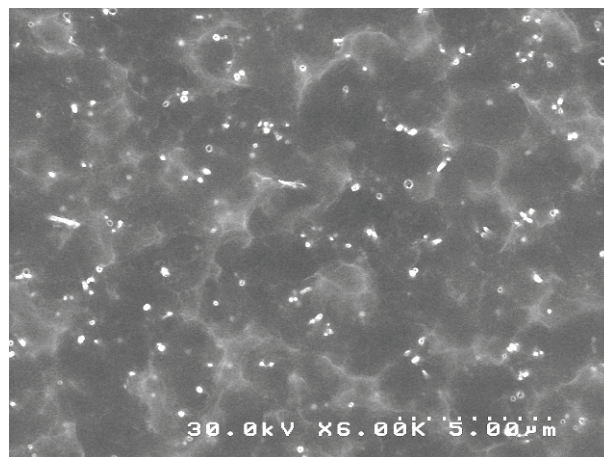


Figure 5-18. Overhead view of CNT electrode array. CNT tip to tip separation is estimated to be approximately $1 \mu\text{m}$.

5.4.2 CNT Electrode Film Patterning

Two methods were tested to pattern the CNT electrode film. The first method used was to pattern the Ti/Ni seed layer using liftoff lithography (Figure 5-19). CNTs were then selectively grown in areas with the seed layer. The second method explored was to fabricate a complete CNT electrode film over the entire wafer and pattern that film using O₂ plasma and a photoresist mask (Figure 5-20). The embedded CNT film etch rate was approximately 0.1 μm/min when etched using a reactive ion etching (RIE) system, three times slower than that of regular Parylene. Both methods successfully produced patterned CNT films, although the full-wafer patterning method is considered more compatible with other potential processing steps.

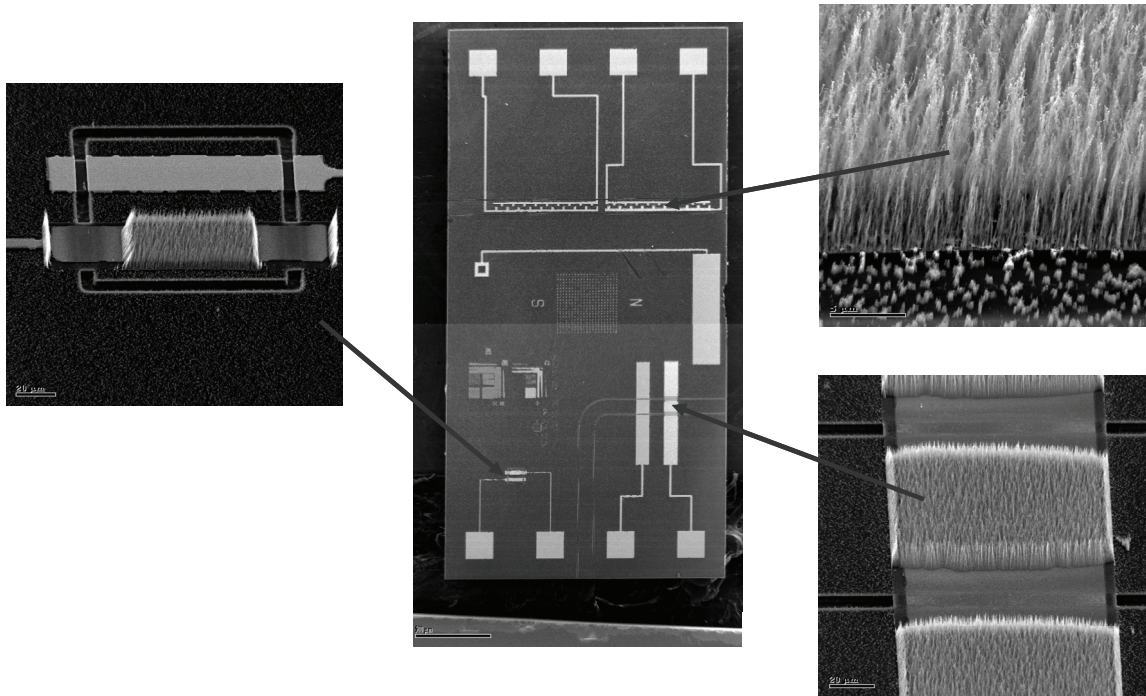


Figure 5-19. CNT growth patterned using Ti/Ni liftoff and selective growth

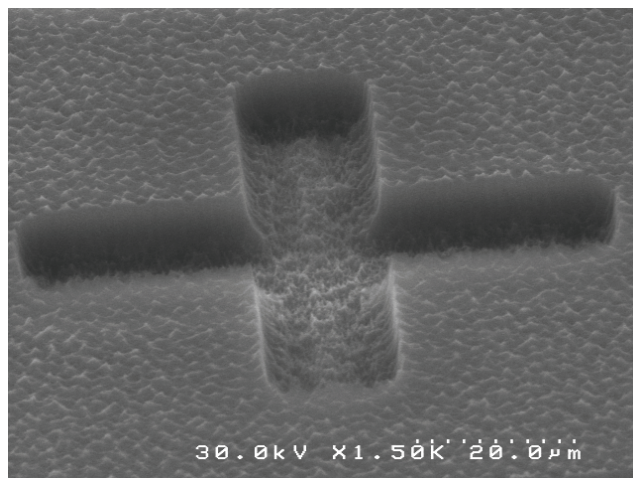


Figure 5-20. Embedded CNT film patterned using O₂ plasma etch

5.5 CNT Nanoarray Characterization

5.5.1 Electrochemical Characterization

All electrochemical measurements were taken using a standard three-electrode configuration. The Parylene-embedded CNT nanoarrays were used as a working electrode and platinum wire was the auxiliary electrode. An Ag/AgCl, KCl (saturated) electrode served as the reference electrode in all experiments. A Princeton Applied Research Model 263A potentiostat (Princeton, NJ) interfaced with PowerSuite software was used to conduct the cyclic voltammetry and record data. K₃Fe(CN)₆ was used as received from Sigma-Aldrich (St. Louis, MO). Stock solution of 100 mM K₃Fe(CN)₆ in 0.1 M KCl was diluted with additional 0.1 M KCl to obtain the desired concentrations of K₃Fe(CN)₆.

The CNT nanoarrays were electrochemically characterized by cyclic voltammetry in 5.0 mM K₃Fe(CN)₆ with 0.1 M KCl at a scan rate of 100 mV/sec. The anodic and cathodic peak separation (ΔE_p) was used as the figure of merit for comparison of

electrode performance. Figure 5-21 shows typical CV scans for platinum, non-isolated CNT nanoarrays, and isolated CNT nanoarrays. Isolated CNT electrodes were attached to an acrylic backing and had all exposed edges covered with epoxy. The isolation protocol improved peak separation from 450 mV in the non-isolated sample to 196 mV in the isolated sample. The isolated CNT electrodes performed comparably to platinum.

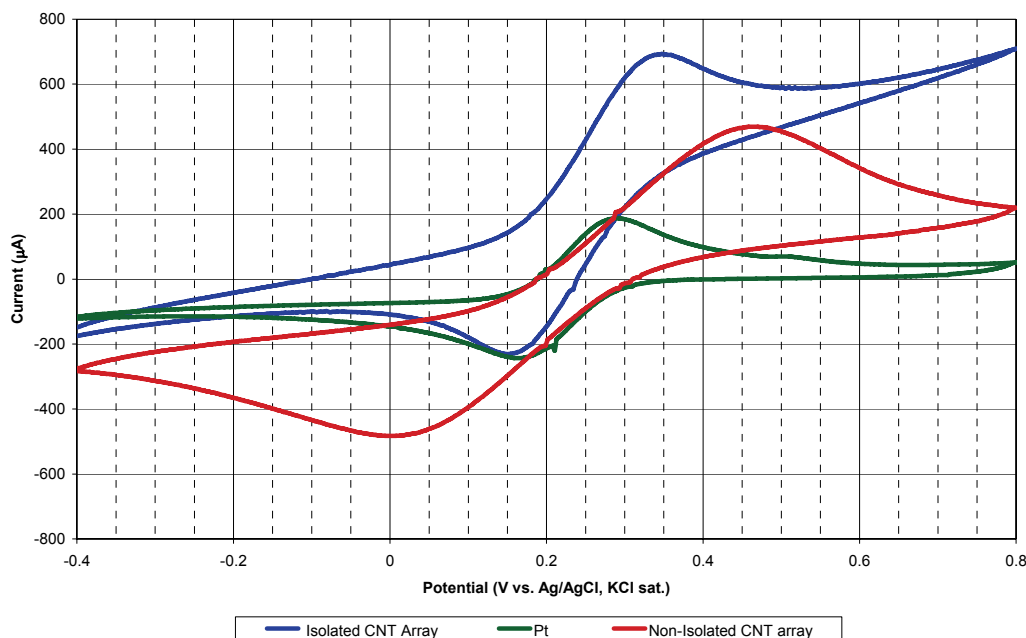


Figure 5-21. Cyclic voltammetry of 5.0 mM $K_3Fe(CN)_6$ in 0.1 M KCl. Scan rate of 100 mV/sec used for three different electrode materials. Pt is included as a standard and has a $\Delta E_p = 120$ mV. The non-isolated CNT array has a $\Delta E_p = 450$ mV. The isolated CNT array has a $\Delta E_p = 196$ mV.

5.5.2 Pretreatment

Various electrochemical pretreatment protocols have been shown to improve electron transfer kinetics on glassy carbon electrodes [127, 128]. The similarity in structure between glassy and graphitic carbon to MWCNTs suggested that similar pretreatment protocols may also be beneficial [125]. To further improve the performance of the isolated CNT nanoelectrodes, a variety of electrochemical pretreatments were tested. Before any isolated nanoelectrode was pretreated a CV was taken in 5.0 mM

$K_3Fe(CN)_6$ with 0.1 M KCl. Only electrodes with an initial $\Delta E_p = 200 \pm 20$ mV were used to test pretreatment conditions. Each treatment was performed on an isolated CNT nanoelectrode before a CV scan was conducted to determine the pretreated ΔE_p value (Table 5-4).

The results show pretreatments of greater than 30 seconds lead to degraded electrode performance compared to untreated electrodes. It is possible that electrochemical pretreatments greater than 30 seconds etch most of the exposed CNT tips causing the observed degradation in performance. CNT tip heights were observed under SEM before and after pretreatments of 30 seconds and were found to be substantially shorter after the pretreatments. In most cases, tips were leveled to the Parylene surface after 30 seconds of pretreatment. Fifteen second pretreatments in H_2SO_4 , HCl, and HNO_3 improved electrode performance. The improvement in performance is possibly due to reduction of oxides and remaining Parylene residue on the surface of the carbon. A 0.8V pretreatment for 15 seconds in HNO_3 gave the best peak separation.

Table 5-4. ΔE_p of $K_3Fe(CN)_6$ after Electrochemical Pretreatment of CNT Nanoelectrodes

	0.6 V/30 s	0.8 V/15 s	1 V/30 s
1.0 M HNO_3			
ΔE_p (mV)	469	123	NR ^a
1.0 M HCl	0.6 V/30 s	0.8 V/15 s	1 V/30 s
ΔE_p (mV)	NT ^b	174	483
1.0 M H_2SO_4	0.6 V/30 s	0.8 V/15 s	1 V/30 s
ΔE_p (mV)	922	167	870
1.0 M KOH	0.6 V/30 s	0.8 V/15 s	1 V/30 s
ΔE_p (mV)	NT ^b	224	856

^a Tested but there was no response

^b Not tested

5.5.3 Additional Electrochemical Characterizations after Pretreatment

Two electrodes were prepared using optimal processing parameters, isolated, and electrochemically pretreated in 1.0 M HNO₃ at 0.8 V for 15 seconds. Solutions of 5.0 mM K₃Fe(CN)₆ in a supporting electrolyte of 0.1 M KCl, phosphate buffered saline (PBS) with pH 7.4, and 0.1 M KCl were prepared. The potential window of the electrode whose boundaries were defined by the onset potentials of water hydrolysis was measured in both 0.1 M KCl and PBS. The water potential window in the 0.1 M KCl was determined to be between approximately -0.35 V and 1.0 V (Figure 5-22a). The potential window in PBS was determined to be approximately -0.6 V to 1.1 V. The potential window of the electrode in 0.1 M KCl and PBS is similar to the reported water potential window of Pt in 1 M H₂SO₄ and pH 7 buffer, respectively [95]. The 0.1 M KCl window is slightly smaller than the size reported for glassy carbon, -1 V to 1 V in 0.1 M KCl [95, 102].

The double layer capacitance, C_{dl} , of the electrode can be estimated from the baseline currents and was found to be approximately 51 $\mu\text{F}/\text{cm}^2$ and 47 $\mu\text{F}/\text{cm}^2$ in 0.1 M KCl and PBS, respectively. The measured C_{dl} is consistent with the expected values for a glassy carbon electrode or the edge plane of a highly-ordered pyrolytic graphite electrode [102]. All normalized values were calculated using the geometric surface area of the electrode submerged in solution.

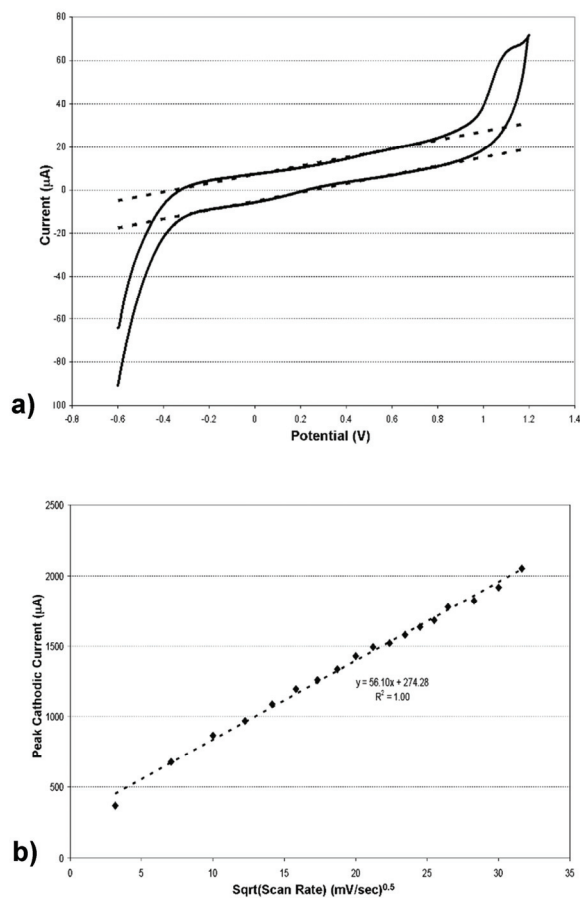


Figure 5-22. Electrochemical characterization of CNT nanoarrays. (a) CV scan of 0.1 M KCl at a scan rate of 100 mV/sec. No significant water hydrolysis occurs between -0.35 V and 1.0 V. The dash line shows the cathodic and anodic baseline currents determined by a linear fit in the potential window. (b) Peak cathodic current versus the square root of scan rate for scan rates between 10 mV/sec and 1 V/sec. The dashed line is a linear fit of the data points showing a nearly perfect linear dependence.

Using the second electrode, cyclic voltammetry scans of the 5.0 mM $K_3Fe(CN)_6$ solution were taken at scan rates ranging from 10 mV/sec to 1 V/sec. For each CV scan, the baseline current due to the uncompensated resistance was determined by a linear fit of the voltammogram in the -0.1 V to 0.1 V range, where no electrochemical activity was observed. The cathodic peak current was measured from the baseline to the voltammogram. Figure 5-22b shows the electrode performed as expected (see Equation (5.2-11)), exhibiting a near perfect linear relationship between the peak cathodic current and the square root of the scan rate.

5.5.4 Sensitivity and Lower Detection Limit

Solutions of concentrations of $\text{K}_3\text{Fe}(\text{CN})_6$ ranging from 0.1 μM to 100 μM in a supporting electrolyte of 0.1 M KCl were prepared. For each concentration, a cyclic voltammetry scan was taken at a scan rate of 100 mV/second, and the baseline current due to the uncompensated resistance was determined by a linear fit of the voltammogram in the -0.1 V to 0.1 V range, where no electrochemical activity was observed. The cathodic peak current was measured from the baseline to the voltammogram. According to equation (5.2-11), a plot of the $\log_{10} i_p$ versus $\log_{10} C$ will produce a line with a slope of one. Figure 5-23 shows a graph of $\log_{10} i_p$ versus $\log_{10} C$ obtained using a CNT electrode. One linear fit is made for concentrations above 100 μM and another for concentrations below 100 μM . The two fits cross at approximately 100 μM . The high-concentration fit has a slope of 0.88 and the low-concentration fit has a slope of 0.308. Both of the slopes are significantly lower than the expected value of one. At higher concentrations, the sensitivity is much closer to the expected linear dependence than at lower concentrations. These results, however, are consistent with previously reported behavior of similar vertical CNT electrodes and other nanoelectrode arrays [103, 129].

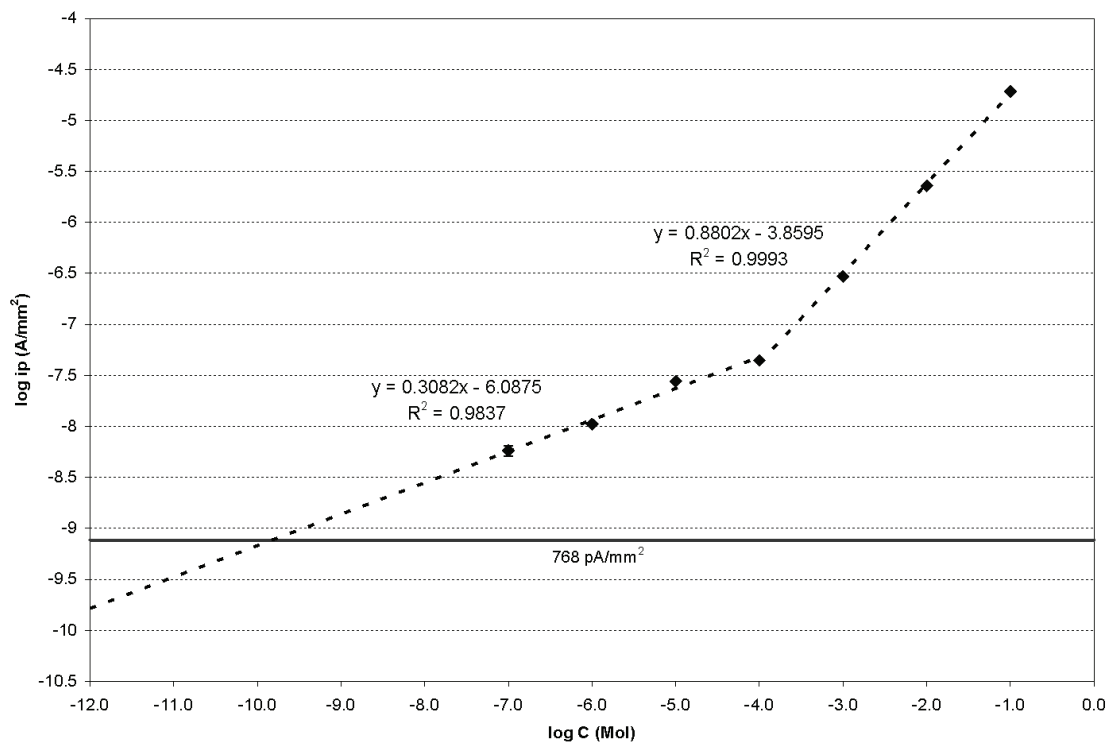


Figure 5-23. Sensitivity measurements of CNT nanoarrays. Plot of the \log_{10} of the measured peak cathodic current relative to background current versus \log_{10} of the concentration of $\text{K}_3\text{Fe}(\text{CN})_6$. The low concentration linear fit (dashed line) has been extended to show its intersection with the lower detection limit (solid red line). This indicates that the lower detection limit could possibly be extended to be on the order of 100 pM. Using current fabrication techniques no signal was detectable for concentrations below 100 nM.

A lower detection limit was determined based on the noise in the baseline current fit. A detectable signal is defined as any current level above twice the root mean square error (RMSE) in the linear baseline fit. The average RMSE was used to calculate the overall lower detection limit of the electrode, which was 768 pA/mm^2 . Assuming the experimentally determined relationship between i_p and C will hold to concentrations below $0.1 \text{ }\mu\text{M}$, it is estimated that a lower detection limit on the order of 100 pM to 1 nM is possible.

5.6 Conclusions

The development of new electrochemical detector working electrode materials with higher potential sensitivity or lower detection limits can greatly aid in the application of electrochemical detection to trace analysis. It is critical to develop new MEMS process compatible materials as HPLC and other trace analysis techniques are miniaturized. Carbon is a promising material because it is well known and widely used in current HPLC electrochemical detectors. Investigations into thin-film carbon and carbon nanotubes will need to continue if these materials are to reach their full potential. Integration of the thin-film carbon onto three dimensional structures can provide significant increases in electrode sensitivity.

Parylene-embedded carbon nanotube nanoelectrode arrays have the potential for ultra-low detection limits while being relatively easy to produce using standard MEMS processes after CNT growth. The CNT electrode films can be patterned either before growth or after being embedded in Parylene. The nanoelectrodes have demonstrated stable electrochemical behavior. The peak separation was comparable to Pt, but the CNT electrodes exhibit a higher background current due to their greater resistivity. A variety of electrochemical pretreatments were tested and several were found to improve electrode performance.

Electrode sensitivity was measured and found to have a nonlinear dependence on bulk concentration. Koehne et al. also observed a similar nonlinear relationship where i_p was proportional to C^α with reported exponents, α , between 0 and 0.2. Koehne et al. theorized that the stabilizing matrix could be adsorbing analyte on its surface leading to local concentrations near the CNTs higher than that in the bulk solution [103, 129]. The C^α relationship results in lower sensitivity, which is normally undesirable. One notable

benefit, however, to the C^α relationship is that it favors lower detection limits since a larger decrease in analyte concentration is necessary before the detected signal is reduced below the background noise level. This nonlinear relationship reduced the electrode's sensitivity but improved its lower detection limit.

Although the tested electrode did not produce a detectable signal when used in 10 nM solution, it is probable that through further refinement of the fabrication process an improvement in lower detection limit of one to three orders of magnitude can be achieved. Furthermore, Koehne et al. made use of a more sensitive electrochemical detection technique known as differential pulse voltammetry (DPV). DPV allows for the subtraction of the double layer charging current greatly reducing the total background noise. The 768 pA/mm² noise floor represents the electronic noise in the detection system but does not account for the background electrochemical noise due to double layer charging. It is possible for the double layer charging current to mask analyte redox signal at very low concentrations. This could explain why detection below 0.1 μ M was impossible even though the electronic noise floor indicates it should be possible. In any system incorporating the CNT nanoelectrode array as a detector, DPV should be investigated and used to improve the detection limit. It should be noted that the confirmed 0.1 μ M lower detection limit is on par with most working electrode materials. Due to their possible lower than average detection limit, the CNT nanoelectrode films may be well suited for use in trace electrochemical analysis. Because of the compatibility with other MEMS fabrication techniques, in the future the CNT nanoelectrodes can be integrated as an electrochemical detector in the nHPLC systems.

6 CONCLUSIONS

The field of microfluidics is young and exciting. From its start as a sub-discipline of MEMS to its current popularity among industrial and academic research, it has been at once challenging and rewarding. The early years of microfluidic research yielded a vast variety of miniaturized microfluidic devices based in silicon. In a short period of time, new materials began to be explored, and polymers became the dominant material in the field. In recent times, entire microfluidic systems have been demonstrated on chip and new areas of application in analytical chemistry, biochemistry, and biology are being explored. The goal of fully integrated, monolithic microfluidic devices still dominates the desires of many researchers. This work represents a distinct departure from this classic microfluidic paradigm.

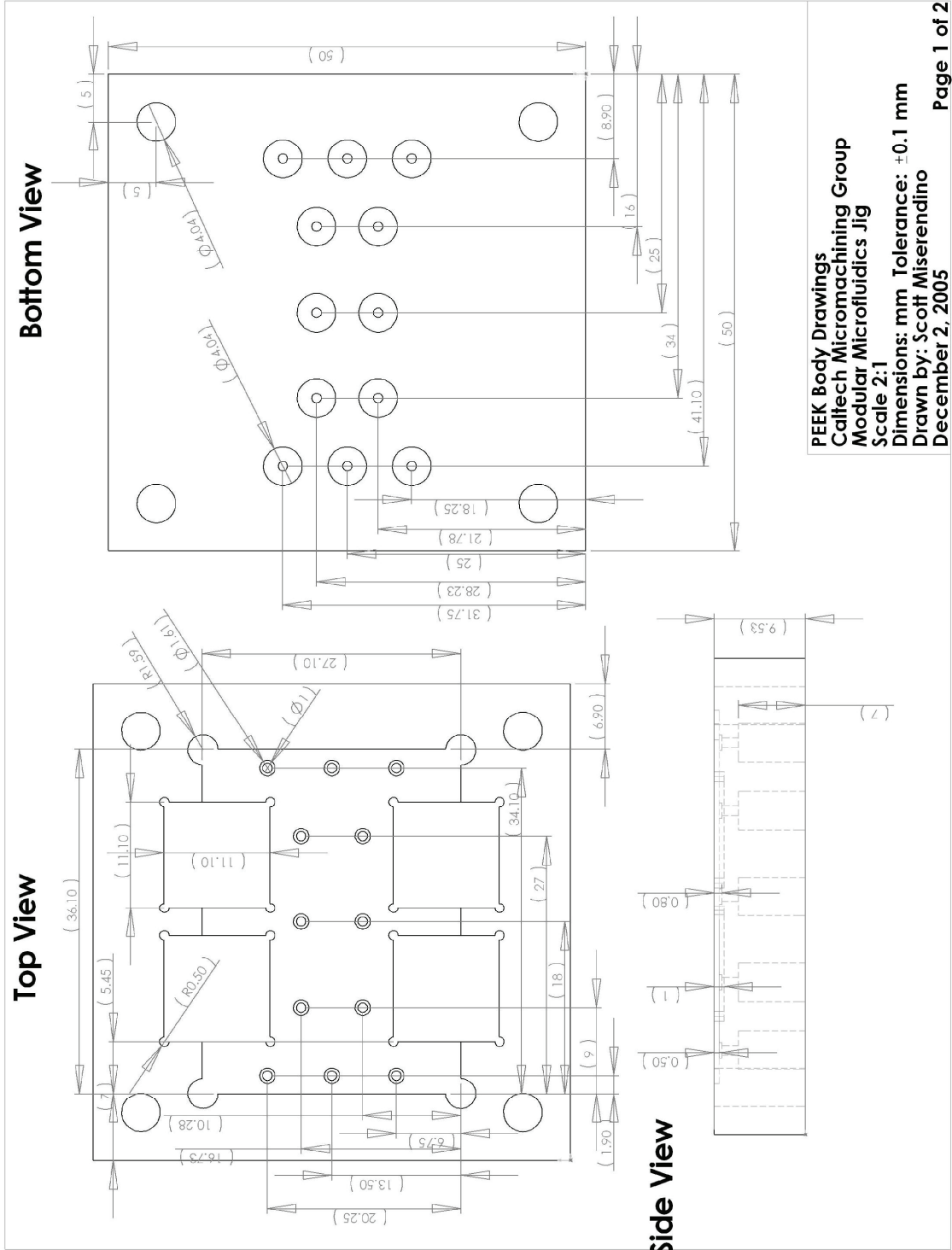
An old approach to new problems is offered as the way forward in microfluidic system design and manufacturing. Much of the microfluidic field recognizes good packaging technologies along with reliable, robust, and reconfigurable microfluidic systems as major challenges for the future. This work addresses those challenges through the development of novel microgasket and MEMS O-ring coupling technology, the promotion of modular microfluidic design, and the implementation of a prototype modular nano high-performance liquid chromatography system with performance on par with some of the best macro HPLC systems. The adoption of the modular design scheme

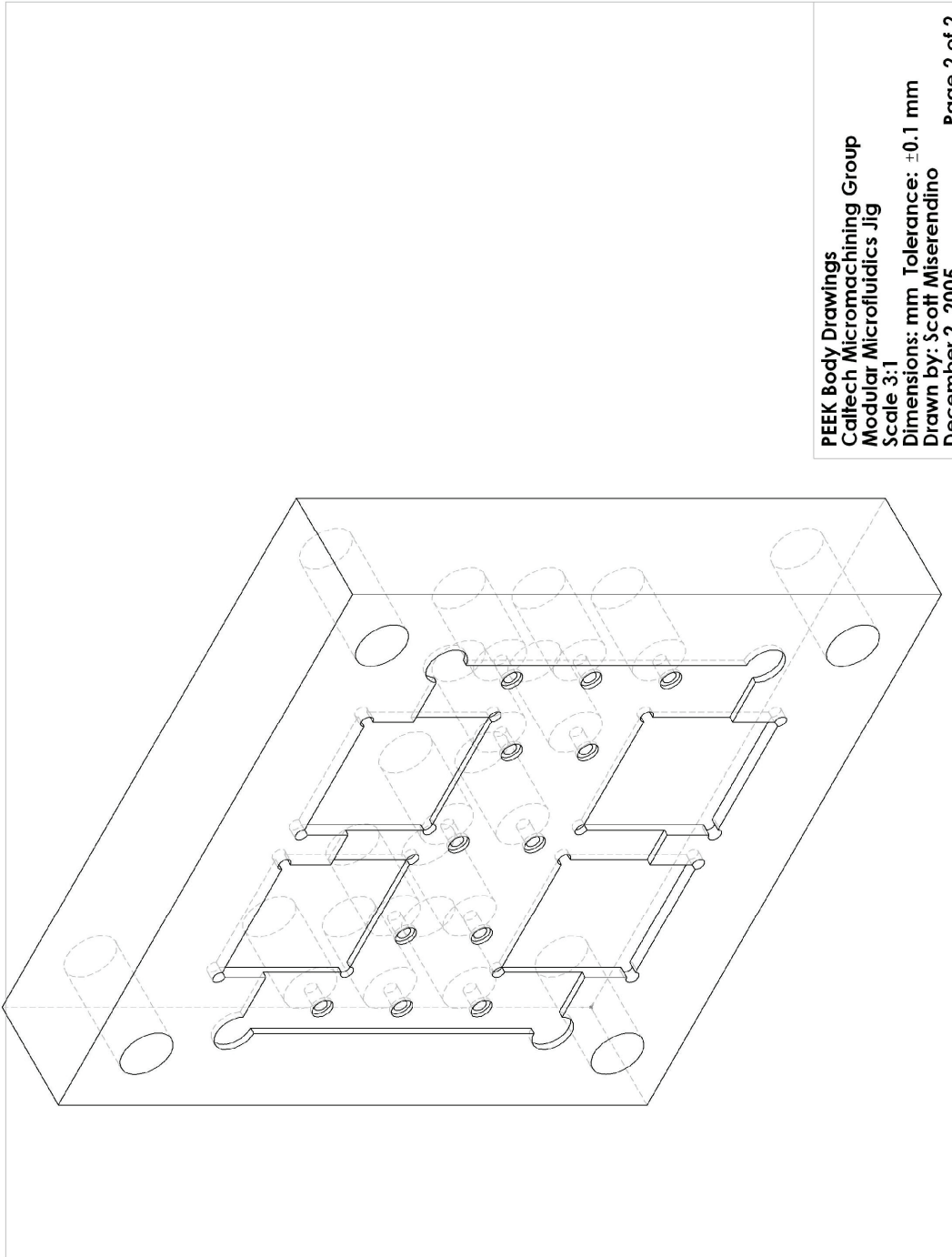
offered here, or something similar, can allow for the much needed standardization of microfluidic components.

No modular microfluidic system is possible without a good solution to the interconnection problem. Integrated microgaskets and MEMS O-rings provide not only practically leak-free operation at typical operating pressures, but also the possible extension of operating pressures and flow rates well above today's standards. The photodefinable silicone microgaskets allow for via dead volumes below 1 nL which is unachievable using any other interconnect technology. The microgaskets also provide a new packaging technique for fully surface micromachined microfluidics, eliminating the need for costly thru-wafer etching. These advances only represent one possible application of the new commercially available photodefinable silicone.

The development of the photodefinable MEMS O-rings has led to the first Parylene microfluidic modular microfluidic system. The prototype nHPLC consists of three individual devices and a single interconnect device. Each device could be fabricated in less than one week with an additional two weeks needed for release. These relatively short device fabrication times (for surface machined microfluidics) have drastically reduced the length of time to next-generation systems. The nHPLC system showed it can achieve performance on par or better than comparable commercial systems. The nHPLC separation also included the refinement of a valveless injection scheme that will make on-chip ion exchange chromatography much more repeatable. It was able to do all of this while maintaining a modular design scheme, allowing for easy part replacement and upgrade.

The component that drove the need for modular design was the electrochemical detector. There was a desire to incorporate a new low detection limit electrochemical detector into the HPLC system without making the system fabrication unnecessarily complicated. The low detection limit electrochemical detector was based on a novel Parylene-embedded vertical carbon nanotube nanoarray working electrode. Testing showed that the CNT nanoarray electrode produced a bifurcated sensitivity profile that allowed for a lower detection limit at the cost of sensitivity. Other novel working electrode materials were also explored. A high effective surface area electrode was developed based on pyrolyzed Parylene. The pyrolyzed Parylene thin film carbon was capable of conformally coating high aspect ratio structures that provide for at least an order of magnitude increase in effective surface area relative to geometric area. While these new materials proved too experimental for the modular nHPLC prototype, the eventual integration into an nHPLC system could make trace analyte detection a possibility. With trace analyte detection and high efficiency analyte separation in a modular microfluidic system, applications such as near real-time, single cell secretion monitoring are on the horizon.





Appendix B: Control Chip Fabrication Recipe

1. **Glass wafer**
 - a. Wafer Type: Soda Lime
 - b. Wafer Thickness: 550 μm
2. **Deposit Parylene (~ 3 μm)**
 - a. Parylene Type: C
 - b. Adhesion Promoter: 400:400:4 IPA:H₂O:A174
 - c. Mass of Parylene dimer: 4.25 g
3. **Lithography for Channels (25 – 30 μm)**
 - a. Mask: Channel Layer
 - b. Stepper Program: Contact Aligner
 - c. Adhesion Promotion: None
 - d. Photoresist Type: AZ4620/AZ4620
 - e. Spin Speed/Time: 1.25 krpm/40 sec (both layers)
 - f. Bake Temp/Time: 100°C for 5 min, 100°C for 30 min
 - g. Exposure Time: 150 sec
 - h. O₂ Descum Pressure/Power/Time: 250 mtorr/400 W/2 min
4. **Hard Bake**
 - a. Temp/Time: 100°C for 3.5 hour
5. **BHF Dip**
 - a. Time: 10 sec
6. **Deposit Parylene (~ 3 μm)**
 - a. Parylene Type: C
 - b. Mass of Parylene dimer: 4.25 g
7. **O₂ Parylene Roughening**
 - a. Plasma type: 100% O₂
 - b. Machine: PEII
 - c. Plasma Pressure/Power/Time: 250 mtorr/400 W/2 min
8. **SU-8 Lithography (~ 50 μm)**
 - a. Mask: SU-8 Layer
 - b. Stepper Program: Contact Aligner
 - c. Adhesion Promoter: None
 - d. SU-8 Spin Speed/Time: 500 rpm/100 rpm/s/10 sec then
2250 rpm/300 rpm/s/30 sec then
3000 rpm/1500 rpm/s/0.5 sec
 - e. SU-8 Prebake Temp/Time: ramp to 65°C @ 555°C/hr hold 4 min ramp to 85°C @ 555°C/hr hold 10 minutes ramp down to 21°C @ 60 C/hr
 - f. SU-8 Exposure Time: 100 sec
 - g. SU-8 PEB: ramp to 65°C @ 555°C/hr ramp to 80 C @ 555°C/hr ramp down to 21 C @ 60°C/hr
 - h. SU-8 Developer Time: 4 min

9. O₂ etch Parylene

- a. Plasma type: 100% O₂
- b. Machine: RIE
- c. Plasma Pressure/Power/Time: 312 mtorr/400 W/15 min (Recipe 3)

10. Silicone Lithography (~ 25 μm)

- a. Mask: Silicone Layer
- b. Stepper Program: Contact Aligner
- c. Silicone Spin Speed/Time: 500 rpm/100 rpm/s/10 sec then
500 rpm/300 rpm/s/30 sec then
1500 rpm/1500 rpm/s/0.5 sec
- d. Silicone Prebake Temp/Time: 110°C for 2 min
- e. Silicone Exposure Time: 100 sec
- f. Silicone PEB Temp/Time: 130°C for 2 min on hot plate
- g. Silicone Developer Time: 3.5 min
- h. Silicone Post Bake: None

11. Silicone Descum

- a. Plasma type: 70 sccm O₂ and 50 sccm SF₆
- b. Machine: RIE
- c. Plasma Pressure/Power/Time: 180 mtorr/180 W/15 min

12. Hard Bake

- a. Temp/Time: 100°C for 30 min (in oven)

13. Dice wafer (top side up)

- a. Passivation Layer: AZ4260 @ 2000 rpm for 40 sec
- b. Passivation Layer Bake: 100°C for 15 min
- c. Depth: 0.250 mm
- d. Index I: By hand
- e. Index II: By hand
- f. Blade Type: Standard
- g. Total Number of Cuts: 6

14. Channel Release

- a. Release agent: IPA @ 80°C for 8 days, Acetone @ 21°C for 3 days

Note: Etching pressures are given as the chamber pressure prior to striking the plasma. Base pressure is included in this value. Typical PEII base pressure is between 25 and 40 mtorr.

Appendix C: Device Chip Fabrication Recipe

1. **Glass wafer**
 - a. Wafer Type: Soda Lime
 - b. Wafer Thickness: 550 μm
2. **Deposit Parylene (~ 3 μm)**
 - a. Parylene Type: C
 - b. Adhesion Promoter: 400:400:4 IPA:H₂O:A174
 - c. Mass of Parylene Dimer: 5.29 g
3. **Lithography for Metal Liftoff**
 - a. Mask: Metal Layer
 - b. Stepper Program: Contact Aligner
 - c. Adhesion Promotion: None
 - d. Photoresist Type: LOR 3B/AZ1518
 - e. Spin Speed/Time: 3 kHz/40 sec (both layers)
 - f. Bake Temp/Time: 190°C for 10 min, 100°C for 30 min
 - g. Exposure Time: 25 sec
 - h. Developer Time: 1 min
 - i. O₂ Descum Pressure/Power/Time: 250 mtorr/400 W/2 min
4. **Hard Bake**
 - a. Temp/Time: 120°C for 2 hr
5. **Deposit Metal**
 - a. Machine: E-beam
 - b. Metal Source: Pt
 - c. Pt Thickness: 2000 Å
6. **Liftoff**
 - a. Stripper used: ST-22 @ 100°C (on digital hotplate)
 - b. Time: 20 min agitate once after 5 min
7. **Descum**
 - a. Plasma type: 100% O₂
 - b. Machine: PEII
 - c. Plasma Pressure/Power/Time: 250 mtorr/400 W/2 min
8. **Lithography for HPLC Channel (25 – 30 μm , 5 μm filters)**
 - a. First Mask: Channel Layer
 - b. Second Mask: Filter Layer
 - c. Stepper Program: Contact Aligner
 - d. Adhesion Promotion: None
 - e. Photoresist Type: AZ4620/AZ4620
 - f. Spin Speed/Time: 1.25 krpm/40 sec (both layers)
 - g. Bake Temp/Time: 100°C for 5 min, 100°C for 30 min
 - h. Exposure Time First Mask: 135 sec
 - i. Exposure Time Second Mask: 40 sec
 - j. Developer: 50 mL AZ351: 100 mL DI H₂O
 - k. Development Time: 4 min

- l. O₂ Descum Pressure/Power/Time: 250 mtorr/400 W/2 min
- 9. Hard Bake**
 - a. Temp/Time: 100°C for 2.75 hour
- 10. BHF Dip**
 - a. Time: 10 sec
- 11. Deposit Parylene (~ 3 μm)**
 - a. Parylene Type: C
 - b. Mass of Parylene dimer: 4.56 g
- 12. O₂ Parylene Roughening**
 - a. Plasma type: 100% O₂
 - b. Machine: PEII
 - c. Plasma Pressure/Power/Time: 250 mtorr/400 W/2 min
- 13. SU-8 Lithography (~ 50 μm)**
 - a. Mask: SU-8 Layer
 - b. Stepper Program: Contact Aligner
 - c. Adhesion Promoter: None
 - d. SU-8 Spin Speed/Time: 500 rpm/100 rpm/s/10 sec then
2250 rpm/300 rpm/s/30 sec then
3000 rpm/1500 rpm/s/0.5 sec
 - e. SU-8 Prebake Temp/Time: ramp to 65°C @ 555 C/hr hold 4 min ramp to 85°C @ 555°C/hr hold 10 minutes ramp down to 21°C @ 60°C/hr
 - f. SU-8 Exposure Time: 100 sec
 - g. SU-8 PEB: ramp to 65°C @ 555°C/hr ramp to 80°C @ 555°C/hr ramp down to 21°C @ 60°C/hr
 - h. SU-8 Developer Time: 4 min
- 14. Lithography for Parylene etch**
 - a. Mask: Pary Etch
 - b. Stepper Program: Contact Aligner
 - c. Adhesion Promotion: None
 - d. Photoresist Type: AZ4620
 - e. Spin Speed/Time: 1000 rpm/40 sec
 - f. Bake Temp/Time: 100°C for 30 min
 - g. Exposure Time: 250 sec
- 15. O₂ etch Parylene**
 - a. Plasma type: 100% O₂
 - b. Machine: RIE
 - c. Plasma Pressure/Power/Time: 315 mtorr/400 W/15 min (Recipe 3)
- 16. Strip PR**
 - a. Stripper used: Acetone/IPA
- 17. Dice wafer (top side up)**
 - a. Passivation Layer: AZ4620 @ 2000 rpm for 40 sec
 - b. Passivation Layer Bake: 100°C for 15 min
 - c. Depth: 0.250 mm
 - d. Index I: By hand
 - e. Index II: By hand
 - f. Blade Type: Standard

g. Total Number of Cuts: 18

18. Channel Release

a. Release agent: IPA at 80°C for 14 days

Note: Etching pressures are given as the chamber pressure prior to striking the plasma. Base pressure is included in this value. Typical PEII base pressure is between 25 and 40 mtorr.

References

- [1] M. Riordan and L. Hoddeson, *Crystal fire: the birth of the information age*, 1st ed. New York: Norton, 1997.
- [2] G. Moore, "Cramming more components onto integrated circuits," *Electronics*, vol 38, issue 8, 1965.
- [3] K. E. Petersen, "Silicon as a Mechanical Material," *Proceedings of the IEEE*, vol. 70, pp. 420-457, 1982.
- [4] L. S. Fan, Y. C. Tai, and R. S. Muller, "Integrated Movable Micromechanical Structures for Sensors and Actuators," *IEEE Transactions on Electron Devices*, vol. 35, pp. 724-730, Jun 1988.
- [5] C. M. Ho and Y. C. Tai, "Micro-electro-mechanical-systems (MEMS) and fluid flows," *Annual Review of Fluid Mechanics*, vol. 30, pp. 579-612, 1998.
- [6] S. Shoji and M. Esashi, "Microflow Devices and Systems," *Journal of Micromechanics and Microengineering*, vol. 4, pp. 157-171, Dec 1994.
- [7] N.-T. Nguyen and S. T. Wereley, *Fundamentals and applications of microfluidics*. Boston, MA: Artech House, 2002.
- [8] A. Manz, N. Graber, and H. M. Widmer, "Miniaturized Total Chemical-Analysis Systems - a Novel Concept for Chemical Sensing," *Sensors and Actuators B-Chemical*, vol. 1, pp. 244-248, Jan 1990.
- [9] G. M. Whitesides, "The origins and the future of microfluidics," *Nature*, vol. 442, pp. 368-373, 2006.
- [10] J. C. McDonald, D. C. Duffy, J. R. Anderson, D. T. Chiu, H. K. Wu, O. J. A. Schueller, and G. M. Whitesides, "Fabrication of microfluidic systems in poly(dimethylsiloxane)," *Electrophoresis*, vol. 21, pp. 27-40, Jan 2000.
- [11] M. A. Unger, H. P. Chou, T. Thorsen, A. Scherer, and S. R. Quake, "Monolithic microfabricated valves and pumps by multilayer soft lithography," *Science*, vol. 288, pp. 113-116, Apr 7 2000.
- [12] A. M. Christensen, D. A. Chang-Yen, and B. K. Gale, "Characterization of interconnects used in PDMS microfluidic systems," *Journal of Micromechanics and Microengineering*, vol. 15, pp. 928-934, May 2005.
- [13] K. A. Shaikh, K. S. Ryu, E. D. Goluch, J. M. Nam, J. W. Liu, S. Thaxton, T. N. Chiesl, A. E. Barron, Y. Lu, C. A. Mirkin, and C. Liu, "A modular microfluidic architecture for integrated biochemical analysis," *Proceedings of the National*

Academy of Sciences of the United States of America, vol. 102, pp. 9745-9750, Jul 12 2005.

- [14] P. F. Man, D. K. Jones, and C. H. Mastrangelo, "Microfluidic plastic capillaries on silicon substrates: A new inexpensive technology for bioanalysis chips," *Proceedings of MEMS 97*, Nagoya, Japan, 1997.
- [15] G. T. A. Kovacs, *Micromachined transducers sourcebook*. Boston, Ma.: WCB, 1998.
- [16] D. Bhusari, H. A. Reed, M. Wedlake, A. M. Padovani, S. A. B. Allen, and P. A. Kohl, "Fabrication of air-channel structures for microfluidic, microelectromechanical, and microelectronic applications," *Journal of Microelectromechanical Systems*, vol. 10, pp. 400-408, Sep 2001.
- [17] Y. N. Xia and G. M. Whitesides, "Soft lithography," *Angewandte Chemie-International Edition*, vol. 37, pp. 551-575, Mar 16 1998.
- [18] J. N. Lee, C. Park, and G. M. Whitesides, "Solvent compatibility of poly(dimethylsiloxane)-based microfluidic devices," *Analytical Chemistry*, vol. 75, pp. 6544-6554, Dec 1 2003.
- [19] S. C. Terry, J. H. Jerman, and J. B. Angell, "Gas-Chromatographic Air Analyzer Fabricated on a Silicon-Wafer," *IEEE Transactions on Electron Devices*, vol. 26, pp. 1880-1886, 1979.
- [20] P. A. Auroux, D. Iossifidis, D. R. Reyes, and A. Manz, "Micro total analysis systems. 2. Analytical standard operations and applications," *Analytical Chemistry*, vol. 74, pp. 2637-2652, Jun 15 2002.
- [21] D. R. Reyes, D. Iossifidis, P. A. Auroux, and A. Manz, "Micro total analysis systems. 1. Introduction, theory, and technology," *Analytical Chemistry*, vol. 74, pp. 2623-2636, Jun 15 2002.
- [22] T. Vilkner, D. Janasek, and A. Manz, "Micro total analysis systems. Recent developments," *Analytical Chemistry*, vol. 76, pp. 3373-3385, Jun 15 2004.
- [23] C. Haber, "Microfluidics in commercial applications; an industry perspective," *Lab on a Chip*, vol. 6, pp. 1118-1121, 2006.
- [24] Lionix BV, "Modular lab-on-a-chip systems," <http://www.lionixbv.nl/microfluidics/matras.html>, 2007.
- [25] S. Miserendino and Y.-C. Tai, "Photodefinable Silicone MEMS Gaskets and O-rings for Microfluidics Packaging," *Proceedings of MEMS 2007*, Kobe, Japan, 2007.

- [26] S. D. Suk, S. Chang, and Y. H. Cho, "Design, fabrication, and characterization of electrical and fluidic interconnections for a multi-chip microelectrofluidic bench," *Proceedings of Proc. MEMS 2005*, Miami, FL, pp. 658-661, 2005.
- [27] Specialty Coating Systems, "Parylene knowledge: Discovery/History," http://www.scscoatings.com/Parylene_knowledge/history.cfm, 2007.
- [28] Specialty Coating Systems, "Parylene knowledge: Specifications and Properties," http://www.scscoatings.com/Parylene_knowledge/specifications.cfm, 2007.
- [29] D. C. Rodger, J. D. Weiland, M. S. Humayun, and Y. C. Tai, "Scalable high lead-count Parylene package for retinal prostheses," *Sensors and Actuators B: Chemical*, vol. 117, pp. 107-114, Sep 12 2006.
- [30] N. Stark, "Literature Review: Biological Safety of Parylene C," *Medical Plastics and Biomaterials*, vol 3, issue 2, 1996.
- [31] J. E. Mark, *Polymer data handbook*. New York: Oxford University Press, 1999.
- [32] J.-H. Lee and W. Y. Ji, "Electrical and Mechanical Properties of Silicone Rubber for High Voltage Insulation," *Proceedings of International Conference on Properties and Applications of Dielectric Materials*, Nagoya, Japan, 2003.
- [33] B. Bhushan and Z. Burton, "Adhesion and friction properties of polymers in microfluidic devices," *Nanotechnology*, vol. 16, pp. 467-478, Apr 2005.
- [34] C. Gonzalez, S. D. Collins, and R. L. Smith, "Fluidic interconnects for modular assembly of chemical microsystems," *Sensors and Actuators B-Chemical*, vol. 49, pp. 40-45, Jun 25 1998.
- [35] P.-J. Chen, D. C. Rodger, E. Meng, M. S. Humayun, and Y.-C. Tai, "Surface-micromachined in-channel Parylene dual valves for unpowered microflow regulation," *Proceedings of Hilton Head 2006 Workshop*, Hilton Head, SC, 2006.
- [36] J. Xie, J. Shih, C. Pang, Y.-C. Tai, Y. Miao, and T. D. Lee, "An integrated LC-ESI chip with electrochemical-based gradient generation," *Proceedings of MEMS 2003*, Kyoto, Japan, pp. 334-337, 2003.
- [37] E. Meng, P.-J. Chen, D. Rodger, Y.-C. Tai, and M. Humayun, "Implantable Parylene MEMS for glaucoma therapy," *Proceedings of IEEE EMBS Conference on Microtechnologies in Medicine and Biology*, Kahuku, HI, 2005.
- [38] Q. He, C. Pang, Y.-C. Tai, and T. D. Lee, "Ion liquid chromatography on-a-chip with beads-packed Parylene column," *Proceedings of MEMS 2004*, Maastricht, the Netherlands, pp. 212-215, 2004.

- [39] C. Y. Shih, Y. Chen, J. Xie, Q. He, and Y. C. Tai, "On-Chip Temperature Gradient Liquid Chromatography," *Proceedings of MEMS 2005*, Istanbul, Turkey, 2005.
- [40] S. Whitaker, *Introduction to fluid mechanics*, Reprint ed. Malabar, Fla.: Krieger, 1981.
- [41] P. A. Thompson and S. M. Troian, "A general boundary condition for liquid flow at solid surfaces," *Nature*, vol. 389, pp. 360-362, Sep 25 1997.
- [42] J. A. Diez, R. Gratton, L. P. Thomas, and B. Marino, "Laplace Pressure-Driven Drop Spreading," *Physics of Fluids*, vol. 6, pp. 24-33, Jan 1994.
- [43] T. Young, "An Essay on the Cohesion of Fluids," *Philosophical Transactions of the Royal Society of London*, vol. 95, pp. 65-87, 1805.
- [44] R. E. Collins and C. E. Cooke, "Fundamental Basis for the Contact Angle and Capillary Pressure," *Transactions of the Faraday Society*, vol. 55, pp. 1602-1606, 1959.
- [45] P. G. Wapner and W. P. Hoffman, "Utilization of surface tension and wettability in the design and operation of microsensors," *Sensors and Actuators B-Chemical*, vol. 71, pp. 60-67, Nov 15 2000.
- [46] L. J. Yang, T. J. Yao, and Y. C. Tai, "The marching velocity of the capillary meniscus in a microchannel," *Journal of Micromechanics and Microengineering*, vol. 14, pp. 220-225, Feb 2004.
- [47] A. R. Berker, "Integration des equations du mouvement d'un fluide visqueux incompressible," *Handbuch der Physik*. vol. 8, S. Flugge, Ed. Berlin: Springer, p. 384, 1963.
- [48] R. K. Shah and A. L. London, *Laminar flow forced convection in ducts : a source book for compact heat exchanger analytical data*. New York: Academic Press, 1978.
- [49] M. Bahrami, M. M. Yovanovich, and J. R. Culham, "Pressure drop of fully developed, laminar flow in rough microtubes," *Journal of Fluids Engineering-Transactions of the Asme*, vol. 128, pp. 632-637, May 2006.
- [50] F. M. White, *Viscous fluid flow*, 2nd ed. New York: McGraw-Hill, 1991.
- [51] I. Papautsky, J. Brazzle, T. Ameal, and A. B. Frazier, "Laminar fluid behavior in microchannels using micropolar fluid theory," *Sensors and Actuators a-Physical*, vol. 73, pp. 101-108, Mar 9 1999.

- [52] J. M. Koo and C. Kleinstreuer, "Liquid flow in microchannels: experimental observations and computational analyses of microfluidics effects," *Journal of Micromechanics and Microengineering*, vol. 13, pp. 568-579, Sep 2003.
- [53] B. R. Thompson, D. Maynes, and B. W. Webb, "Characterization of the hydrodynamically developing flow in a microtube using MTV," *Journal of Fluids Engineering-Transactions of the Asme*, vol. 127, pp. 1003-1012, Sep 2005.
- [54] H. S. S. Hsiao, B. J. Hamrock, and J. H. Tripp, "Stream functions and streamlines for visualizing and quantifying side flows in EHL of elliptical contacts," *Journal of Tribology-Transactions of the Asme*, vol. 123, pp. 603-607, Jul 2001.
- [55] M. S. Greywall, "Streamwise Computation of 3-Dimensional Incompressible Potential Flows," *Journal of Computational Physics*, vol. 78, pp. 178-193, Sep 1988.
- [56] M. S. Greywall, "Streamwise Computation of 3-Dimensional Flows Using 2 Stream Functions," *Journal of Fluids Engineering-Transactions of the ASME*, vol. 115, pp. 233-238, Jun 1993.
- [57] D. Knight and G. Mallinson, "Visualizing unstructured flow data using dual stream functions," *IEEE Transactions on Visualization and Computer Graphics*, vol. 2, pp. 355-363, Dec 1996.
- [58] L. R. Huang, E. C. Cox, R. H. Austin, and J. C. Sturm, "Continuous particle separation through deterministic lateral displacement," *Science*, vol. 304, pp. 987-990, May 14 2004.
- [59] D. W. Inglis, J. A. Davis, R. H. Austin, and J. C. Sturm, "Critical particle size for fractionation by deterministic lateral displacement," *Lab on a Chip*, vol. 6, pp. 655-658, 2006.
- [60] S. Zheng, Y.-C. Tai, and H. Kasdan, "A micro device for separation of erythrocytes and leukocytes in human blood," *Proceedings of 27th Annual International Conference of the IEEE Engineering in Medicine and Biology Society (EMBS)*, Shanghai, China, 2005.
- [61] C. K. Fredrickson and Z. H. Fan, "Macro-to-micro interfaces for microfluidic devices," *Lab on a Chip*, vol. 4, pp. 526-533, 2004.
- [62] L. D. Koffman, M. S. Plesset, and L. Lees, "Theory of Evaporation and Condensation," *Physics of Fluids*, vol. 27, pp. 876-880, 1984.
- [63] K. J. Beverley, J. H. Clint, and P. D. I. Fletcher, "Evaporation rates of pure liquids measured using a gravimetric technique," *Physical Chemistry Chemical Physics*, vol. 1, pp. 149-153, Jan 1 1999.

- [64] M. Zimmermann, S. Bentley, H. Schmid, P. Hunziker, and E. Delamarche, "Continuous flow in open microfluidics using controlled evaporation," *Lab on a Chip*, vol. 5, pp. 1355-1359, 2005.
- [65] E. Meng, "MEMS technology and devices for a micro fluid dosing system," Ph. D. Thesis in Electrical Engineering, Pasadena, CA: California Institute of Technology, 2003.
- [66] W. van der Wijngaart, H. Andersson, P. Enoksson, K. Noren, and G. Stemme, "The First Self-Priming and Bi-Directional Valve-less Diffuser Micropump for Both Liquid and Gas," *MEMS 2000 Miyazaki, Japan*, pp. 674-679, 2000.
- [67] J.-H. Tsai and L. Lin, "Micro-to-macro fluidic interconnects with an integrated polymer sealant," *Journal of Micromechanics and Microengineering*, vol. 11, pp. 577-581, 2001.
- [68] P. F. Man, D. K. Jones, and C. H. Mastrangelo, "Microfluidic Plastic Interconnects For Multi-bioanalysis Chip Modules," *SPIE-Int. Soc. Opt. Eng. Proceedings of SPIE- Micromachined Devices and Components III*. vol. 3224 Austin, TX, pp. 196-200, 1997.
- [69] C. González, S. D. Collins, and R. L. Smith, "Fluidic interconnects for modular assembly of chemical microsystems," *Sensors and Actuators B*, vol. 49, pp. 40-45, 1998.
- [70] A. Puntambekar and C. H. Ahn, "Self-aligning microfluidic interconnects for glass- and plastic-based microfluidic systems," *Journal of Micromechanics and Microengineering*, vol. 12, pp. 35-40, 2002.
- [71] B. L. Gray, D. Jaeggi, N. J. Mourlas, B. P. van Driehuisen, K. R. Williams, and N. I. Maluf, "Novel interconnection technologies for integrated microfluidic systems," *Sensors & Actuators A*, vol. 77, pp. 57-65, 1999.
- [72] T. J. Yao, S. W. Lee, W. Fang, and Y. C. Tai, "A Micromachined Rubber O-Ring Microfluidic Coupler," *MEMS 2000 Miyazaki, Japan*, pp. 624-627, 2000.
- [73] E. Meng, S. Y. Wu, and Y. C. Tai, "Silicon couplers for microfluidic applications," *Fresenius Journal of Analytical Chemistry*, vol. 371, pp. 270-275, Sep 2001.
- [74] V. L. Spiering, J. N. van der Moolen, G.-J. Burger, and A. van den Berg, "Novel microstructures and technologies applied in chemical analysis techniques," *Transducers '97 Chicago, IL*, pp. 511-514, 1997.
- [75] C. R. Friedrich, R. R. K. Avula, and S. Gugale, "A fluid microconnector seal for packaging applications," *Journal of Micromechanics and Microengineering*, vol. 15, pp. 1115-1124, Jun 2005.

- [76] R. P. Goel, "Analysis of an Interference-Fit Pin Connection," *IEEE Transactions on Components Hybrids and Manufacturing Technology*, vol. 1, pp. 248-251, 1978.
- [77] J. B. Choi and R. S. Lakes, "Design of a Fastener Based on Negative Poissons Ratio Foam," *Cellular Polymers*, vol. 10, pp. 205-212, 1991.
- [78] D. E. Czernik, *Gaskets : design, selection, and testing*. New York: McGraw-Hill, 1996.
- [79] "ASME Boiler and Pressure Vessel Code," ASME, New York, 2001.
- [80] D. B. Rossheim and R. C. Markl, "Gasket-Loading Constants," *Mechanical Engineering*, vol. 65, pp. 647-648, 1943 1943.
- [81] A. H. Bouzid and M. Derenne, "Analytical modeling of the contact stress with nonlinear gaskets," *Journal of Pressure Vessel Technology-Transactions of the ASME*, vol. 124, pp. 47-53, Feb 2002.
- [82] Q. He, "Integrated Nano Liquid Chromatography System On-a-Chip," Ph. D. Thesis in Electrical Engineering, Pasadena, CA: California Institute of Technology, 2006.
- [83] C. Grosjean, "Silicone MEMS for Fluidics," Ph. D. Thesis in Electrical Engineering, Pasadena, CA: California Institute of Technology, 2001.
- [84] G. Gardner, B. Harkness, E. Ohare, H. Meynen, M. V. Bulcke, M. Gonzalez, and E. Beyne, "Integration of a low stress photopatternable silicone into a wafer level package," *Proceedings of Electronic Components and Technology Conference 2004*, Las Vegas, Nevada, 2004.
- [85] H. Meynen, M. V. Bulcke, M. Gonzalez, B. Harkness, G. Gardner, J. Sudbury-Holtschlag, B. Vandavelde, C. Winters, and E. Beyne, "Ultra low stress and low temperature patternable silicone materials for applications within microelectronics," *Microelectronic Engineering*, vol. 76, pp. 212-218, Oct 2004.
- [86] F. Y. Shih, B. R. Harkness, G. B. Gardner, J. S. Alger, M. R. Cummings, and J. L. Princing, "Photopatternable Silicone Compositions for Electronics Packaging Applications," *Proceedings of International Conference on Electronic Packaging Technology 2003*, Shanghai, China, 2003.
- [87] "Information About Dow Corning Brand Low-Stress Patternable Silicone Materials," Dow Corning Corporation, Manufacturer's datasheet, 2003.
- [88] J. R. Thorpe, D. P. Steenson, and R. E. Miles, "High frequency transmission line using micromachined polymer dielectric," *Electronics Letters*, vol. 34, pp. 1237-1238, 1998.

- [89] J. Kling, "Moving diagnostics from the bench to the bedside," *Nat Biotech*, vol. 24, pp. 891-893, 2006.
- [90] C. Gonzalez, S. D. Collins, and R. L. Smith, "Fluidic interconnects for modular assembly of chemical microsystems," *Sensors and Actuators B: Chemical*, vol. 49, pp. 40-45, 1998.
- [91] U. D. Neue, *HPLC columns: theory, technology, and practice*. New York: Wiley-VCH, 1997.
- [92] R. P. W. Scott, "Basic Instrumentation for Chromatography: High-Performance Liquid Chromatography," *Analytical instrumentation handbook*, 2nd ed, G. W. Ewing, Ed. New York: M. Dekker, pp. xii, 1453 p., 1997.
- [93] U. D. Neue, *HPLC columns : theory, technology, and practice*. New York: Wiley-VCH, 1997.
- [94] W. R. LaCourse, *Pulsed electrochemical detection in high performance liquid chromatography*. New York: Wiley, 1997.
- [95] A. J. Bard and L. R. Faulkner, *Electrochemical methods : fundamentals and applications*, 2nd ed. New York: Wiley, 2001.
- [96] A. P. O'Neill, P. O'Brien, J. Alderman, D. Hoffman, M. McEnery, J. Murrphy, and J. D. Glennon, "On-chip definition of picolitre sample injection plugs for miniaturised liquid chromatography," *Journal of Chromatography A*, vol. 924, pp. 259-263, Jul 27 2001.
- [97] ZirChrom Separations, Inc., "ZirChrom-WAX: Recommendations for use, cleaning and storage of zirconia-based HPLC columns," <http://www.zirchrom.com/pdf/WAXCare.pdf>, 2007.
- [98] Bischoff Chromatography, "Pronto-Pearl: A new generation of packings for ultra fast HPLC," <http://www.bischoff-chrom.de/?url=prontoppearl&lang=en>, 2007.
- [99] Agilent Technologies, "ZORBAX reverse phase HPLC columns," <http://www.chem.agilent.com/Scripts/PDS.asp?lPage=2113>, 2007.
- [100] G. Rozing, "Trends in HPLC column formats - microbore, nanobore and smaller," *LC GS Europe*, vol 16, issue 2003.
- [101] S. Ghosal, "Electrokinetic flow and dispersion in capillary electrophoresis," *Annual Review of Fluid Mechanics*, vol. 38, pp. 309-338, 2006.
- [102] P. T. Kissinger and W. R. Heineman, *Laboratory techniques in electroanalytical chemistry*, 2nd ed. New York: Marcel Dekker, Inc., 1996.

- [103] J. Koehne, J. Li, A. M. Cassell, H. Chen, Q. Ye, H. T. Ng, J. Han, and M. Meyyappan, "The fabrication and electrochemical characterization of carbon nanotube nanoelectrode arrays," *Journal of Materials Chemistry*, vol. 14, pp. 676-684, Feb 21 2004.
- [104] P. H. Chen and R. L. McCreery, "Control of electron transfer kinetics at glassy carbon electrodes by specific surface modification," *Analytical Chemistry*, vol. 68, pp. 3958-3965, Nov 15 1996.
- [105] D. R. Lide, *CRC Handbook of Chemistry and Physics*, 77 ed. Boca Raton, FL: CRC Press, Inc., 1996.
- [106] M. Liger, S. Konishi, and Y.-C. Tai, "Uncooled all-Parylene bolometer," *Proceedings of MEMS 2004*, Maastricht, Holland, pp. 593-596, 2004.
- [107] C. L. Wang, L. Taherabadi, G. Y. Jia, M. Madou, Y. T. Yeh, and B. Dunn, "C-MEMS for the manufacture of 3D microbatteries," *Electrochemical and Solid State Letters*, vol. 7, pp. A435-A438, 2004.
- [108] Y. Mizuno, M. Liger, and Y.-C. Tai, "Nanofluidic flowmeter using carbon sensing element," *Proceedings of MEMS 2004*, Maastricht, Holland, pp. 322-325, 2004.
- [109] J. Kim, X. Song, K. Kinoshita, M. Madou, and B. White, "Electrochemical studies of carbon films from pyrolyzed photoresist," *Journal of the Electrochemical Society*, vol. 145, pp. 2314-2319, Jul 1998.
- [110] S. Ranganathan, R. McCreery, S. M. Majji, and M. Madou, "Photoresist-derived carbon for microelectromechanical systems and electrochemical applications," *Journal of the Electrochemical Society*, vol. 147, pp. 277-282, Jan 2000.
- [111] M. Liger, T. A. Harder, Y.-C. Tai, and S. Konishi, "Parylene-pyrolyzed carbon for MEMS applications," *Proceedings of MEMS 2004*, Maastricht, Holland, pp. 161-164, 2004.
- [112] S. Miserendino, S. Boland, and Y.-C. Tai, "Material and electrochemical properties of pyrolyzed Parylene-c," *Proceedings of 206th Joint International Meeting of the Electrochemical Society*, Honolulu, HI, 2004.
- [113] E. E. Hui, C. G. Keller, and R. T. Howe, "Carbonized Parylene as a conformal sacrificial layer," *Proceedings of Solid-State Sensor and Actuator Workshop*, Hilton Head, South Carolina, pp. 256-260, 1998.
- [114] O. Beyssac, B. Goffe, J. P. Petitet, E. Froigneux, M. Moreau, and J. N. Rouzaud, "On the characterization of disordered and heterogeneous carbonaceous materials by Raman spectroscopy," *Spectrochimica Acta Part a-Molecular and Biomolecular Spectroscopy*, vol. 59, pp. 2267-2276, Aug 2003.

- [115] F. Tuinstra and J. L. Koenig, "Raman Spectrum of Graphite," *Journal of Chemical Physics*, vol. 53, pp. 1126-1128, 1970.
- [116] S. Konishi, M. Liger, T. Harder, and Y.-C. Tai, "Parylene-pyrolyzed carbon for MEMS applications," *Proceedings of MEMS 2004*, Maastricht, The Netherlands, 2004.
- [117] S. Iijima, "Helical Microtubules of Graphitic Carbon," *Nature*, vol. 354, pp. 56-58, Nov 7 1991.
- [118] M. Monthieux and V. L. Kuznetsov, "Who should be given the credit for the discovery of carbon nanotubes?," *Carbon*, vol. 44, pp. 1621-1623, Aug 2006.
- [119] S. Iijima and T. Ichihashi, "Single-Shell Carbon Nanotubes of 1-Nm Diameter," *Nature*, vol. 363, pp. 603-605, Jun 17 1993.
- [120] D. S. Bethune, C. H. Kiang, M. S. Devries, G. Gorman, R. Savoy, J. Vazquez, and R. Beyers, "Cobalt-Catalyzed Growth of Carbon Nanotubes with Single-Atomic-Layerwalls," *Nature*, vol. 363, pp. 605-607, Jun 17 1993.
- [121] J. Li, R. Stevens, L. Delzeit, H. T. Ng, A. Cassell, J. Han, and M. Meyyappan, "Electronic properties of multiwalled carbon nanotubes in an embedded vertical array," *Applied Physics Letters*, vol. 81, pp. 910-912, Jul 29 2002.
- [122] J. Li, H. T. Ng, A. Cassell, W. Fan, H. Chen, Q. Ye, J. Koehne, J. Han, and M. Meyyappan, "Carbon nanotube nanoelectrode array for ultrasensitive DNA detection," *Nano Letters*, vol. 3, pp. 597-602, May 2003.
- [123] University of Reading, "Projects available for MSc in Physics by Research in 2006," <http://www.rdg.ac.uk/Physics/pgprogrammes/MSCprojects2006.htm>, 2007.
- [124] J. Koehne, H. Chen, J. Li, A. M. Cassell, Q. Ye, H. T. Ng, J. Han, and M. Meyyappan, "Ultrasensitive label-free DNA analysis using an electronic chip based on carbon nanotube nanoelectrode arrays," *Nanotechnology*, vol. 14, pp. 1239-1245, Dec 2003.
- [125] J. Li, A. Cassell, L. Delzeit, J. Han, and M. Meyyappan, "Novel three-dimensional electrodes: Electrochemical properties of carbon nanotube ensembles," *Journal of Physical Chemistry B*, vol. 106, pp. 9299-9305, Sep 12 2002.
- [126] B. A. Cruden, A. M. Cassell, Q. Ye, and M. Meyyappan, "Reactor design considerations in the hot filament/direct current plasma synthesis of carbon nanofibers," *Journal of Applied Physics*, vol. 94, pp. 4070-4078, Sep 15 2003.
- [127] A. L. Beilby, T. A. Sasaki, and H. M. Stern, "Electrochemical Pretreatment of Carbon Electrodes as a Function of Potential, Ph, and Time," *Analytical Chemistry*, vol. 67, pp. 976-980, Mar 1 1995.

- [128] R. C. Engstrom, "Electrochemical Pretreatment of Glassy-Carbon Electrodes," *Analytical Chemistry*, vol. 54, pp. 2310-2314, 1982.
- [129] V. P. Menon and C. R. Martin, "Fabrication and Evaluation of Nanoelectrode Ensembles," *Analytical Chemistry*, vol. 67, pp. 1920-1928, Jul 1 1995.